博 士 学 位 論 文
Doctoral Thesis

論文題目

Thesis Title

A Study on Thermally Induced Knudsen Forces for Contactless Driving Mechanism

東 北 大 学 大 学 院 工 学 研 究 科

Graduate School of Engineering,

TOHOKU UNIVERSITY

専攻/Department: Finemechanics

氏名/Name: Clint John Cortes Otic

TOHOKU UNIVERSITY
Graduate School of Engineering

A Study on Thermally Induced Knudsen Forces for Contactless Driving Mechanism
(非接触駆動機構のための熱的に誘起されるクヌッセン力の研究)

A dissertation submitted for the degree of Doctor of Philosophy (Engineering)
Department of Finemechanics

by
Clint John Cortes OTIC

July 8, 2022

A Study on Thermally Induced Knudsen Forces for Contactless Driving Mechanism

Clint John Cortes OTIC

Abstract

In a rarefied gas, an object placed close to structure of different temperature receives a force. This phenomenon is caused by the non-uniform temperature distribution in the gas at conditions where the Knudsen number, defined as the ratio of the mean free path for gas molecules to the characteristic length of the flow, is not vanishingly small. The macroscopic forces induced in this phenomenon are called as thermally induced Knudsen forces. Recent advancements in micro/nano-technologies led to applications of Knudsen forces in gas sensing, micro-actuators, precision instruments, and many more. These technologies exploit the normal component of the Knudsen force. However, related studies for ratchet-shaped channels have shown that a tangential component of the Knudsen force can be also induced in addition to the normal component. These studies suggested that the tangential Knudsen force can induce self-propulsion on a solid object. However, there are still some questions that need to be addressed. One, what other geometric configurations, aside from the conventional ratchet structure, can induce stronger Knudsen forces. Two, why the Knudsen forces are generated in the first place, or, what mechanisms are behind it. Lastly, how these thermally induced Knudsen forces can be used as an application for a novel device. These are the major points that this thesis aims to address using a combination of numerical and theoretical approaches.

In chapter 2, an infinitely wide and flat object placed close to an infinitely wide hot substrate is considered. Four configurations repeated periodically in the horizontal direction are considered as the surface structures on the substrate. The bottom surface of the object is also horizontal. One configuration is the commonly studied ratchet configuration, and the others are new modifications, namely, modified ratchet, oblique plate, and oblique ridge. Using the direct simulation Monte Carlo (DSMC) method, the flow in each configuration is reproduced at different Knudsen numbers. It was found that by modifying the conventional ratchet-shaped structure into the new configurations, a stronger tangential Knudsen force can be achieved. Specifically, the tip angle of the structure is an important parameter in optimizing the induced force. The increase in the propulsive force induced by the different microstructures is also found to depend on the Knudsen number and the temperature difference between the heated structure and the colder object. In all cases, the oblique plate induces the strongest tangential Knudsen force, followed by the modified ratchet and the oblique ridge. It is found that the smaller tip angles in the new configurations enhanced the tangential Knudsen force. Here, from the DSMC results, the difference in the tangential Knudsen force among the different structures is explained by considering the momentum brought onto the bottom surface of the upper object by incident molecules coming directly from the heated surfaces. However, the numerical results alone could not completely explain the behavior of the tangential Knudsen force.

Therefore, in chapter 3, the mechanism of the tangential Knudsen force is clarified theoretically. Specifically, a theoretical expression is formulated to describe the tangential Knudsen stress by considering the momentum fluxes transferred by two groups of molecules impinging on the surface of interest. One is a group of molecules directly coming from the other surface without experiencing intermolecular collisions, and the other is a group of

molecules coming from the bulk region after experiencing intermolecular collisions there. As reference, the same ratchet configuration used in the DSMC simulation is used, such that the lower surface is a hot ratchet structure and the upper surface is a flat cold object. The tangential Knudsen stress distribution and the net tangential Knudsen force induced on the object obtained in the theoretical analysis was compared with the results from the DSMC simulation at different Knudsen numbers. It is found that the theoretical tangential Knudsen stress distribution and the tangential Knudsen force show similar tendency with that obtained in the DSMC simulation. But, the values of both show a disparity. By adding the contribution of several factors that are not considered in the theory, such as viscous shear stress and thermal stress, onto the theoretical results, the theoretical results agree very well with the DSMC results for all considered Knudsen numbers less than and equal to unity. Based on this comparison, it is found that the tangential Knudsen force is caused by three mechanisms. First is the contribution of impinging molecules directly coming from the other surface with different temperature without experiencing intermolecular collisions. Second is the contribution of viscous effect of thermally driven flows. The third is the contribution of thermal stress.

In chapter 4, it is proposed that thermally induced Knudsen forces in a rarefied gas can be exploited to achieve a tweezer-like mechanism that can be used to trap and grasp a micro-object without physical contact. Using the DSMC method, it is demonstrated that the proposed mechanism is achieved when a heated thin plate mounted perpendicularly on a heated flat substrate is placed over and close to a colder object, in this case, a beam. This mechanism is mainly due to the pressure differences induced by the thermal edge flows at the corners of the beam and the thermal edge flow at the tip of the thin plate. Specifically, the pressure on the top surface of the beam is smaller than that on its bottom surface when the thin plate is above the beam, while the pressure on the right side of the beam is smaller than that on its left side when the thin plate is located near the right side of the beam. These differences in pressure generate a force which attracts the beam to the plate horizontally and vertically. The mechanism proposed here was also found to depend significantly with the height of the beam, the temperature difference between the thin plate and the beam, and the Knudsen number.

Hopefully, the results obtained here will help engineers and researchers to better design systems or devices with contactless driving mechanism using thermally induced Knudsen forces.

Contents

Chapter 1 Introduction

1.1 Background

In the 1870s, Sir William Crookes invented a device that uses light to induce a rotation on a series of vanes mounted inside a glass bulb[1]. The device, which still bears his name as Crookes radiometer, has fascinated scientists who were interested in the nature of the force rotating the vanes[2]. Several theories were suggested, including that of Crookes himself who argued that pressure of light is the origin of the force[1]. However, the mechanism was clarified later by Reynolds and Maxwell. They explained that in the presence of a thermal gradient in low pressure gas conditions, tangential forces along the edges of the vane are exerted by gas molecules, resulting in the rotations observed[3]. This is the pioneering application of thermally induced phenomena, specifically the radiometric force[4–7], in rarefied gas. Since then, studies on the radiometric forces have branched out into other related macroscopic forces, such as the thermophoretic force[8–11], where small particles receive a force when they are suspended in a gas with a temperature gradient. As these thermally induced forces appear under the condition that the Knudsen number, defined as the ratio of the mean free path for gas molecules to the characteristic length of the flow, is not vanishingly small, they are called Knudsen forces[11–15].

In addition to thermally induced Knudsen forces, thermally driven flows can also be induced in a rarefied gas with non-uniform temperature distributions[16–18]. First is the thermal creep flow which is induced along the solid surface from the colder region to the hotter region when the temperature of the solid surface is not uniform along the solid surface[16]. Second is the thermal stress slip flow which is induced along the solid surface from the hotter region to the colder region when the temperature gradient normal to the solid surface in the gas is not uniform along the solid surface[17]. Lastly, if a solid surface has a sharp edge, a steep temperature gradient in the gas is induced in the vicinity of the edge. This results in a flow by the same mechanism as the thermal creep flow, and is known as thermal edge flow[18]. Thermally driven flows are the key mechanism in the operation of Knudsen pumps that provide a steady gas flow

rate without using any moving parts and with a very simple structure[19]. These thermally driven flows are induced as a result of momentum transfer between gas molecules and solid surfaces. Namely, the thermally driven flows and the thermally induced forces are inseparably intertwined each other. In addition to this, the thermally driven flows have a pumping effect, and hence, they generate the spatial change of the gas pressure, which also induces a force exerted on solid surfaces. Therefore, when we consider the thermally induced forces, i.e., the Knudsen forces, we have to consider the thermally driven flows together.

The challenge with technological applications involving thermally induced phenomena is that under atmospheric conditions the mean free path of gas molecules is in micro/nano-scale. Therefore, the size of the system must be in the same order or smaller. This was a problem in the past, however, due to recent advances in micro-electromechanical systems (MEMS), it is now possible to fabricate micro/nano-devices that can exploit the Knudsen forces for specific applications[11–15,20–22]. Such technologies include microstructure actuation[12,20], gas sensing[13–15], atomic force microscopy[11,22], high precision force measurements[21], among others.

Studies on thermally induced phenomena in rarefied gas have shown that for certain configurations, the Knudsen force generated on the solid surfaces has not only a normal component but also a tangential component[23–28]. This tangential component of the Knudsen force is referred here as tangential Knudsen force, i.e., the thermally induced force acting tangentially on the surface of interest.

One interesting phenomenon where the tangential Knudsen force may play a key role is the self-propulsion[29] of the Leidenfrost object. The Leidenfrost effect [30] is the phenomenon that when an evaporating object such as a droplet or dry ice is placed on a highly heated surface, it levitates on the cushion of its own vapor. But when the heated surface has a shape such as that of a ratchet, the object is propelled with a definite direction and speed[29]. Würger[25] predicted that the thermally driven flows play a key role in the induced propulsive force. Specifically, he expected that a thermally driven flow appears along the inclined surface of the ratchet, entrains the surface of the Leidenfrost droplet and sets it into motion[25]. However, using the conditions of previous experiments and numerical analyses, it was found that although propulsive force is induced, thermally driven flows only play a minor role in the self-propulsion compared to the pressure-driven flow due to evaporation or sublimation[26]. Nevertheless, the results of numerical simulations in Ref. 26 still show that self-propulsion can be induced even when the object is not evaporating or sublimating, i.e., solid objects, given that the Knudsen number is not vanishingly small. Therefore, under the right conditions, the tangential Knudsen

force can induce self-propulsion even on a solid object. However, studies on this phenomenon have been limited to the ratchet configuration. Whether this phenomenon is enhanced in different configurations or not is still in question. Furthermore, it has been suggested that the propulsive Knudsen force appears due to the asymmetric nature of the ratchet structure[27–28]. Therefore, depending on the geometry, other asymmetric structures may induce stronger tangential Knudsen forces.

Despite the wide application of Knudsen forces and decades of research on the phenomenon, clarification is still needed on the mechanisms behind it and which mechanism is prevalent at specific flow regimes. Therefore, thorough consideration on the mechanism of the Knudsen force is becoming more significant. The works of Passian *et al*. [11], Scandurra *et al*. [31], and Zhu and Ye[32], are examples of rigorous theoretical studies aimed at understanding the mechanism of Knudsen forces. However, they focused on a specific configuration of a microcantilever hanging over a flat surface. They were particularly interested in the normal component of the Knudsen force. In contrast to the normal component of the Knudsen force, theoretical study on the tangential Knudsen force is even more lacking, or at least, clarity on its mechanism is still required. Some have tried to explain the tangential Knudsen force intuitively[24,28], and those who did detailed theoretical analysis have limited their discussion to non-diffusive surfaces and only in the free molecular flow regime[27]. Such studies are not suitable for common materials, where the surfaces are commonly fully diffusive, and for flows in the transition flow regime.

It is important to clarify the mechanism of the Knudsen force so that engineers and researchers can better design systems where thermally induced phenomenon is used. One of the commonly studied applications of the Knudsen force is a microactuator device composed of a microbeam and a flat plate[33–34]. Specifically, a beam placed close to a flat plate of different temperature receives a Knudsen force. Depending on the temperature gradient, the beam is either attracted or repelled to the plate[35]. Zhu and Ye[32] pointed out that the Knudsen force in this case is caused mainly by the thermal edge flow[36] induced around the sharp corners of the beam. In addition to this, as mentioned in the previous paragraphs, the configuration of the system has a significant influence on the magnitude and direction of the Knudsen force. The simple configuration of a microbeam and a flat plate can be applied to obtain a new device concept. Example of this is that two beams of different temperatures placed close to each other can act as a gas sensor mechanism[12,14–15,20], and a heated object placed eccentrically inside a closed system can act as a rotational mechanism[37].

It is crucial to note that the thermally induced phenomena described here appear in conditions where the Knudsen number is on the order of unity. Under such conditions, the gas is rarefied and cannot be treated as a continuum. For example, although the Navier-Stokes equation is given by

$$\rho \frac{D\boldsymbol{v}}{Dt} = \rho F - \nabla p + \mu \left[\nabla^2 \boldsymbol{v} + \frac{1}{3}\nabla(\nabla \cdot \boldsymbol{v})\right], \tag{1.1}$$

under the conditions that there is no external force and no external pressure gradient and the flow field is steady, it is apparent from the Navier-Stokes equation that steady flow cannot be induced even though steady temperature distribution is given on surfaces of solid objects in a gas. Namely, in the steady state, a rest gas of $\boldsymbol{v} = 0$ and a uniform pressure of $p = \text{const}$ are the obvious solution of the Navier-Stokes equation. Since the pressure is uniform and there is no viscous force because of zero velocity, no force is exerted on the solid objects immersed in the gas. But, as mentioned above, in such a situation, thermally induced forces and thermally driven gas flows such as thermal creep flow and thermal stress slip flows will appear when the Knudsen number is on the order of unity. Thus, for any temperature distribution on the solid surfaces, under continuum flow assumption, no flows and no forces cannot be expected by using the Navier-Stokes equations. Hence, thermally driven flows and Knudsen forces cannot be examined by using the Navier-Stokes equation. Instead, the Boltzmann equation, which describes the flow behavior considering molecular motion[38], must be used.

The Boltzmann equation can be solved stochastically[39] using the direct simulation Monte Carlo (DSMC) method[40] shown in Fig. 1.1. In this stochastic scheme, real molecules are represented by sample molecules whose motions are simulated and tracked over a long period of time. But the main essence of the DSMC method is that intermolecular collisions are decoupled from free molecular motions over a very small time-step[40]. This time-step is determined based on the gas molecules' mean free time, i.e., average time between intermolecular collisions. Using the DSMC method, rarefied gas flows can be reproduced to study different thermally induced phenomena and the corresponding Knudsen forces.

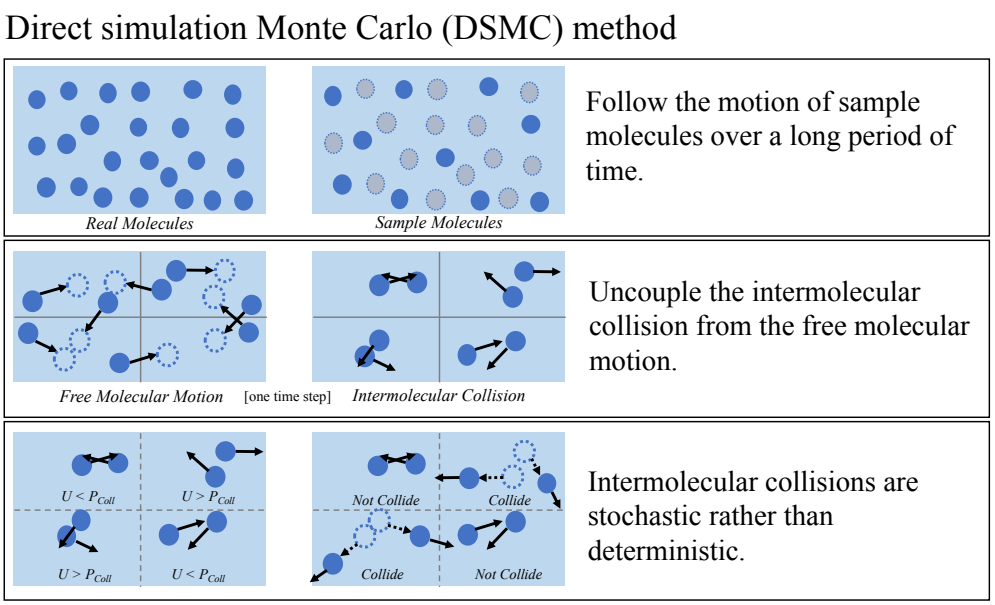

Fig. 1.1. The concept of DSMC method.

1.2 Objectives of this thesis

As mentioned above, from theory to applications, there are still several aspects of the thermally induced Knudsen force that are not considered. The objectives of the present study are to conduct a numerical investigation about the effect of new asymmetric configurations on the tangential Knudsen force, to clarify the mechanism of the tangential Knudsen force theoretically, and to propose a device exploiting the thermally induced Knudsen forces. As an example for the third objective, a concept of a tweezer-like mechanism which can grasp and manipulate a micro-object without contact is to be proposed. On the part of numerical analyses, gas flows are to be reproduced by performing numerical experiments by the direct simulation Monte Carlo (DSMC) method and the governing factors of the flow are to be investigated. On the theoretical part, the tangential Knudsen force is to be investigated by rigorous theoretical analysis on the momentum fluxes brought by molecules incident on the surface of interest.

1.3 Outline of this thesis

The rest of this thesis is organized as follows:

Chapter 2 provides the investigation on the self-propulsion of an object placed close to a heated substrate with periodically repeating structures. Specifically, a parametric study using numerical experiments by the DSMC method is carried out. One of the main goal of this chapter is to show how different configurations of the surface structure affect the thermally driven flows and propulsive force on the object, i.e., tangential Knudsen force. By modifying the conventional ratchet-shaped structure, new configurations that induce stronger tangential Knudsen forces are proposed. Moreover, an intuitive explanation on how these new configurations induce stronger tangential Knudsen forces was also provided. In addition, the effects of parameters like tip angles, oblique angles, Knudsen numbers, and temperature gradients on the tangential Knudsen force are also investigated.

Chapter 3 provides a theoretical investigation on the tangential Knudsen force induced on an object placed close to a heated substrate with periodically repeating structures described in Chap. 2. Specifically, Chap. 3 aims to clarify the mechanism of the tangential force theoretically by considering the two kinds of momentum fluxes transferred on the bottom surface of the object. The theoretical results are compared with the numerical results from Chap. 2. Based on the comparison, the mechanisms of the tangential Knudsen force are proposed. In addition, it is also clarified which mechanism is dominant at different flow regimes.

Chapter 4 shows that the thermally induced Knudsen forces can be exploited to obtain a tweezer-like mechanism which can be used to trap and manipulate a micro-object in a gas. Specifically, a numerical experiment by the DSMC method is used to demonstrate that when a heated thin plate is perpendicularly mounted on a heated substrate and placed close to a colder beam, a force is generated on the beam and attracts the beam to the thin plate horizontally and vertically. Therefore, in this simple configuration, the heated thin plate can act as a tweezer that can trap and manipulate the beam. The effect of different parameters on the thermally induced Knudsen forces is also investigated in this chapter.

References

[1] W. Crookes, “On attraction and repulsion resulting from radiation,” *Philosophical Transactions of the Royal Society A* 164, 501–527 (1874).

[2] G. Stanhill, “Sir William Crookes and his radiometer,” *Wether* 74, 56–57 (2019).

[3] J.C. Maxwell, “On stresses in rarified gases arising from inequalities of temperature,” *Philosophical Transactions of the Royal Society A* 170, 231–256 (1879).

[4] A. Ketsdever, N. Gimelshein, S. Gimelshein, and N. Selden, “Radiometric phenomena: From the 19th to the 21st century,” *Vacuum* 86, 1644–1662 (2012).

[5] S. Taguchi, and K. Aoki, “Motion of an array of plates in a rarefied gas caused by radiometric force,” *Physical Review E* 91, 063007 (2015).

[6] D. Zeng, R. Cai, and Y. Yang, “ Rarefied gas flow around a double-plate induced by temperature difference,” *Advances in Space Research* 69, 737 (2022).

[7] W. Phillips, “Thermal Force on Spherical Particles in a Rarefied Gas,” *Physics of Fluids* 15, 999 (1972).

[8] S. Beresnev and V. Chernyak, "Thermophoresis of a spherical particle in a rarefied gas: Numerical analysis based on the model kinetic equations," *Physics of Fluids* 7, 1743 (1995).

[9] S. Yu, J. Wang, G. Xia, L. Zong. “Thermophoretic force on nonspherical particles in the free-molecule regime,” *Physical Review E* 97, 053106 (2018).

[10] J.C. Padrino, J.E. Sprittles, D.A. Lockerby, “Thermophoresis of a spherical particle: modelling through moment-based, macroscopic transport equations,” *Journal of Fluid Mechanics* 862, 312–347 (2019).

[11] A. Passian, A. Wig, F. Meriaudeau, T. L. Ferrel, and T. Thundat, “Knudsen forces on microcantilevers,” *Journal of Applied Physics* 92, 6326 (2002).

[12] A. Strongrich, and A. Alexeenko, "Microstructure actuation and gas sensing by the Knudsen thermal force," *Applied Physics Letters* 107, 193508 (2015).

[13] D.D. Vo, R. Moradi, M.B. Gerdroodbary, and D.D. Ganji, "Measurement of low-pressure Knudsen force with deflection approximation for gas detection," *Results in Physics* 13, 102257 (2019).

[14] A. Pikus, I. Borges Sebastião, A. Strongrich, and A. Alexeenko, "Characterization of a Knudsen force based vacuum sensor for N2H2O gas mixtures," *Vacuum* 161, 130–137 (2019).

[15] Z. Li, A.M. Abazari, M. Barzegar Gerdroodbary, T. D. Manh, N. D. Nam, P. Valipour, R. Moradi, and H. Babazadeh, "Three-dimensional DSMC simulation of thermal Knudsen force in micro gas actuator for mass analysis of gas mixture," *Measurement* 160, 107848 (2020).

[16] Y. Sone, "Thermal creep in rarefied gas," *Journal of the Physical Society of Japan* 21, 1836 (1966).

[17] Y. Sone, "Flow induced by thermal stress in rarefied gas," *Physics of Fluids* 15, 1418 (1972).

[18] Y. Sone and M. Yoshimoto, "Demonstration of a rarefied gas flow induced near the edge of a uniformly heated plate," *Physics of Fluids* 9, 3530 (1997).

[19] X. Wang, T. Su, W. Zhang, Z. Zhang, and S. Zhang, "Knudsen pumps: A review," *Microsystems & Nanoengineering* 6, 26 (2020).

[20] A. Alexeenko, A. D. Strongrich, A. G. Cofer, A. Pikus, I. B. Sebastiao, S. S. Tholeti, and G. Shivkumar, "Microdevices enabled by rarefied flow phenomena," *AIP Conference Proceedings* 1786, 080001 (2016).

[21] B. W. Harris, F. Chen, and U. Mohideen, "Precision measurement of the Casimir force using gold surfaces," *Physical Review A* 62, 052109 (2000).

[22] B. Gotsmann and U. Dürig, "Experimental observation of attractive and repulsive thermal forces on microcantilevers," *Applied Physics Letters* 87, 194102 (2005).

[23] T. Baier, S. Hardt, V. Shahabi, and E. Roohi, "Knudsen pump inspired by Crookes radiometer with a specular wall," *Physical Review Fluids* 2, 033401(2017).

[24] V. Shahabi, T. Baier, E. Roohi, and S. Hardt, "Thermally induced gas flows in ratchet channels with diffuse and specular boundaries," *Scientific Reports* 7, 41412(2017).

[25] A. Würger, “Leidenfrost gas ratchets driven by thermal creep,” *Physical Review Letters* 107, 164502(2011).

[26] S. Hardt, S. Tiwari, and T. Baier, “Thermally driven flows between a Leidenfrost solid and a ratchet surface,” *Physical Review E* 87, 063015(2013).

[27] A. Donkov, S. Tiwari, S. Liang, S. Hardt, A. Klar, and W. Ye, “Momentum and mass fluxes in a gas confined between periodically structured surfaces at different temperatures,” *Physical Review E* 84, 016304(2011).

[28] A. Lotfian and E. Roohi, “Radiometric flow in periodically patterned channels: Fluid physics and improved configurations,” *Journal of Fluid Mechanics* 860, 544–576(2019).

[29] H. Linke, B. J. Alemán, L.D. Melling, M.J. Taormina, M.J. Francis, C.C. Dow-Hygelund, V. Narayanan, R.P. Taylor, and A. Stout, “Self-propelled Leidenfrost droplets,” *Physical Review Letters* 96, 154502(2006).

[30] J.G. Leidenfrost, “On the fixation of water in diverse fire,” *International Journal of Heat and Mass Transfer* 9, 1153–1166 (1966).

[31] M. Scandurra, F. Izacopetti, and P. Colona, “Gas kinetic forces on thin plates in the presence of thermal gradients,” *Physical Review E* 75, 026308 (2007).

[32] T. Zhu and W. Ye, “Origins of Knudsen forces on heated microbeams,” *Physical Review E* 82, 036308 (2010).

[33] A. Passian, R. J. Warmack, T. L. Ferrell, and T. Thundat, “Thermal Transpiration at the Microscale: A Crookes Cantilever,” *Physical Review Letters* 90, 124503 (2003).

[34] J. Nabeth, S.Chigullapalli, and A. Alexeenko, “Quantifying the Knudsen force on heated microbeams: A compact model and direct comparison with measurements,” *Physical Review E* 83, 066306 (2011).

[35] A. Strongrich, W. O’Neill, A. Cofer, and A. Alexeenko,, “Experimental measurements and numerical simulations of the Knudsen force on a non-uniformly heated beam,” *Vaccuum* 109, 405–416 (2014).

[36] S. Taguchi and T. Tsuji, “One-way flow over uniformly heated U-shaped bodies driven by thermal edge effects,” *Science Reports* 12, 1929 (2022).

[37] Q. Li, T. Liang, and W. Ye, “Knudsen torque: A rotational mechanism driven by thermal force,” *Physical Review E* 90, 033009 (2014).

[38] Y. Sone, *Molecular Gas Dynamics: Theory, Techniques, and Applications* (Birkhauser, Boston, USA, 2007).

[39] K. Nanbu, "Direct simulation scheme derived from the Boltzmann equation—I: Monocomponent gases," *J. Phys. Soc. Jpn.* 49, 2042–2049 (1980).

[40] G.A. Bird, *Molecular Gas Dynamics and the Direct Simulation of Gas Flows* (Oxford, USA, 1994).

Chapter 2 A Numerical Study on the Tangential Knudsen Force Induced by Different Surface Structures

2.1 Introduction

It is well known that non-uniform temperature fields induce convection in a continuum gas surrounding us. Here, convection is induced due to the combined effect of non-uniform density and gravity, i.e., buoyancy. However, if there is no external force such as gravity, convection will not occur because buoyancy will not appear since it is driven by gravity. Contrary to this, non-uniform temperature fields in a rarefied gas, such as that in micro/nano-scale flow or low-pressure conditions, can cause a steady flow even without external forces. This phenomenon appears in conditions where the Knudsen number, defined as the ratio of the mean free path for gas molecules to the characteristic length of the flow, is not vanishingly small [1]. Such flows are called thermally driven flows since they are induced by non-uniform temperature distributions. These include the thermal creep flow, thermal stress slip flow, nonlinear thermal stress flow, and thermal edge flow [2]. Thermally driven flows are the key mechanism in the operation of Knudsen pumps that provide a steady gas flow rate without using any moving parts [3]. The very simple structures of several micro-scale configurations of the Knudsen pump [4–5] make it attractive for research. The physics of thermally driven flows has been a subject of several analyses, from lid-driven cavity cases [6–7] to periodically patterned channel cases [8]. Furthermore, in addition to thermally driven flows, temperature distributions in rarefied gas can also generate macroscopic forces. Specifically, the profile of the temperature distribution in the

---

Discussions are based mainly on C.J.C. Otic and S. Yonemura, "Effect of different surface microstructures in the thermally induced self-propulsion phenomenon," *Micromachines* 13, 871 (2022).

gas can result in a force on the solid boundaries and a net gas flow [9]. These macroscopic forces can be in the form of radiometric forces [10] and thermophoretic forces [11], among other forces, which are collectively called Knudsen forces [12–13]. A significant number of studies on Knudsen forces have focused mainly on its normal component due to its potential applications in actuation devices [14–15]. However, several studies on a channel bounded by periodically structured surfaces with different temperatures and whose characteristic length is in the order of or less than the mean free path for gas molecules have shown that the Knudsen force generated on the solid boundaries has not only a normal component but also a tangential component [16–18]. It was even suggested that the tangential component of the Knudsen force may have contributed to the self-propulsion of a Leidenfrost object placed on a heated ratchet surface [17,19]. The results from these previous studies [16–19] have suggested that if an object is placed close to a substrate with a surface microstructure, a force will be induced on the object. This force can set the object in motion without the use of moving parts, i.e., self-propulsion. As this force is acting on the surface of the object tangentially to it, and this force only appears in not so low Knudsen numbers, this propulsive force is referred to in this study as the tangential Knudsen force or the tangential Knudsen stress in the unit area. Moreover, it has been pointed out intuitively that the asymmetric nature of the ratchet structure is the origin of the tangential Knudsen force [16]. Therefore, by modifying the surface structure into different asymmetric configurations, the tangential Knudsen force can be controlled and optimized. In this chapter, new configurations with asymmetric geometries are presented as surface microstructures that are modifications to the conventionally used ratchet configuration. The results of this study will be useful in designing systems that utilize this self-propulsion.

2.2 Methodology

2.2.1 Configuration of the surface microstructures

Consider an infinitely wide object of cold temperature $T_c = 300$ K placed close to an infinitely wide substrate of hot temperature $T_h = 500$ K, which has a surface structure repeated periodically in the x-direction, as shown in Fig 2.1. The bottom surface of the object is perfectly flat and defines the upper boundary of the channel. On the other hand, the substrate with the periodically repeated surface structure of periodic length L_P and a depth d defines the lower

boundary of the channel. The space between the bottom surface of the object and the substrate creates a channel that is filled with air. The minimum gap g between the bottom surface of the object and the tip of the surface structure of the substrate was set at $g = 0.2d$.

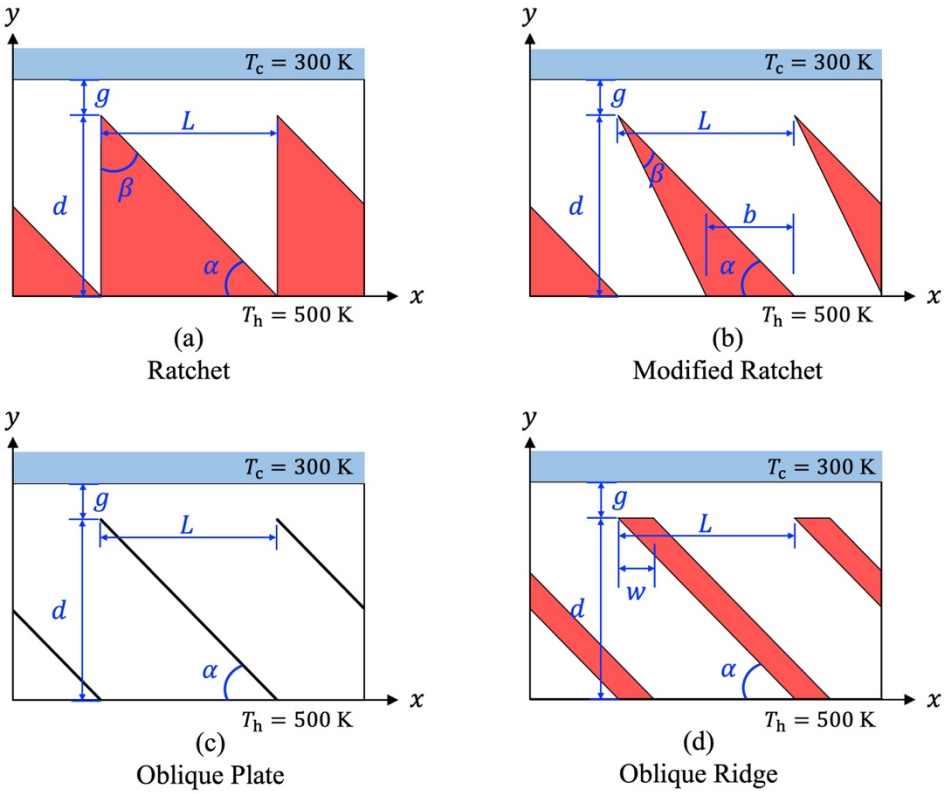

Fig. 2.1. Schematics of the substrate with different surface microstructures. Reprinted with permission from C. J. C. Otic and S. Yonemura, Micromachines 13, 871 (2022). Copyright 2022 Author(s).

The four configurations shown in Fig. 2.1 are considered here as the surface structures. The first surface structure is called here as "ratchet" shown in Fig. 2.1 (a), is defined by the periodic length L_P , an oblique wall with an inclination angle α, a vertical wall with a depth d given by $d = L_P \tan\alpha$, and a tip angle β given by $\beta = (\pi/2) - \alpha$. The second surface structure is called here as "modified ratchet" with the tip angle set $\beta < (\pi/2) - \alpha$ without changing the inclination angle α, as shown in Fig. 2.1 (b). Note that this modification causes the vertical side of the ratchet to be adjusted into an inclined orientation. Let us call this the modified side and the other oblique wall, the oblique side, respectively. The third surface structure is called here

as “oblique plate,” which is the limiting case of the modified ratchet, i.e., $\beta = 0$, as shown in Fig. 2.1 (c). In this case, the modified side coincides with the oblique side. The fourth surface microstructure is called here as “oblique ridge,” which is a modification of the oblique plate in which a thickness w is added, as shown in Fig. 2.1 (d). In this study, an aspect ratio of unity, i.e., $d = L_{\mathrm{P}}$, is considered as the reference such that the inclination angle is $\alpha = \pi/4$. Furthermore, a base length $L_{\mathrm{b}} = 0.5L_{\mathrm{P}}$ is considered as the reference for the modified ratchet structure such that its tip angle is $\beta = (\pi/4) - \tan^{-1} 0.5$, while the ridge width $w_{\mathrm{r}} = 0.2L_{\mathrm{P}}$ is used for the oblique ridge.

2.2.2 Direct simulation Monte Carlo (DSMC) method and parameters

This study focuses on flows outside the continuum flow regime, and therefore, the Navier–Stokes equation is not applicable. The direct simulation Monte Carlo (DSMC) method [20–21] was used to reproduce such flows. The DSMC method has already been used in several studies to simulate thermally driven flows in microchannels involving ratchet-like periodic structures [16–18]. This method is a particle-based algorithm in which real molecules are represented by a relatively small number of sample molecules that approximate the velocity distribution function of the real molecules, and the motions of sample molecules are simulated and followed. Although realistic air consists of many kinds of molecules, the air molecules are represented with an imaginary hard-sphere molecule [22] of mass $m = 4.80967 \times 10^{-26}$ kg and a diameter $d_{\mathrm{m}} = 0.356$ nm. The diameter d_{m} was evaluated from a reference viscosity and using the reference temperature $T_{\mathrm{ref}} = (T_{\mathrm{h}} + T_{\mathrm{c}})/2 = 400$ K [23–24]. For simplicity, it is assumed that the diameter of hard-sphere molecules does not depend on the local temperature of the gas. Thus, in the present study, the discussion of the Knudsen force is not for a realistic air but for the ideal case of a gas consisting of hard-sphere molecules with constant diameter. That is, the discussion in this study will not be strictly accurate for a realistic air. However, thanks to the usage of molecules of the constant diameter, which is not unique to air, the results obtained in the present simulations can be applied to other gases without being limited to air in the case wherein the Knudsen number is the same.

The reference mean free path λ_{ref} and the reference mean free time τ_{ref} for molecules with a diameter $d_{\mathrm{m}} = 0.356$ nm under the condition of the reference atmosphere set at $p_{\mathrm{ref}} = 101325$ Pa, and the reference temperature $T_{\mathrm{ref}} = 400$K, are $\lambda_{\mathrm{ref}} = 96.7969$ nm and $\tau_{\mathrm{ref}} = 1.790101 \times 10^{-10}$ s, respectively. These are obtained by using the relations $\lambda = 1/\sqrt{2}\, n\pi d_{\mathrm{m}}^2$

and $p = nk_{\mathrm{B}}T$, where n is the number density and $k_{\mathrm{B}} = 1.380649 \times 10^{-23}$ J/K is the Boltzmann constant. Note that τ_{ref} is the expected mean free time, which corresponds to the mean free path λ_{ref} and is given by $\tau_{\mathrm{ref}} = \lambda_{\mathrm{ref}}/\bar{C}_{\mathrm{ref}}$, where $\bar{C}_{\mathrm{ref}} = \sqrt{8k_{\mathrm{B}}T_{\mathrm{ref}}/\pi m}$ is the mean molecular speed.

The gap distance g was used as the characteristic length to define the Knudsen number Kn, as $\mathrm{Kn} = \lambda_{\mathrm{ref}}/g$. In this study, the Knudsen number is adjusted by keeping the gas mean free path λ_{ref} constant, i.e., the reference gas pressure p_{ref} is kept constant while adjusting the gap g as $g = \lambda_{\mathrm{ref}}/\mathrm{Kn}$. For example, with the λ_{ref} given above, in the case of $\mathrm{Kn} = 0.1$, the gap is $g = 967.9697$ nm, and so on. In each of the surface microstructures, the flow was investigated at different Knudsen numbers enumerated in Table 2.1. The computational domain used for the DSMC in each microstructure is the region within one periodic length L_{P} along the x axis, i.e., $0 \le x \le L_{\mathrm{P}}$, and $0 \le y \le d + g$. Here, $y = 0$ is set at the bottom of the microstructure, and $x = 0$ is set at the center of the oblique side, except for the oblique ridge where $x = 0$ is set at the center of the left side of the oblique ridge, as shown in Fig. 2.2. In addition, the side boundaries of the computational domain are considered to be periodic in the $+x$-direction and $-x$-direction. A uniform grid is used such that the computational domain was divided into rectangular cells with cell size $\Delta x = \Delta y$. The chosen cell sizes at different Knudsen numbers are enumerated in Table 1 and is set sufficiently smaller than the mean free path, at a maximum of $\lambda_{\mathrm{ref}}/3$, for all the Knudsen number considered in this study. Moreover, the number of sample molecules in each DSMC cell was initialized at 50 for the standard cell size of $\Delta x \times \Delta y$.

The main essence of the DSMC method is the uncoupling of the intermolecular collision from the free molecular motion over a small time step Δt. The time step Δt must be set much smaller than the mean free time τ_{ref} for intermolecular collisions [20]. In this study, the chosen time step is enumerated in Table 2.1. Notice that for Knudsen numbers less than unity, $\mathrm{Kn} \le 1$, the time step is set at $\Delta t = 0.08\tau_{\mathrm{ref}}$, which corresponds to a representative molecular displacement in the x-direction or y-direction of $(\bar{C}_{\mathrm{ref}}/2)\Delta t = 0.04\lambda_{\mathrm{ref}}$. This is sufficiently smaller than the cell size Δx or Δy, that molecules do not travel across more than one cell size within one time step. For Knudsen numbers greater than unity, $\mathrm{Kn} > 1$, consider the case where the time step is kept at $\Delta t = 0.08\tau_{\mathrm{ref}}$, i.e., the corresponding representative molecular displacement is kept at $0.04\lambda_{\mathrm{ref}}$, while the cell size is $0.05g = 0.05\,\lambda_{\mathrm{ref}}/\mathrm{Kn}$. Under such conditions, the cell size decreases with increasing Kn and will be smaller than the representative molecular displacement, i.e., molecules can travel across more than one cell size within one time step. In order to avoid this, the time step for $\mathrm{Kn} > 1$ is set at $\Delta t = 0.08g/\bar{C}_{\mathrm{ref}}$ instead, such that the representative molecular displacement is $(\bar{C}_{\mathrm{ref}}/2)\Delta t = 0.04g$, which is smaller

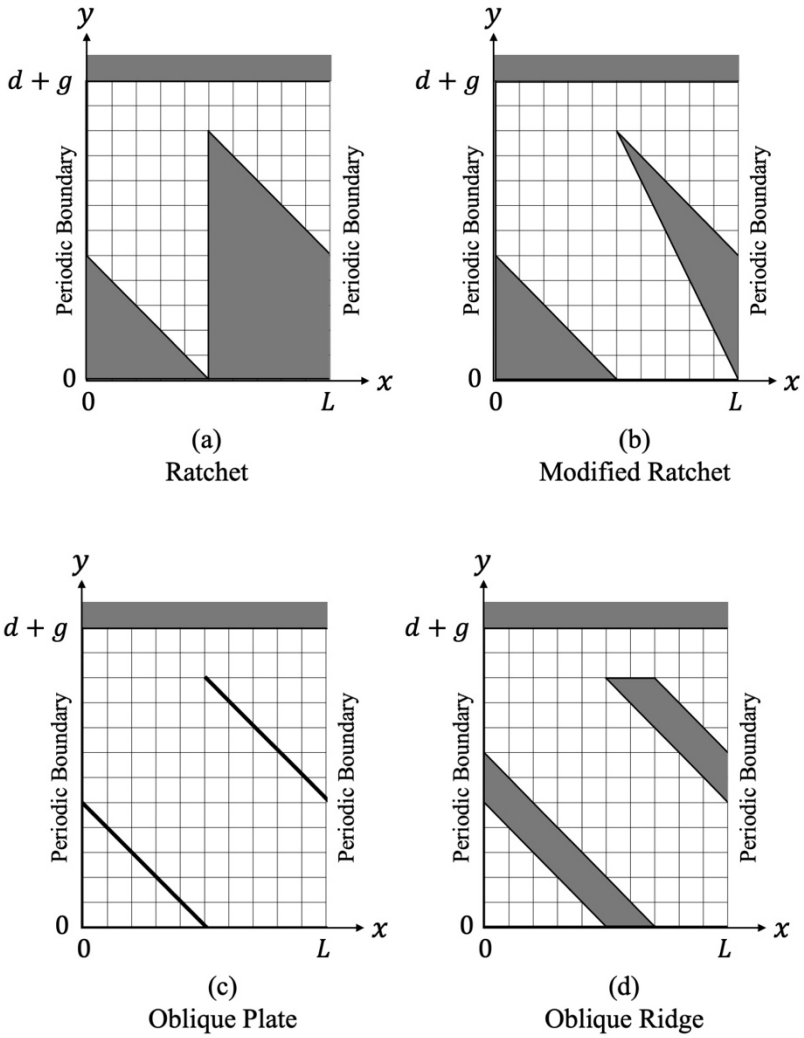

Fig. 2.2. Computational domain used in each microstructure. Reprinted with permission from C. J. C. Otic and S. Yonemura, Micromachines 13, 871 (2022). Copyright 2022 Author(s).

Table 2.1. Parameters for the DSMC Simulation for the different Knudsen number cases.

Knudsen number	**Cell size**	**Time step**
0.05, 0.1	$\lambda_{\mathrm{ref}}/3$	$0.08\tau_{\mathrm{ref}}$
0.2, 0.3, 0.5, 0.7, 1.0	$0.05g$	$0.08\tau_{\mathrm{ref}}$
1.4, 2.0, 3.0, 5.0, 10, 20, 50, 100	$0.05g$	$0.08g/\bar{C}_{\mathrm{ref}}$

than the cell size of $0.05g$. By doing so, the condition that molecules do not travel across more than one cell size within one time step is satisfied even for high Knudsen numbers.

The free motions and intermolecular collisions of molecules were tracked, and the time evolution of the flow field was simulated. In the present simulations, intermolecular collisions were judged stochastically based on the collision probability for the pair of sample molecules in each cell by using the maximum collision number method [25–26].

To elucidate this method, let us consider a single cell containing N number of sample molecules whose velocities are $\boldsymbol{c}_1, \boldsymbol{c}_2, \cdots, \boldsymbol{c}_N$. The probability that a sample molecule s will collide with another sample molecule k within a single time step Δt, $P_{s,k}$, is

$$P_{s,k} = N^{-1} n g_{s,k} \sigma_{\mathrm{T}} \Delta t, \tag{2.1}$$

where $g_{s,k} = |\boldsymbol{c}_k - \boldsymbol{c}_s|$ is the relative speed between the sample molecules s and k, n is the number density of real molecules in the considered cell, and σ_{T} is the total collision cross-section given by $\sigma_{\mathrm{T}} = \pi d_{\mathrm{m}}^2$. Then, the maximum collision probability, $P_{\max}$, is evaluated using the estimated maximum relative speed between all possible pairs, $g_{\max}$, such that

$$P_{\max} = N^{-1} n g_{\max} \sigma_{\mathrm{T}} \Delta t. \tag{2.2}$$

In the present simulations, initially, the maximum relative speed was estimated as $g_{\max} = 5\sqrt{k_{\mathrm{B}} T_{\mathrm{ref}}/m}$. In the case when a $g_{s,k}$ larger than $g_{\max}$ appeared, the value of $g_{\max}$ was replaced by the larger one.

In the maximum collision number method, it is considered that each pair of molecules has a collision probability of $P_{\max}$. However, this is not a real collision. This type of collision with the probability of $P_{\max}$ is considered as a tentative collision, in other words, a candidate of real collision. As the number of possible pairs of sample molecules in the cell is $N(N-1)/2$, the number of tentative collision pairs is given by

$$\begin{aligned} P_{\max} &= N^{-1} n g_{\max} \sigma_{\mathrm{T}} \Delta t, \\ P_{\max} &= (N-1) n g_{\max} \sigma_{\mathrm{T}} \Delta t/2. \end{aligned} \tag{2.3}$$

Here, $N_{\max}$ is called the maximum collision number. Then, $N_{\max}$ tentative collision pairs is chosen randomly out of all $N(N-1)/2$ possible pairs of sample molecules. This procedure is equivalent to the procedure in that tentative collision pairs based on the probability of $P_{\max}$ is

chosen. Then, it is judged whether each of the selected tentative collision pairs, e.g. (s,k), results in a real collision pair or not, based on the probability of $P_{s,k}/P_{\max}$. Thus, this procedure is equivalent to the procedure that whether each of $N(N-1)/2$ possible pairs, e.g. (s,k), results in a real collision pair or not is judged based on the probability $P_{s,k}$ since $P_{\max} \times \left(P_{s,k}/P_{\max}\right) = P_{s,k}$. The latter procedure is straightforward, but its computational load is proportional to $N(N-1)/2$, i.e., roughly N^2. Using a large number of sample molecules is an expensive task for the latter procedure. On the other hand, the former procedure, i.e., the maximum collision number method, is two-tiered, and its computational load is proportional to $N_{\max}$, i.e., $\{N(N-1)/2\} \times P_{\max}$. As $P_{\max}$ is inversely proportional to N as shown in Eq. (2.3), the computational load of the maximum collision number method is proportional to N. Due to this characteristic of the maximum collision number method, a large number of sample molecules can be used.

In addition, for molecule–wall collisions at the solid boundaries, impinging gas molecules were scattered using the diffuse reflection model [22]. Within an infinitesimally small time length of molecule-surface interaction, all the molecules impinging on the surface were diffusively emitted after the full adaptation to the temperature of the surface.

After the gas flow was judged to have reached the steady state, the molecular velocities and the number of sample molecules started to be sampled at each DSMC cell, and the impulses given on the bottom surface of the upper object by colliding molecules started to be accumulated. The number density n, flow velocity $\boldsymbol{v}$, and temperature T in each cell (i,j) at the end of M_{samp} samplings are

$$n_{i,j} = \frac{W_{\mathrm{f}}}{V_{\mathrm{cell}}(i,j)}\left[\frac{N_{\mathrm{tot}}(i,j)}{M_{\mathrm{samp}}}\right], \tag{2.4}$$

$$\boldsymbol{v}_{i,j} = \frac{1}{N_{\mathrm{tot}}(i,j)}\sum_{l=1}^{M_{\mathrm{samp}}}\sum_{q=1}^{N^{(l)}(i,j)}\boldsymbol{c}_q, \tag{2.5}$$

$$T_{i,j} = \frac{m}{3k_{\mathrm{B}}}\left[\left(\frac{1}{N_{\mathrm{tot}}(i,j)}\sum_{l=1}^{M_{\mathrm{samp}}}\sum_{q=1}^{N^{(l)}(i,j)}\boldsymbol{c}_q^2\right) - \boldsymbol{v}_{i,j}^2\right]. \tag{2.6}$$

Here, $V_{\mathrm{cell}}(i,j)$ is the volume of the cell (i,j), W_{f} is the number of real molecules represented by one sample molecule, $N_{\mathrm{tot}}(i,j)$ is the total number of molecules sampled at cell (i,j), $N^{(l)}(i,j)$ is the number of molecules sampled at the cell (i,j) at the moment of lth sampling, and $\boldsymbol{c}_q$ is the velocity of the qth sample molecule existing in the DSMC cell (i,j) at the moment of the lth sampling. Note that the corresponding pressure is evaluated from $p_{i,j} = n_{i,j}k_{\mathrm{B}}T_{i,j}$. On the other hand, the propulsive force referred to in this study is the force acting tangentially

on the bottom surface of the upper object, simply called in this study the tangential Knudsen force. The local tangential Knudsen stress, $\tau_{\mathrm{Kn},i}$, i.e., the local tangential Knudsen force per unit area, is defined as

$$\tau_{\mathrm{Kn},i} = \frac{W_{\mathrm{f}}}{\Delta x_i (t_{\mathrm{end}} - t_{\mathrm{start}})} \sum_{q=1}^{N_{\mathrm{wall-coll},i}} m \left[(\boldsymbol{c}_q)_x - (\boldsymbol{c}_q)'_x \right]. \tag{2.7}$$

Here, $\tau_{\mathrm{Kn},i}$ is the tangential Knudsen stress exerted on the ith surface element with width Δx_i on the bottom surface of the upper object, t_{start} and t_{end} are the starting time and the ending time of sampling, $N_{\mathrm{wall-coll},i}$ is the number of sample molecules colliding onto the element Δx_i during the sampling term from $t = t_{\mathrm{start}}$ to $t = t_{\mathrm{end}}$, $\boldsymbol{c}_q$ and $\boldsymbol{c}'_q$ are the pre-collision and post-collision velocities of the qth sample molecule in terms of the order of molecule–wall collision occurring in the sampling term, and the suffix x represents the x component of the molecular velocities. The net tangential Knudsen stress, τ_{Kn}, is then obtained by averaging the local tangential Knudsen force for Eq. (2.7).

2.3 Results and discussion

From the works of Y. Sone and K. Aoki [1–2], with some knowledge of the expected temperature distribution in the gas, the behavior of the thermally induced gas flows mentioned in Sec. 1 can be predicted. Specifically, it is expected that the temperature distribution of the gas near the oblique side will be non-uniform, and therefore, thermal stress slip flow can be induced near that region. In addition, it is also expected that the temperature distribution at the tips of the microstructure will be strongly non-uniform, and therefore, strong thermal edge flows can be induced near that region. The strength and behavior of thermal edge flow will depend on the shape and orientation of the tips of the microstructure. As the tip angle is different in each microstructure, the strength and behavior of the thermal edge flow is expected to vary in each configuration. Furthermore, according to Aoki *et al*. [2], the strength of thermally driven flows will depend on the Knudsen number. Figures 2.3–2.5 show the resulting flow distributions and temperature distributions obtained from the DSMC simulation for each microstructure at selected Knudsen numbers. First, at $\mathrm{Kn} = 0.1$, it can be seen from Fig. 2.3 that strong temperature gradients are localized on the tips of the microstructures, and strong flow is induced along the surfaces of the tips that are directed from the cold to the hotter region.

This is the thermal edge flow that dominates the flow field, while the thermal stress slip flow is not visible. Second, at $\mathrm{Kn} = 1$, it can be seen from Fig. 2.4 that strong temperature gradients can now be seen in the vicinity of the oblique sides, and flows are induced along their surfaces from the hot region to the colder region. This is the thermal stress slip flow which combines with thermal edge flow to generate a strong counter-clockwise vortex that dominates the flow field. Lastly, at $\mathrm{Kn} = 10$, it can be seen from Fig. 2.5 that the temperature gradients weaken, and the thermally driven flows also weaken but still persist, especially the thermal stress slip flow. As expected, the sharper tips of the new configurations result in stronger thermal edge flows for all the selected Knudsen numbers. As for the flow along the oblique side, stronger flow can be seen in the cases of the three new configurations compared to the ratchet configuration. However, the contribution of thermal stress slip flow, in this case, may not largely differ among the four configurations. This is because for all the configurations, the orientation of the oblique side is the same, and hence, the temperature field near the oblique side is not so different. Most probably, the difference in the flow along the oblique side among the cases is caused by the difference in the strength of the thermal edge flow to satisfy the equation of continuity. Thus, it was found that the three new configurations proposed in this study induce much stronger flows compared to the conventional ratchet configuration. The results obtained here indicate that the new configurations can induce higher gas flow rates in the case of Knudsen pump applications.

Next, let us investigate the propulsive force induced on the bottom surface of the upper object. As mentioned, this propulsive force per unit area is the tangential Knudsen stress, τ_{Kn}. Fig. 2.6 shows the distribution of the local tangential Knudsen stress obtained from the DSMC simulation in each microstructure at $\mathrm{Kn} = 1$. In this study, p_{ave}, which is the pressure spatially averaged in the bulk region of the gas, is used for non-dimensionalization. A positive value of the local tangential Knudsen stress means that the local propulsive force is directed rightward, i.e., $+x$-direction, while a negative value means that the local propulsive force is directed leftward, i.e., $-x$-direction. It can be seen that negative tangential Knudsen forces are located on the surface near the tip of each microstructure, while positive tangential Knudsen forces are located on the surface above the oblique side except in the region near the tip. When compared to other sections on the bottom surface of the upper object, the tangential Knudsen stress on the sections in the upper right neighborhood of the tip, around $0.5 < x/L_{\mathrm{P}} < 0.7$, are similar in each configuration except for the case of the oblique ridge. Although the location of tip for the oblique ridge is the same as that for the other configurations, the location of the oblique side is shifted rightward by its width $w_{\mathrm{r}} = 0.2L_{\mathrm{P}}$. Therefore, care should be taken when comparing it

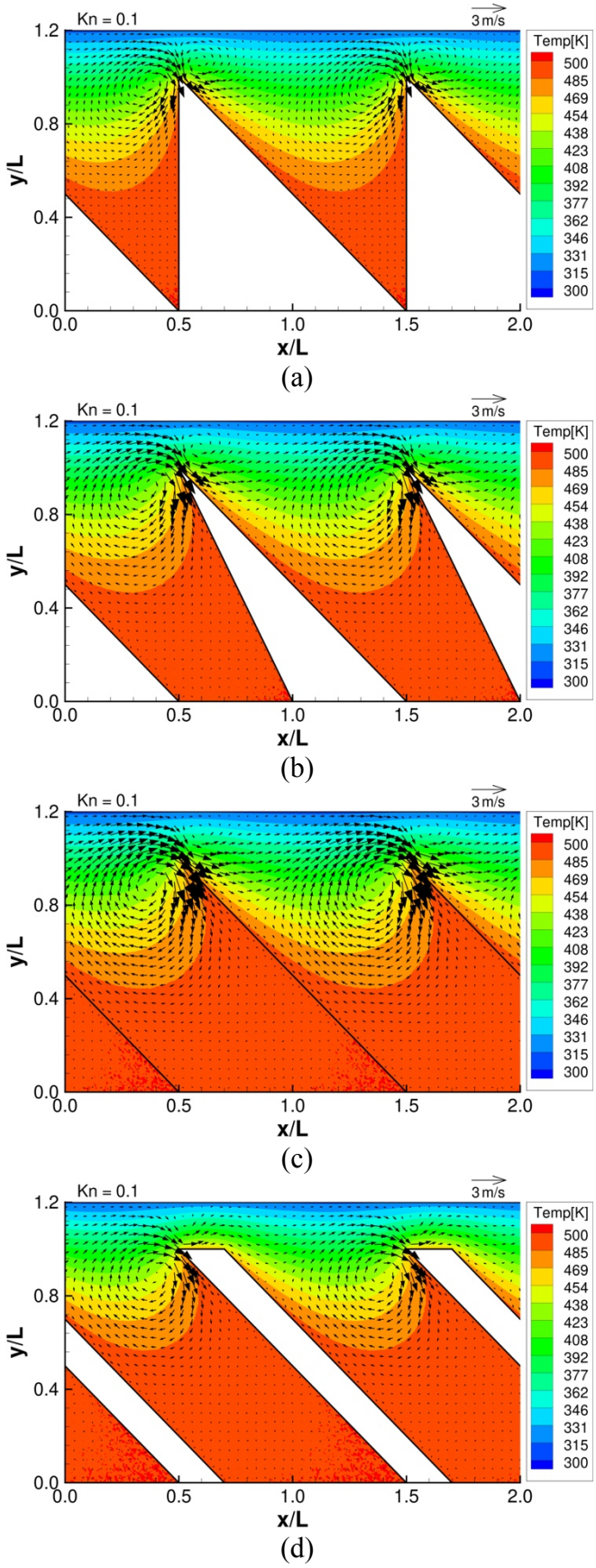

Fig. 2.3. Flow distribution and temperature distribution for (a) ratchet, (b) modified ratchet, (c) oblique plate, and (d) oblique ridge, at Kn = 0.1. Reprinted with permission from C. J. C. Otic and S. Yonemura, Micromachines 13, 871 (2022). Copyright 2022 Author(s).

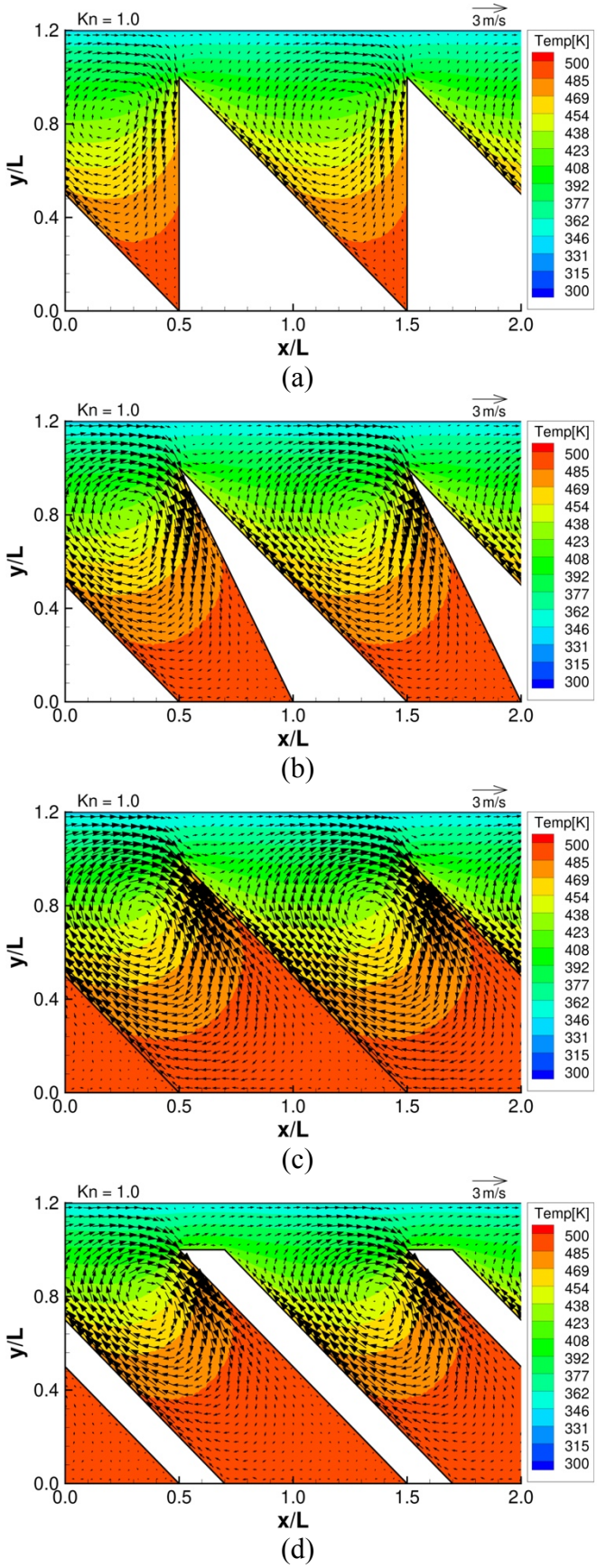

Fig. 2.4. Flow distribution and temperature distribution for (a) ratchet, (b) modified ratchet, (c) oblique plate, and (d) oblique ridge, at Kn = 1. Reprinted with permission from C. J. C. Otic and S. Yonemura, Micromachines 13, 871 (2022). Copyright 2022 Author(s).

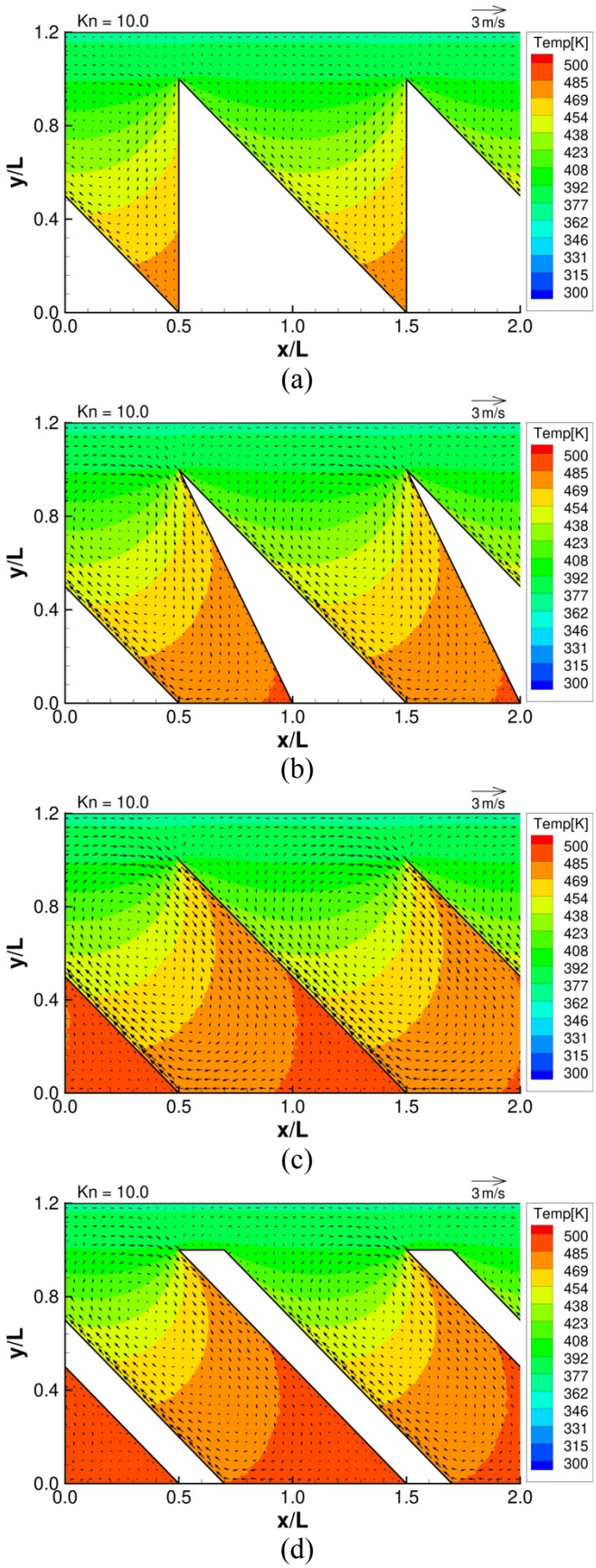

Fig. 2.5. Flow distribution and temperature distribution for (a) ratchet, (b) modified ratchet, (c) oblique plate, and (d) oblique ridge, at Kn = 10. Reprinted with permission from C. J. C. Otic and S. Yonemura, Micromachines 13, 871 (2022). Copyright 2022 Author(s).

with others. The differences in the distribution of the tangential Knudsen stress among the different configurations except for the oblique ridge can be considered to be largely due to the decrease in the tip angle β.

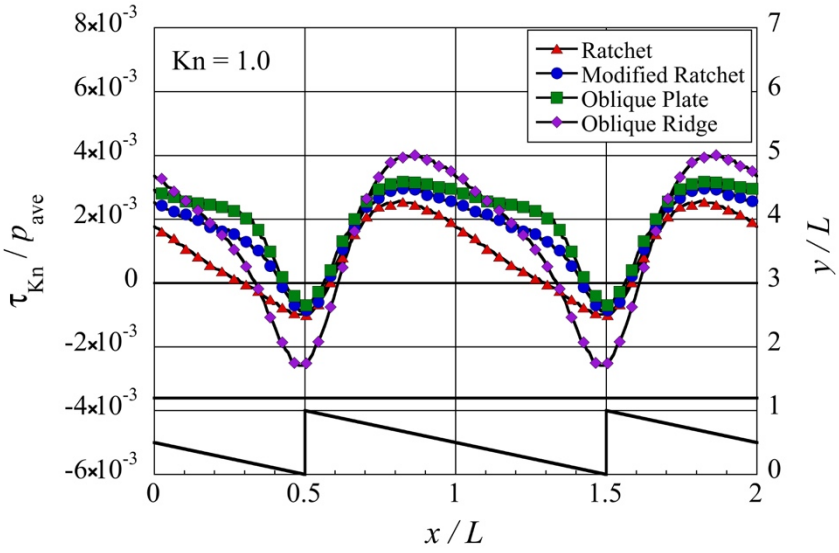

Fig. 2.6. Distribution of the local tangential Knudsen stress, i.e., local propulsive force per unit area, for each case of the microstructure, at Kn = 1. The silhouette of the ratchet structure is added for easy reference. Reprinted with permission from C. J. C. Otic and S. Yonemura, Micromachines 13, 871 (2022). Copyright 2022 Author(s).

By integrating the distribution of local tangential Knudsen stress at Kn = 1, the net tangential Knudsen stress is obtained. Figure 2.7 (a) shows the net tangential Knudsen stresses for different tip angle β under the condition of constant inclination angle $\alpha = \pi/4$. Here, the marker for $\beta = \pi/4$ represents the net tangential Knudsen stress for the ratchet, the marker for $\beta = 0$ represents that for the oblique plate, and the other markers represent those for the modified ratchet. It can be seen that at constant inclination angle $\alpha = \pi/4$, the net tangential Knudsen stress increases linearly with decreasing tip angle β. Therefore, in addition to the fact that smaller tip angles result in stronger gas flows, as mentioned previously, the smaller tip angles also result in stronger propulsive force. Next, let us investigate the relationship between the net tangential Knudsen stress and the inclination angle α by adjusting the periodic length L_P while keeping the depth d of the ratchet structure. Figure 2.7 (b) shows the resulting net tangential Knudsen stress for the ratchet for different inclination angle α, at Kn = 1. From the

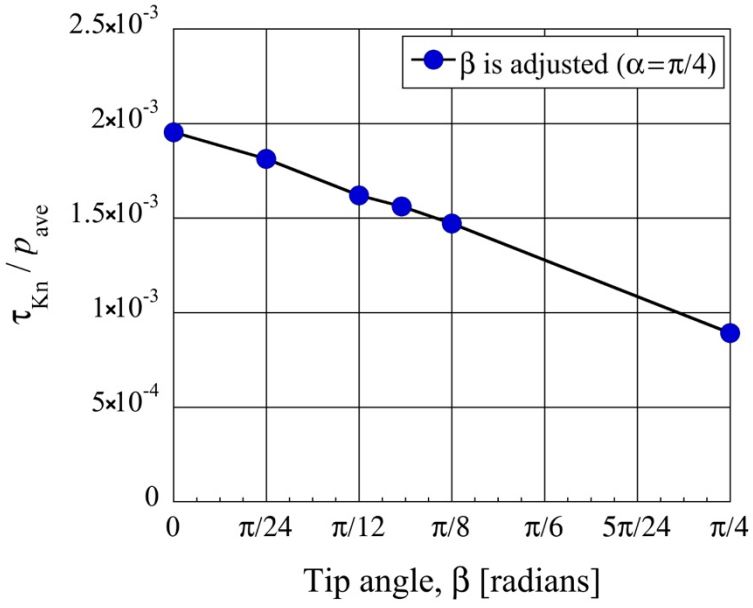

(a)

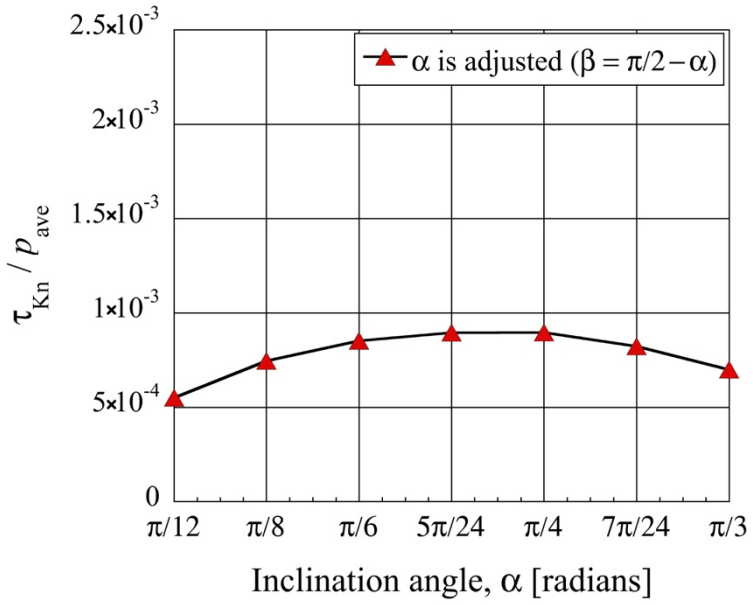

(b)

Fig. 2.7. Net tangential Knudsen stresses, i.e., propulsive forces per unit area, at (a) different tip angles β for the modified ratchet, and (b) different inclination angles α for the ratchet, for Kn = 1. Reprinted with permission from C. J. C. Otic and S. Yonemura, Micromachines 13, 871 (2022). Copyright 2022 Author(s).

plot, the maximum tangential Knudsen stress is around $\alpha = \pi/4$, or when $d = L_{\mathrm{P}}$, which is what is used in this study as a reference. Therefore, the propulsive force is maximum in the case that the aspect ratio of the microstructure is unity. As for the case $\alpha \to \pi/2$, the geometry of the microstructure approaches that of a vertical plate structure which is symmetric in the horizontal direction, and the net tangential Knudsen stress, i.e., propulsive force, vanishes. While for the case $\alpha \to 0$, the substrate approaches that of a flat surface and the tangential Knudsen stress, i.e., propulsive force, also vanishes. The results obtained here on the relationship between the inclination angle α and the tangential Knudsen stress are similar to that obtained by Donkov *et al.* [16] even though fully diffusive walls are used here, whereas they used a combination of specular and diffusive walls.

To understand how the tip angle β or how the shape of the structure, in general, affects the tangential Knudsen stress, i.e., propulsive force, let us consider two groups of molecules. First, those molecules diffusively reflected at the oblique side of the structure after impinging on it. Second, those molecules diffusively reflected at the modified side of the structure, i.e., the vertical side in the case of ratchet, after impinging on it. Note that both groups of molecules obtain higher momentum compared with molecules in bulk during the process of diffuse reflection due to the high temperature of the walls. Due to the orientation of the walls, the former group of molecules carries a $+x$-momentum, while the latter group of molecules carries a $-x$-momentum. When these two groups of molecules reach the bottom surface of the upper object without experiencing an intermolecular collision in the gas, they transfer their x-momentum onto the bottom surface of the upper object. In the case where all the molecules arriving at the bottom surface of the upper object come from the gas after experiencing intermolecular collisions there, most probably, the x-momentum brought on it is not so large. However, if some of the impinging molecules are replaced by the molecules with higher momentum directly coming from the hot sides of the microstructure, the imbalance in the x-momentum flux will be induced by such molecules, and hence, a net propulsive force will occur. The imbalance occurs based on two factors: distance from the microstructure to the bottom surface of the upper object and orientation of the modified side. When molecules travel a longer distance, they have more chance to collide with other molecules and cannot bring the x-momentum onto the bottom surface of the upper object. As the tip angle β is decreased, the distance between the surface element on the bottom surface of the upper object and the modified side increases, and hence the x-momentum carried by reflected molecules leaving the modified side also decreases. Furthermore, when the orientation of the modified side deviates from a vertical position such that it is rotated counter-clockwise, the number flux of reflected

molecules towards the bottom surface of the upper object decreases. The combination of these factors means that decreasing the tip angle β decreases the negative contribution of the second group of molecules, i.e., those that come from the modified side to the propulsive force. On the other hand, since the orientation of the oblique side is kept, i.e., α is constant, the contribution of the first group of molecules, i.e., those that come from the oblique side to the propulsive force, is unchanged. As only the negative contribution of the second group of molecules which come from the modified side is decreased, the resultant rightward force increases with decreasing tip angle β. Figure 2.8 shows the distribution of the local tangential Knudsen stress due to the first group of molecules, i.e., those coming from the oblique side of the structure, and Fig. 2.9 shows the distribution of the local tangential Knudsen stress due to the second group of molecules, i.e., those coming from the modified side of the structure. Both figures show the results for the modified ratchet. Figure 2.8 verifies our discussion above that the contribution of the first group of molecules remains unchanged at different tip angle β. However, Fig. 2.9 verifies our discussion above that the negative contribution of the second group of molecules decreases at decreasing tip angle β.

Let us look at how the propulsive force is affected by the Knudsen number. By integrating the distribution of local tangential Knudsen stress, i.e., propulsive force per unit area, the net tangential Knudsen stress is obtained at different Knudsen numbers, as shown in Fig. 2.10. It was found that a net positive tangential Knudsen stress is obtained, i.e., the propulsive force induced on the object is directed rightward or in the $+x$-direction, for all Knudsen numbers irrespective of the configuration of the microstructure. However, it is clearly seen that the magnitude of the net tangential Knudsen stress varies depending on the structure. In fact, the oblique plate induces a net tangential Knudsen stress that is about two times larger than that of the ratchet. If the configurations are ranked in terms of the strongest propulsive force, the oblique plate is followed by a modified ratchet and oblique ridge, which induce about 1.5 times larger propulsive force than that of the ratchet.

Although the magnitude of the net tangential Knudsen stress varies significantly with the type of configuration, their distribution follows a similar trend with the Knudsen number. The net propulsive force vanishes at low Knudsen numbers, $\mathrm{Kn} < 0.1$, i.e., near the continuum flow limit, peaks around $\mathrm{Kn} = 3$, i.e., in the transition flow regime, and vanishes at very high Knudsen numbers $\mathrm{Kn} > 100$, i.e., near the free molecular flow limit. To support this, consider Fig. 2.11 which shows the distribution of the local tangential Knudsen stress in the case of the ratchet microstructure. It can be seen in Fig. 2.11 (a) that at lower Knudsen numbers, i.e., $\mathrm{Kn} \leq 3$, the local tangential Knudsen stress weakens with decreasing Knudsen number. This is con-

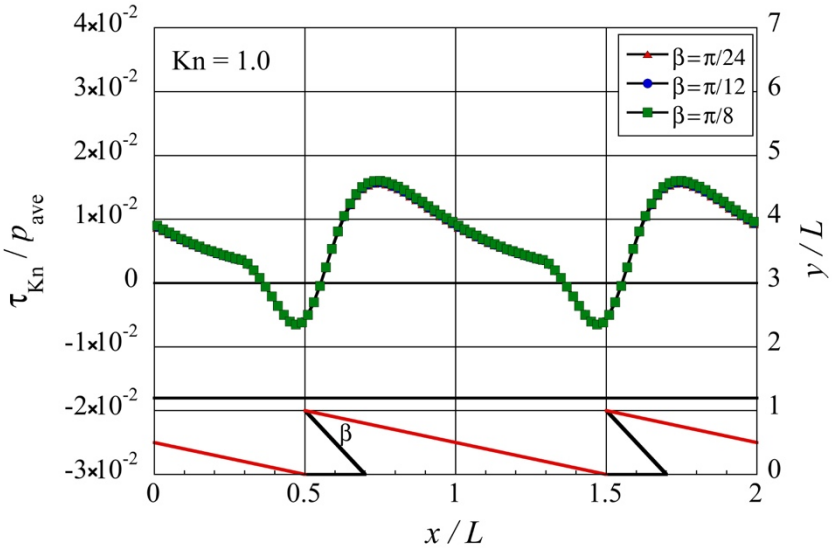

Fig. 2.8. Distributions of the local tangential Knudsen stress due to molecules coming from the oblique side of the modified ratchet microstructure, for different tip angles β at $\mathrm{Kn} = 1$. Reprinted with permission from C. J. C. Otic and S. Yonemura, Micromachines 13, 871 (2022). Copyright 2022 Author(s).

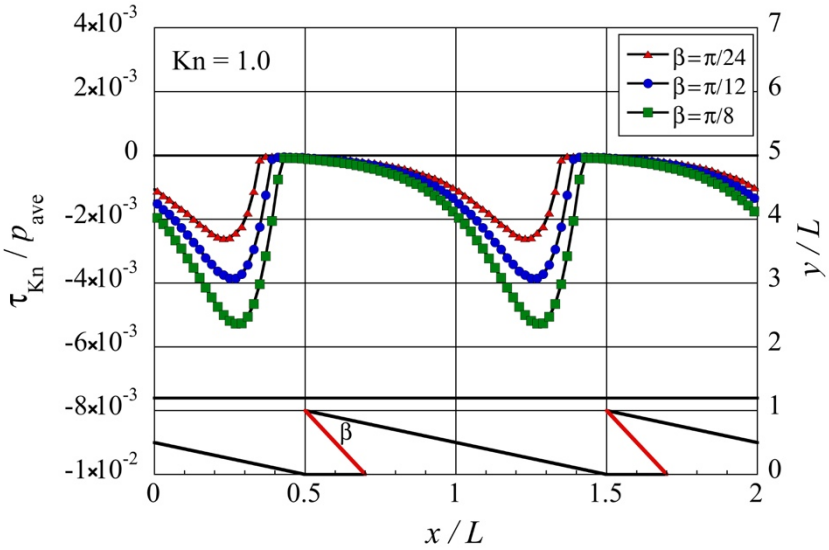

Fig. 2.9. Distributions of the local tangential Knudsen stress due to molecules coming from the modified side of the modified ratchet microstructure, for different tip angles β at $\mathrm{Kn} = 1$. Reprinted with permission from C. J. C. Otic and S. Yonemura, Micromachines 13, 871 (2022). Copyright 2022 Author(s).

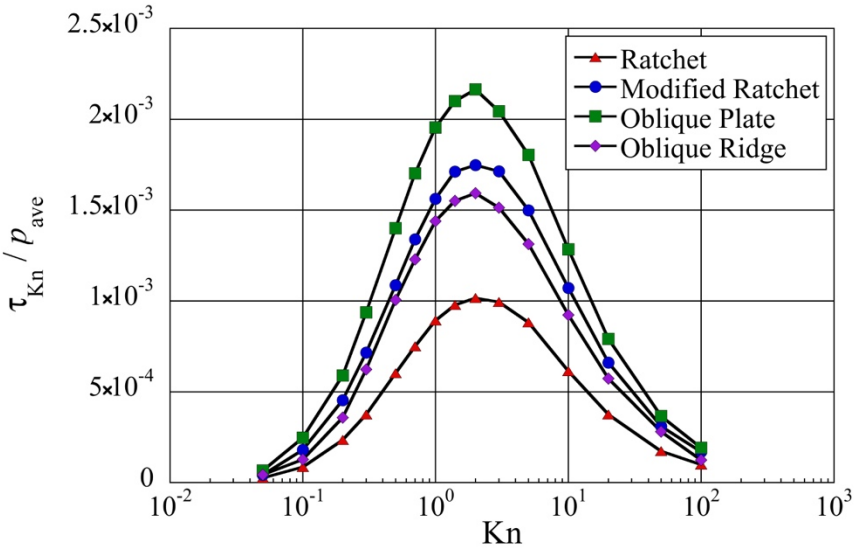

Fig. 2.10. Net tangential Knudsen stresses, i.e., propulsive forces per unit area, at different Knudsen numbers for different surface microstructures. Reprinted with permission from C. J. C. Otic and S. Yonemura, Micromachines 13, 871 (2022). Copyright 2022 Author(s).

sistent with the fact that in the continuum flow regime, i.e., $\mathrm{Kn} \to 0$, the gas is in equilibrium condition, and hence, the thermally induced flows and tangential Knudsen stress vanish. Furthermore, Fig. 2.11 (b) shows that at higher Knudsen numbers, i.e., $\mathrm{Kn} \geq 3$, the local tangential Knudsen stress weakens with increasing Knudsen number. This agrees with the work of Donkov *et al.* [16], where it is mentioned that in the case of a channel bounded by fully diffusive surfaces, the tangential Knudsen stress vanishes in the free-molecular flow regime, i.e., $\mathrm{Kn} \to \infty$. Although the distributions in Fig. 2.11 are for the ratchet microstructure, the same trend can be seen in the cases of the other microstructures presented in this study.

Lastly, let us look at the effect of the temperature difference between the heated microstructure and the colder upper object, i.e., $T_\mathrm{h} - T_\mathrm{c}$, on the net propulsive force. Figure 2.12 shows the distribution of the net propulsive force in each of the microstructures at various temperature differences, at $\mathrm{Kn} = 1$, where the temperature difference $T_\mathrm{h} - T_\mathrm{c}$ is changed while the middle value $(T_\mathrm{h} + T_\mathrm{c})/2$ between the surface temperatures T_c and T_h is kept at 400 K. It can be seen that in the case of no temperature difference, i.e., $T_\mathrm{h} = T_\mathrm{c}$, the net tangential Knudsen stress vanishes in all the microstructures. As the temperature difference is increased, the net tangential Knudsen stress increases linearly, whose slope varies depending on the microstructure. Here, the oblique plate has the largest slope, followed by the modified ratchet and the oblique ridge, while the conventional ratchet has the smallest slope.

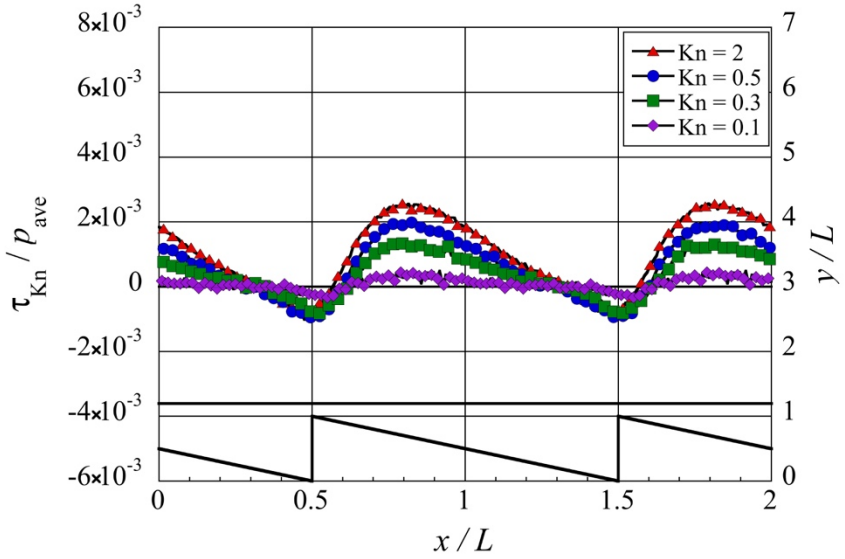

(a)

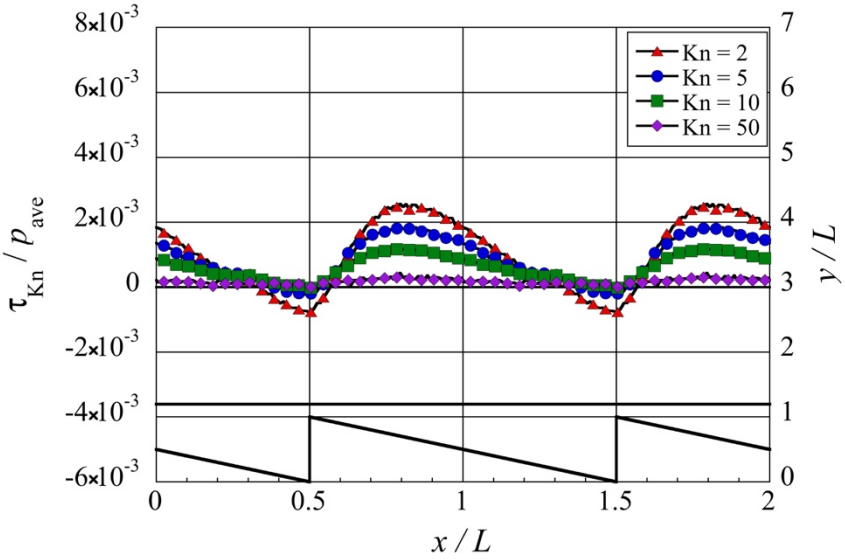

(b)

Fig. 2.11. Distributions of the local tangential Knudsen stress, i.e., local propulsive force per unit area, for the ratchet microstructure, at (a) selected lower Knudsen numbers, Kn ≤ 3, and (b) selected higher Knudsen numbers, Kn ≥ 3. Reprinted with permission from C. J. C. Otic and S. Yonemura, Micromachines 13, 871 (2022). Copyright 2022 Author(s).

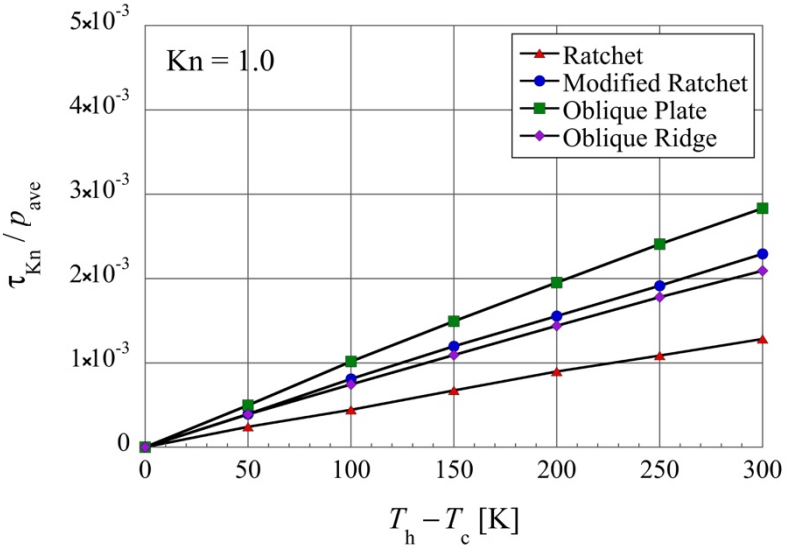

Fig. 2.12. Net tangential Knudsen stresses, i.e., propulsive forces per unit area, for different surface microstructures at different temperature differences, in the case of $\mathrm{Kn} = 1$ and $(T_\mathrm{h} + T_\mathrm{c})/2 = 400\ \mathrm{K}$. Reprinted with permission from C. J. C. Otic and S. Yonemura, Micromachines 13, 871 (2022). Copyright 2022 Author(s).

In this study, it is shown that the self-propulsion phenomenon is optimized in the case of the oblique plate configuration. From the perspective of manufacturing, a structure with no thickness is difficult, and so an oblique ridge is an alternative to the oblique plate, where the induced propulsive force is still stronger than the conventional ratchet microstructure.

2.4 Conclusion

In this study, four surface microstructures were considered, one of which is the conventional ratchet configuration, and the three configurations are modifications of the ratchet. Using the DSMC method, it was demonstrated that these new configurations can induce stronger thermally driven gas flows and a larger propulsive force on the object placed close to them. The differences in the induced flows among these microstructures are due to the fact that these new configurations have smaller tip angles than the ratchet configuration, which results in stronger thermal edge flows. Similarly, the differences in the propulsive force among these microstructures are also attributed to their differences in the tip angle. That is, for smaller tip angles, the negative contribution to the rightward propulsive force due to molecules impinging on the bottom surface of the upper object directly from the modified side without experiencing intermolecular collision is reduced, and as a result, the rightward propulsive force increases with decreasing tip angle. In addition to the fact that the magnitude of the propulsive force depends on the microstructure, the Knudsen number and the temperature difference also significantly affect the propulsive force. For all the microstructures considered in this study, it was found that the propulsive force vanishes near the continuum flow regime and near the free molecular flow regime and is maximum in the transition flow regime. Furthermore, it was also found that for all the microstructures considered here, the propulsive force increases linearly with the increasing temperature difference between the heated microstructure and the colder object. The results show that although the oblique plate microstructure induces the strongest propulsive force, both the modified ratchet and oblique ridge microstructures still induce a stronger propulsive force compared to the conventional ratchet microstructure.

References

[1] Y. Sone, *Molecular Gas Dynamics: Theory, Techniques, and Applications* (Birkhauser, Boston, USA, 2007).

[2] K. Aoki, S. Takata, and H. Aikawa, "A rarefied gas flow caused by a discontinuous wall temperature," *Physics of Fluids* 13, 2645–2661 (2001).

[3] X. Wang, T. Su, W. Zhang, Z. Zhang, and S. Zhang, "Knudsen pumps: A review," *Microsystems & Nanoengineering* 6, 26 (2020).

[4] A. Ebrahimi and E. Roohi, "DSMC investigation of rarefied gas flow through diverging micro-and nanochannels," *Microfluidics and Nanofluidics* 21, 18 (2017).

[5] Z. Zhang, X. Wang, L. Zhao, S. Zhang, and F. Zhao, "Study of flow characteristics of gas mixtures in a rectangular knudsen pump," *Micromachines* 10, 79 (2019).

[6] M. Hssikou, J. Baliti, and M. Alaoui, "Numerical analysis of non-isothermal walls driven-gas flow," *International Journal of Engineering Systems Modelling and Simulation* 10, 63–74(2018).

[7] M. Hssikou, J. Baliti, and M. Alaoui, "Continuum analysis of rarefaction effects on a thermally induced gas flow," *Mathematical Problems in Engineering* 2019, 5084098(2019).

[8] A. Lotfian and E. Roohi, "Radiometric flow in periodically patterned channels: Fluid physics and improved configurations," *Journal of Fluid Mechanics* 860, 544–576(2019).

[9] T. Baier, S. Hardt, V. Shahabi, and E. Roohi, "Knudsen pump inspired by Crookes radiometer with a specular wall," *Physical Review Fluids* 2, 033401(2017).

[10] Y. Wu, "Kinetic theory of molecular radiometric force and radiometer," *Annals of Physics* 19, 144(1967).

[11] K. Yamamoto, Y. Ishihara, and K. Fujise, "Thermophoresis of a circular cylinder in a rarefied gas," *Journal of the Physical Society of Japan* 57, 2386–2397(1988).

[12] A.L. Lereu, A. Passian, R.J. Warmack, T.L. Ferrell, and T. Thundat, "Effect of thermal variations on the Knudsen forces in the transitional regime," *Applied Physics Letters* 84, 1013(2004).

[13] Y. Sugiura, "Experimental studies on the force exerted on a disc placed in a flow of rarefied gas," *Journal of the Physical Society of Japan* 9, 244–248(1954).

[14] A. Strongrich and A. Alexeenko, "Microstructure actuation and gas sensing by the Knudsen thermal force," *Applied Physics Letters* 107, 193508(2015).

[15] A. Passian, A. Wig, F. Meriaudeau, T.L. Ferrel, and T. Thundat, "Knudsen forces on microcantilevers," *Journal of Applied Physics* 92, 6326(2002).

[16] A. Donkov, S. Tiwari, S. Liang, S. Hardt, A. Klar, and W. Ye, "Momentum and mass fluxes in a gas confined between periodically structured surfaces at different temperatures," *Physical Review E* 84, 016304(2011).

[17] S. Hardt, S. Tiwari, and T. Baier, "Thermally driven flows between a Leidenfrost solid and a ratchet surface," *Physical Review E* 87, 063015(2013).

[18] V. Shahabi, T. Baier, E. Roohi, and S. Hardt, "Thermally induced gas flows in ratchet channels with diffuse and specular boundaries," *Scientific Reports* 7, 41412(2017).

[19] A. Würger, "Leidenfrost gas ratchets driven by thermal creep," *Physical Review Letters* 107, 164502(2011).

[20] G.A. Bird, *Molecular Gas Dynamics and the Direct Simulation of Gas Flows* (Oxford, USA, 1994).

[21] K. Nanbu, " Direct simulation scheme derived from the Boltzmann equation I. Monocomponent gases," *Journal of the Physical Society of Japan* 49, 2042–2049(1980).

[22] W. Vincenti and C. Kruger Jr., *Introduction to Physical Gas Dynamics* (Krieger Publishing Company, Malabar, USA, 1965).

[23] National Astronomical Observatory of Japan, *Rika Nenpyo: Chronological Scientific Tables 2007* (Maruzen, Tokyo, Japan, 2006). (In Japanese)

[24] G. Kaye and T. Laby, *Tables of Physical and Chemical Constant* (Longman, New York, USA, 1986).

[25] K. Nanbu, "Stochastic solution method of the Boltzmann equation I," *The Memoirs the Institute of Fluid Science* 3, 47–93(1992).

[26] K. Nanbu, “Probability theory of electron–molecule, ion–molecule, molecule–molecule, and Coulomb collisions for particle modeling of materials processing plasmas and cases,” *IEEE Transactions on Plasma Science* 28, 971–990(2000).

Chapter 3 Consideration about the Mechanism of Tangential Knudsen Force Using Theoretical Analysis

3.1 Introduction

The quest to understanding thermally driven forces goes back to 1874 when Crookes' radiometer has shown that a small mill inside a vacuum chamber can be powered by light[1]. It became a subject of intense investigation by some prominent researchers, including Reynolds who measured the force[2] and Einstein who qualitatively formulated an equation of the force[3]. This force was called radiometric, and is a result of a combination of several thermally induced phenomenon occurring at rarefied gas conditions[4–5]. In addition, another phenomenon similar to this is the thermophoretic force where a tiny particle moves in gas with strong temperature gradients[6–7]. As these thermally induced forces appear under the condition that the Knudsen number is not vanishingly small, they fall in the category of Knudsen forces[8–15]. The fluid physics behind thermally induced forces have captured the curiosity of many researchers over the years[5,8,11–13,16–20]. Although it has been decades since their discoveries, Knudsen forces remain significant today[21–25], thanks partly to recent advancements in micro/nano-technologies[9–10,13–15]. Therefore, in-depth investigation on the mechanism of the Knudsen forces is increasingly becoming significant. The rigorous theoretical studies like those of Passian *et al*. [8], Scandurra *et al*. [11], and Zhu and Ye[12], among others, have shown promising results to better understand the mechanism of Knudsen forces. However, these studies have focused on the particular configuration of thin plates or microcantilevers placed close to a flat surface. Specifically, they were interested in the normal component of the Knudsen force.

Discussions are based mainly on C.J.C. Otic and S. Yonemura, "Mechanism of tangential Knudsen force at different Knudsen numbers," *Physics of Fluids* 34, 072010 (2022).

Research studies on thermally driven flows at rarefied gas conditions have shown that in ratchet-shaped channels, the Knudsen force generated on the solid boundaries not only has a normal component but also a tangential component[17–18,26–31]. Although most of these studies have focused on the conventional ratchet-type channel, simple modifications on the configuration of the channel can lead to stronger Knudsen forces[18,32]. Here, this tangential component of the Knudsen force is simply called tangential Knudsen force, i.e., the thermally induced force acting tangentially on the surface of interest. The role of the tangential Knudsen force on the self-propulsion of a Leidenfrost object placed on a heated ratchet surface was a subject of several investigations[26–27]. Although there was a debate about whether the contribution of such force is significant in the Leidenfrost effect or not, the results in Refs. 26 and 27 suggested that under the right conditions, the tangential Knudsen force can induce self-propulsion on a solid object. Furthermore, in the generation of the tangential Knudsen force, heat is converted into mechanical energy, which can provide relatively large available forces[33], and is a novel concept for energy conversion that is outside the common volumetric expansion systems[28]. Despite the potential applications, clarification is still needed on the mechanisms of the tangential Knudsen force and which mechanism is dominant at specific operational regimes. Compared to the normal component of the Knudsen force, theoretical studies on the tangential Knudsen force and its mechanism are still lacking, or at least there is still room to provide clarity. Some studies have attempted to explain the mechanism qualitatively[18,29,32–33], and those that did rigorous theoretical analysis arrived in formulations that are only applicable to specific cases, such as the case when the bounding surfaces are not fully diffusive, and limited to the molecular flow regime[17,30], and such as the case with the moving walls[28,31]. The limitations of these studies means that they are not suitable when the substrate surfaces are fully diffusive, as in the case of common materials, and when the flow is not in the free molecular flow regime. Although it has already been suggested that the asymmetry of the structure is the origin of the tangential Knudsen force[17–18], due to the limitations of the above studies there is still a need for more clarification on its mechanism that is backed by rigorous theoretical analysis, particularly in the transition flow regime and fully diffusive surfaces.

In Chap. 2, the tangential Knudsen force induced by various surface structures on an object placed close to it was calculated using the direct simulation Monte Carlo (DSMC) method[34]. Specifically, an infinitely wide object of cold temperature T_c was considered to be placed close to an infinitely wide substrate of hot temperature T_h, which has a surface structure repeated periodically along its surface. There were four configurations considered as the surface

structures, and one of them is the conventionally used ratchet configuration shown in Fig. 3.1. The ratchet configuration is defined by a periodic length, L_P, a depth, d, and a gap distance, g. The tangential Knudsen force induced on the bottom surface of the upper object for the ratchet configuration was presented in Chap. 2. The aim of this chapter is to clarify the mechanism of the tangential force theoretically. Specifically, in this chapter, a theoretical analysis on the tangential Knudsen force is presented using a thorough and comprehensive investigation of the momentum flux brought by incident molecules on the bottom surface of the upper object, under the condition of fully diffusive surfaces and for all Knudsen numbers. The theoretical results are compared with the results of the DSMC simulations obtained in the previous chapter, and the mechanism of the tangential Knudsen force is clarified. In this chapter, let us call the bottom surface of the upper object in Fig. 3.1 simply as "upper surface".

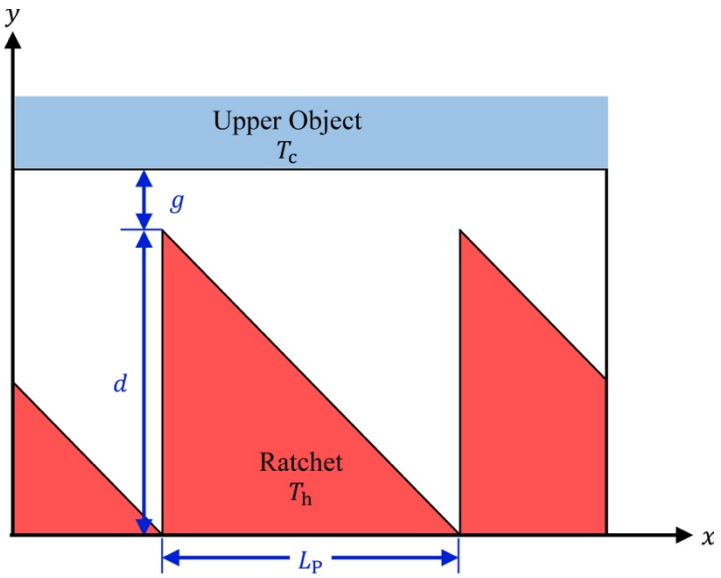

Fig. 3.1. Schematic of an object placed close to a heated ratchet surface as considered in the DSMC simulation of Chap. 2. Reprinted with permission from C. J. C. Otic and S. Yonemura, Physics of Fluids 34, 072010 (2022). Copyright 2022 Author(s).

3.2 Theory

In order to clarify the mechanism of generation of the tangential Knudsen force on the upper surface, let us analyze it theoretically by focusing on the momentum transferred by molecules. Molecules impinging onto the upper surface can carry a momentum obtained when they experienced their latest collision, which may be a collision with another molecule or a collision with a solid wall. Therefore, the focus is on the latest collision of molecules before they impinge onto the upper surface. Here, the position of their latest collision is found stochastically based on their mean free path.

3.2.1 Expected value of free path of a molecule with some specific velocity

The mean free path is defined as the average of free path over all of molecules. However, the average of free path of molecules with some specific velocity will be different from the average of free path over all kinds of molecules, i.e., mean free path. Therefore, when it is expected where a molecule experienced its last intermolecular collision or where a molecule will experience its next collision, the average of free path corresponding to molecular velocity of the considered molecule should be used.

The expected number of collisions per unit time, i.e., the collision frequency ν_c, of the considered molecule with other molecules can be given by

$$\nu_c = \int_{-\infty}^{\infty}\int_{-\infty}^{\infty}\int_{-\infty}^{\infty} n\sigma_{\mathrm{T}} v_{\mathrm{rel\ to}\ \boldsymbol{c}}\, f(\boldsymbol{\zeta}) d\zeta_x d\zeta_y d\zeta_z, \tag{3.1}$$

where n is the number density of molecules, σ_{T} is the total collision cross section of molecular pairs, $\boldsymbol{\zeta} = (\zeta_x, \zeta_y, \zeta_z)$ represents the velocity of other molecules, and $v_{\mathrm{rel\ to}\ \boldsymbol{c}}$ is the speed of other molecules relative to the considered molecule with velocity $\boldsymbol{c} = (c_x, c_y, c_z)$ and given by

$$v_{\mathrm{rel\ to}\ \boldsymbol{c}} = \sqrt{(\zeta_x - c_x)^2 + (\zeta_y - c_y)^2 + (\zeta_z - c_z)^2}\,. \tag{3.2}$$

For simplicity, let us consider hard sphere molecules with constant diameter like a billiard ball. In that case, the collision frequency ν_c of the considered molecule can be rewritten as

$$\nu_c = n\sigma_{\mathrm{T}} \int_{-\infty}^{\infty}\int_{-\infty}^{\infty}\int_{-\infty}^{\infty} \upsilon_{\text{rel to } \boldsymbol{c}} f(\boldsymbol{\zeta}) d\zeta_x d\zeta_y d\zeta_z,$$
$$= n\sigma_{\mathrm{T}} \langle \upsilon_{\text{rel to } \boldsymbol{c}} \rangle, \tag{3.3}$$

where $\langle \upsilon_{\text{rel to } \boldsymbol{c}} \rangle$ represents the average of speed of other molecules relative to the considered molecule with velocity $\boldsymbol{c}$ and is given by

$$\langle \upsilon_{\text{rel to } \boldsymbol{c}} \rangle =$$
$$\int_{-\infty}^{\infty}\int_{-\infty}^{\infty}\int_{-\infty}^{\infty} \sqrt{(\zeta_x - c_x)^2 + \left(\zeta_y - c_y\right)^2 + (\zeta_z - c_z)^2}\, f(\boldsymbol{\zeta}) d\zeta_x d\zeta_y d\zeta_z. \tag{3.4}$$

If the direction of the coordinate system is set in such a way that the considered molecule has only one component as $\boldsymbol{c} = (c, 0, 0)$, the above equation can be rewritten as follows:

$$\langle \upsilon_{\text{rel to } \boldsymbol{c}} \rangle = \int_{-\infty}^{\infty}\int_{-\infty}^{\infty}\int_{-\infty}^{\infty} \sqrt{(\zeta_x - c)^2 + {\zeta_y}^2 + {\zeta_z}^2}\, f(\boldsymbol{\zeta}) d\zeta_x d\zeta_y d\zeta_z,$$
$$\langle \boldsymbol{\upsilon}_{\text{rel to } \boldsymbol{c}} \rangle = \int_{-\infty}^{\infty}\int_{-\infty}^{\infty}\int_{-\infty}^{\infty} \sqrt{(\zeta_x - c)^2 + {\zeta_y}^2 + {\zeta_z}^2} \left(\frac{m}{2\pi k_{\mathrm{B}} T}\right)^{3/2}$$
$$\exp\left(-\frac{m}{2k_{\mathrm{B}}T}\left({\zeta_x}^2 + {\zeta_y}^2 + {\zeta_z}^2\right)\right) d\zeta_x d\zeta_y d\zeta_z. \tag{3.5}$$

Here, it is assumed that the velocity distribution of molecules is Maxwellian. Clearly, $\langle \boldsymbol{\upsilon}_{\text{rel to } \boldsymbol{c}} \rangle$ is a function of not only the speed c of the considered molecule but also the temperature T. It is inconvenient because if the case of different temperature is considered, the relative velocity have to be recalculated. In order to apply the result obtained here regardless of temperature, let us non-dimensionalize the velocities in the above expression by dividing them by thermal velocity $\upsilon_{\mathrm{th}} = \sqrt{2k_{\mathrm{B}}T/m}$, such that $\hat{\upsilon}_{\text{rel to } \boldsymbol{c}} = \upsilon_{\text{rel to } \boldsymbol{c}}/\sqrt{2k_{\mathrm{B}}T/m}$, $\hat{c}_i = c_i/\sqrt{2k_{\mathrm{B}}T/m}$, $\hat{c} = c/\sqrt{2k_{\mathrm{B}}T/m}$, $\hat{\zeta}_i = \zeta_i/\sqrt{2k_{\mathrm{B}}T/m}$, and $d\hat{\zeta}_i = d\zeta_i/\sqrt{2k_{\mathrm{B}}T/m}$. Dividing both sides of Eq. (3.5) by thermal velocity $\sqrt{2k_{\mathrm{B}}T/m}$, results to

$$\langle \hat{\upsilon}_{\text{rel to } \boldsymbol{c}} \rangle = \left(\frac{1}{\pi}\right)^{3/2} \int_{-\infty}^{\infty}\int_{-\infty}^{\infty}\int_{-\infty}^{\infty} \sqrt{\left(\hat{\zeta}_x - \hat{c}\right)^2 + {\hat{\zeta}_y}^2 + {\hat{\zeta}_z}^2}$$
$$\exp\left(-\left({\hat{\zeta}_x}^2 + {\hat{\zeta}_y}^2 + {\hat{\zeta}_z}^2\right)\right) d\hat{\zeta}_x d\hat{\zeta}_y d\hat{\zeta}_z. \tag{3.6}$$

Thus, $\langle \hat{v}_{\mathrm{rel\ to}\ \boldsymbol{c}} \rangle$ is given as a function of molecular speed $\hat{c}$ alone. Let us make the table of $\langle \hat{v}_{\mathrm{rel\ to}\ \boldsymbol{c}} \rangle$ for the values of $\hat{c}$. Although the domain of definition of $\hat{c}$ is $0 \leq \hat{c} \leq \infty$, 7 is enough as the maximum value of $\hat{c}$. Let us vary the value of $\hat{c}$ from 0 to 7 by the increment of 0.01 for the table of $\langle \hat{v}_{\mathrm{rel\ to}\ \boldsymbol{c}} \rangle$. The $\langle \hat{v}_{\mathrm{rel\ to}\ \boldsymbol{c}} \rangle$ for some $\hat{c}$ can be obtained by interpolating the two data for two grids of $\hat{c}$ near the given $\hat{c}$. The numerical integration for the above expression should be done by using the conditions for $\hat{\zeta}_x$, $\hat{\zeta}_y$ and $\hat{\zeta}_z$ similar to those for $\hat{c}$. For example, the increment, the maximum, and the minimum for $\hat{\zeta}_x$, $\hat{\zeta}_y$ and $\hat{\zeta}_z$ should be set 0.01, 7, and -7, respectively. The choice of 7 is because $\exp(-7^2) = 5.24 \times 10^{-22}$ is small enough.

The value of $\langle v_{\mathrm{rel\ to}\ \boldsymbol{c}} \rangle$ can be given by $\langle \hat{v}_{\mathrm{rel\ to}\ \boldsymbol{c}} \rangle \cdot v_{\mathrm{th}}$. As mentioned above, the expected number of collisions per unit time of the considered molecule, ν_c, is given by $\nu_c = n\sigma_{\mathrm{T}} \langle v_{\mathrm{rel\ to}\ \boldsymbol{c}} \rangle$. Therefore, the average free path of the considered molecule with the speed c is given by

$$\lambda_c = \frac{c}{\nu_c} = \frac{c}{n\sigma_{\mathrm{T}} \langle v_{\mathrm{rel\ to}\ \boldsymbol{c}} \rangle} . \tag{3.7}$$

Note that, not the mean free path λ but this length λ_c should be used as the average of free path of a molecule with the speed c.

3.2.2 Momentum flux onto the upper surface brought by molecules leaving the lower surface without experiencing intermolecular collisions

From now, let us consider the momentum transferred by molecules impinging onto the upper surface. Those molecules are divided into two groups. One group is molecules directly coming from the other surfaces without experiencing intermolecular collisions and the other group is molecules coming from the bulk region after experiencing intermolecular collisions. In this section, the momentum transferred by the former group of molecules is considered.

As the first step, a simple case of no intermolecular collisions is considered, and then, the influence of intermolecular collisions are considered later. Consider the case that there are two surfaces, S_1 and S_2, as shown in Fig. 3.2 (a). Then, let us consider the momentum flux brought onto an infinitesimal area element $d\mathrm{S}_1$ on the surface S_1 by molecules emitted from an infinitesimal area element $d\mathrm{S}_2$ on the surface S_2. Let us set a Cartesian coordinate system O-xyz in such a way that the xz plane is parallel to the infinitesimal area element $d\mathrm{S}_1$ and the y

axis is directed in the direction of the inward normal of the infinitesimal area element $d\mathrm{S}_1$. The surface structures show two-dimensional pattern in the xy plane, which does not change in the z direction.

Let us also assume that the infinitesimal area element $d\mathrm{S}_1$ is small enough to be regarded as a point compared with the size of the surface structure. In order for a molecule with velocity $\boldsymbol{c}$ to strike the infinitesimal area element $d\mathrm{S}_1$, it must be in the cylinder which has the side surface formed by all straight lines that are parallel to the velocity $\boldsymbol{c}$ and pass through the closed curve bounding $d\mathrm{S}_1$, as shown in Fig. 3.2 (a). In order for a molecule with velocity $\boldsymbol{c} + d\boldsymbol{c}$ to strike the infinitesimal area element $d\mathrm{S}_1$, it must be in the cylinder which has the side surface formed by all straight lines that are parallel to not the velocity $\boldsymbol{c}$ but the velocity $\boldsymbol{c} + d\boldsymbol{c}$ and pass through the closed curve bounding $d\mathrm{S}_1$. However, since $d\boldsymbol{c}$ is infinitesimal and $\boldsymbol{c} + d\boldsymbol{c}$ is almost parallel to $\boldsymbol{c}$, within a finite distance from $d\mathrm{S}_1$, the region occupied by the cylinder which has the side surface formed by the straight lines parallel to $\boldsymbol{c} + d\boldsymbol{c}$ almost agrees with that occupied by the cylinder which has the side surface formed by the straight lines parallel to $\boldsymbol{c}$. Therefore, as for a molecule of class $\boldsymbol{c}$ which has a velocity in the range $\boldsymbol{c}$ to $\boldsymbol{c} + d\boldsymbol{c}$, it can be judged whether or not it will strike the infinitesimal area element $d\mathrm{S}_1$ based on whether or not it is inside the cylinder with the side surface formed by all straight lines that are parallel to the velocity $\boldsymbol{c}$ and pass through the closed curve bounding $d\mathrm{S}_1$.

Let us consider a molecule which is reflected after it strikes the infinitesimal area element $d\mathrm{S}_2$ on the surface S_2. Let us call the number density and temperature of a gas just outside $d\mathrm{S}_2$ as n_{S2o} and T_{S2o}, as shown in Fig. 3.2 (b). The number flux of molecules incident on the surface element $d\mathrm{S}_2$ is given by

$$J_{\mathrm{S2\_in}} = \frac{1}{4} n_{\mathrm{S2o}} \bar{C}_{\mathrm{S2o}} = \frac{1}{4} n_{\mathrm{S2o}} \sqrt{\frac{8k_{\mathrm{B}} T_{\mathrm{S2o}}}{\pi m}}. \tag{3.8}$$

On the other hand, the number flux of molecules reflected at the surface element $d\mathrm{S}_2$, $J_{\mathrm{S2\_ref}}$, must be equal to the number flux of incident molecules $J_{\mathrm{S2\_in}}$. Let us assume that the reflections of molecules are diffusive. In the diffuse reflection model, gas molecules impinging on the surface are assumed to be reflected with a Maxwellian velocity distribution with zero mean velocity relative to the surface as if the reflected molecules came from an imaginary gas behind the surface[34]. Here, an assumption is made that the temperature of the imaginary gas is equal to the temperature of the surface element $d\mathrm{S}_2$, T_{S2}. If the number density of imaginary gas is n_{S2}, then

$$J_{\mathrm{S2\_ref}} = \frac{1}{4} n_{\mathrm{S2}} \bar{C}_{\mathrm{S2}} = \frac{1}{4} n_{\mathrm{S2}} \sqrt{\frac{8k_{\mathrm{B}} T_{\mathrm{S2}}}{\pi m}} = \frac{1}{4} n_{\mathrm{S2o}} \sqrt{\frac{8k_{\mathrm{B}} T_{\mathrm{S2o}}}{\pi m}} = \frac{1}{4} n_{\mathrm{S2o}} \bar{C}_{\mathrm{S2o}} = J_{\mathrm{S2\_in}}. \quad (3.9)$$

From this, the number density of imaginary gas n_{S2} behind the surface element $d\mathrm{S}_2$ can be estimated by

$$n_{\mathrm{S2}} = n_{\mathrm{S2o}} \sqrt{\frac{T_{\mathrm{S2o}}}{T_{\mathrm{S2}}}}. \quad (3.10)$$

Based on this number density, the number of molecules of class $\boldsymbol{c}$ per unit time, which strike the surface element $d\mathrm{S}_1$ after leaving the element $d\mathrm{S}_2$, can be estimated.

Let us call the angle between the velocity $\boldsymbol{c}$ and the inward normal of $d\mathrm{S}_1$, i.e., the direction of the y axis, θ, as shown in Fig. 3.2 (a). The projected area of $d\mathrm{S}_1$ onto the plane perpendicular to $\boldsymbol{c}$ is given by $dA = d\mathrm{S}_1 \cos\theta$. Here, dA represents the area of a cross section perpendicular to $\boldsymbol{c}$ of the cylinder with the side surface formed by all straight lines that are parallel to the velocity $\boldsymbol{c}$ and pass through the closed curve bounding $d\mathrm{S}_1$. Since molecules of class $\boldsymbol{c}$ move a distance of $\boldsymbol{c}$ in unit time along the axis of cylinder, in the case of no intermolecular collision, the number of molecules of class $\boldsymbol{c}$ per unit time which strike the element $d\mathrm{S}_1$ after being reflected at the element $d\mathrm{S}_2$ is given by

$$\begin{aligned} dJ_{\mathrm{N}} \cdot d\mathrm{S}_1 &= n_{\mathrm{S2}} \cdot c dA \cdot f_{\mathrm{S}}(\boldsymbol{c}) d\boldsymbol{c}. \\ &= n_{\mathrm{S2}} \cdot c d\mathrm{S}_1 \cos\theta \cdot \left(\frac{m}{2\pi k_{\mathrm{B}} T_{\mathrm{S2}}}\right)^{3/2} \exp\left(-\frac{m}{2k_{\mathrm{B}} T_{\mathrm{S2}}} c^2\right) d\boldsymbol{c}. \end{aligned} \quad (3.11)$$

Since $d\boldsymbol{c}$ is infinitesimal, all of these molecules can be considered to strike the element $d\mathrm{S}_1$ carrying the momentum of $m\boldsymbol{c}$. Therefore, the momentum brought to the element $d\mathrm{S}_1$ per unit time by molecules of class $\boldsymbol{c}$ which strike the element $d\mathrm{S}_1$ after being reflected at the element $d\mathrm{S}_2$ is given by

$$d\boldsymbol{J}_{\mathrm{M}} \cdot dS_1 = m\boldsymbol{c} \cdot n_{\mathrm{S2}} \cdot c dS_1 \cos\theta \cdot \left(\frac{m}{2\pi k_{\mathrm{B}} T_{\mathrm{S2}}}\right)^{3/2} \exp\left(-\frac{m}{2k_{\mathrm{B}} T_{\mathrm{S2}}} c^2\right) dc. \quad (3.12)$$

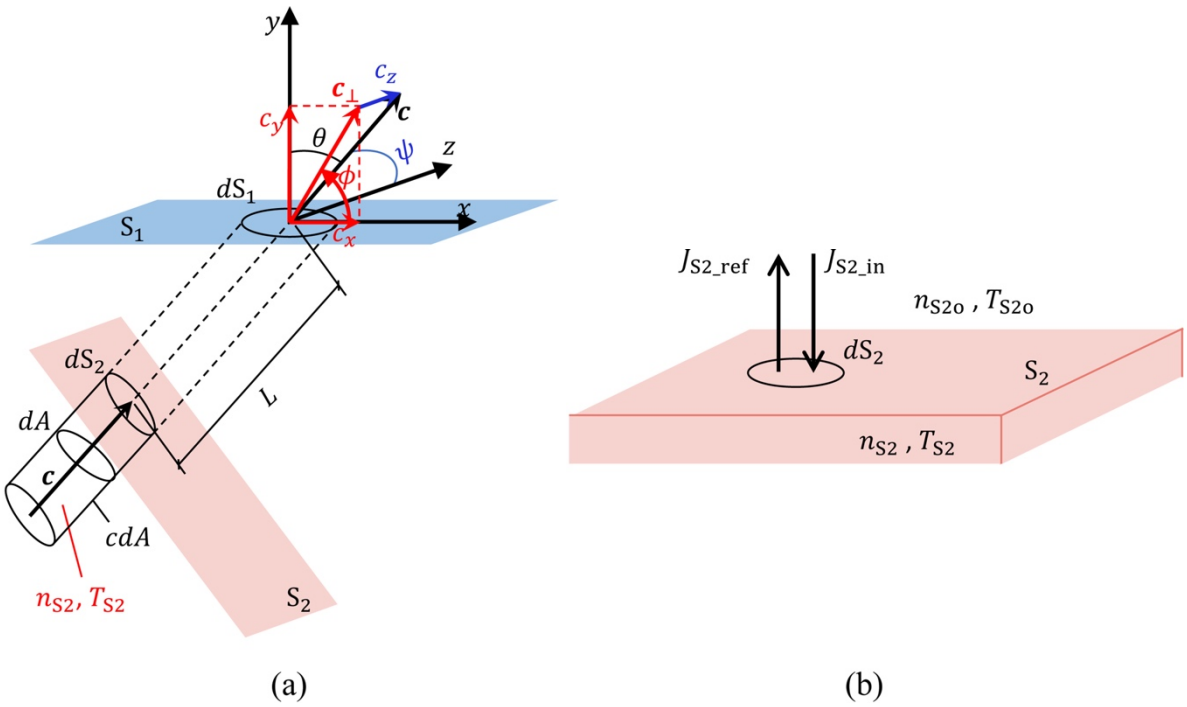

Fig. 3.2. Schematics of (a) the cylinder formed by all straight lines parallel to the velocity $\boldsymbol{c}$ that pass through the closed curve bounding dS_1 on S_1, and (b) the flux of gas molecules impinging on and leaving dS_2 on S_2. Reprinted with permission from C. J. C. Otic and S. Yonemura, Physics of Fluids 34, 072010 (2022). Copyright 2022 Author(s).

Hence, the j-momentum brought to the element dS_1 per unit time per unit area by molecules of class $\boldsymbol{c}$ which strike the element dS_1 after being reflected at the element dS_2 is given by

$$dJ_{M,j} = mc_j \cdot n_{S2} \cdot c_y \cdot \left(\frac{m}{2\pi k_B T_{S2}}\right)^{3/2} \exp\left(-\frac{m}{2k_B T_{S2}} c^2\right) dc \,, \tag{3.13}$$

where $c_y = c\cos\theta$, since θ is the angle between the velocity $\boldsymbol{c}$ and the direction of the y axis. In order to consider the j-momentum per unit time per unit area, $J_{M,j}$, brought to the element dS_1 by any kind of molecule which strikes the element dS_1 after being reflected at the element dS_2, it is only necessary to integrate $dJ_{M,j}$ over all the possible directions which is directed from some point on the surface S_2 to the surface element dS_1 and over all the possible molecular speed, i.e., over the range of $0 \leq c < \infty$. Therefore, the x-momentum per unit time per unit area, $J_{M,x}$, brought to the element dS_1 by any kind of molecule which strikes the element dS_1 after being reflected at an element dS_2 on one of wall surfaces, S_2, surrounding dS_1 is given by

$$J_{\mathrm{M},x}^{(\mathrm{wall})} = \iiint_{D_1} mc_x n_{\mathrm{S}2} c_y \left(\frac{m}{2\pi k_{\mathrm{B}} T_{\mathrm{S}2}}\right)^{3/2} \exp\left(-\frac{m}{2k_{\mathrm{B}} T_{\mathrm{S}2}} c^2\right) d\boldsymbol{c}, \tag{3.14}$$

where the superscript (wall) denotes that the momentum flux $J_{\mathrm{M},x}^{(\mathrm{wall})}$ is brought by molecules directly coming from any of the wall surfaces, while D_1 is the domain of $\boldsymbol{c}$ which represents the possible range of $\boldsymbol{c}$ of any molecule coming from the direction of one of wall surfaces to the element $d\mathrm{S}_1$. Since the surface pattern does not change in the z direction, the shape of the domain D_1 does not change in the z direction. However, the above equation is limited to the case where intermolecular collisions are not taken into account.

Let us investigate the case where intermolecular collisions exist that may interrupt molecular motion during a molecule's flight. Consider a gas in equilibrium, where the mean free path of molecules is λ. However, as mentioned in Sec. 3.2.1, the average free path λ_c of a molecule depends on its speed c and differs from the mean free path λ, and hence λ_c must be used to evaluate the fraction of molecules arriving at $d\mathrm{S}_1$ from the emission spot on the surface S_2 without experiencing intermolecular collisions. Let us consider N_0 molecules with some specific velocity $\boldsymbol{c}$ from some specific point moving toward at $d\mathrm{S}_1$. Let $N(l)$ be the number of the molecules that have not had intermolecular collisions up to the moment when they travel a distance l. The probability that such a molecule will have an intermolecular collision in going an infinitesimal distance dl is dl/λ_c. Therefore, during the motion of $N(l)$ molecules from when they travel a distance l until when they travel a distance $l + dl$, $N(l)dl/\lambda_c$ molecules will experience an intermolecular collision, and hence, the number $N(l)$ will be reduced by $N(l)dl/\lambda_c$ at the moment when they travel a distance $l + dl$. Thus,

$$N(l + dl) = N(l) - N(l)dl/\lambda_c \ , \tag{3.15a}$$

$$\Rightarrow \ dN/N = -dl/\lambda_c \ , \tag{3.15b}$$

$$\Rightarrow N(l)/N_0 = \exp\left(-l/\lambda_c\right) \ , \tag{3.15c}$$

where $dN = N(l + dl) - N(l)$ and $N(0) = N_0$ are used. From this, the fraction of molecules that have not had intermolecular collisions up to the moment when they travel a distance l is $\exp\left(-l/\lambda_c\right)$. Therefore, the fraction of molecules arriving at $d\mathrm{S}_1$ from the emission spot on the surface S_2 without experiencing intermolecular collisions is given by $\exp\left(-L/\lambda_c\right)$, where L represents the distance from the emission spot to the element $d\mathrm{S}_1$, as shown in Fig. 3.2 (a) Therefore, the momentum flux in Eq. (3.14) is rewritten to

$$J_{\mathrm{M},x}^{(\mathrm{wall})} = \iiint_{D_1} \exp\left(-L/\lambda_c\right) m c_x n_{\mathrm{S}2} c_y \left(\frac{m}{2\pi k_{\mathrm{B}} T_{\mathrm{S}2}}\right)^{3/2} \exp\left(-\frac{m}{2k_{\mathrm{B}} T_{\mathrm{S}2}} c^2\right) d\boldsymbol{c} \,. \qquad (3.16)$$

Here, note that in addition to the fact that the average free path λ_c depends on c, the distance L also depends on the direction of the velocity $\boldsymbol{c}$, i.e., L depends not only on c_x and c_y but also on c_z. Therefore, the term $\exp\left(-L/\lambda_c\right)$ cannot be taken out of the integration.

Let us call the polar angle of $\boldsymbol{c}$ as ψ, where ψ is the angle of the velocity vector $\boldsymbol{c}$ from the c_z axis in the velocity space $\mathrm{O} - c_x c_y c_z$, and let us call the azimuthal angle of $\boldsymbol{c}$ as ϕ, which is the angle between the c_x axis and the line from the origin of the velocity space $\mathrm{O} - c_x c_y c_z$ to the projection of the point $\left(c_x, c_y, c_z\right)$ on the $c_x c_y$ plane, where ϕ increases for rotations in counterclockwise orientation in the $c_x c_y$ plane. The components of $\boldsymbol{c}$ can be written in terms of ψ and ϕ, such that, $c_x = c\sin\psi\cos\phi$, $c_y = c\sin\psi\sin\phi$, and $c_z = c\cos\psi$. Thus, the Jacobian determinant for the transformation from (c, ψ, ϕ) to $\left(c_x, c_y, c_z\right)$ is given by $J = \partial\left(c_x, c_y, c_z\right)/\partial(c, \psi, \phi) = c^2\sin\psi$. Since the range of the polar angle ψ is $0 \le \psi \le \pi$, $\sin\psi \ge 0$ then $|J| = c^2\sin\psi$. The infinitesimal volume element $d\boldsymbol{c}$ in the velocity space can be expressed as $d\boldsymbol{c} = |J| dc d\psi d\phi = c^2\sin\psi\, dc d\psi d\phi$. Thus,

$$J_{\mathrm{M},x}^{(\mathrm{wall})} = \int_{\phi_1}^{\phi_2}\int_0^{\pi}\int_0^{\infty} \exp\left(-L/\lambda_c\right) m n_{\mathrm{S}2} \sin^3\psi \sin\phi\cos\phi\, c^4 \left(\frac{m}{2\pi k_{\mathrm{B}} T_{\mathrm{S}2}}\right)^{3/2} \exp\left(-\frac{m}{2k_{\mathrm{B}} T_{\mathrm{S}2}} c^2\right) dc d\psi d\phi. \qquad (3.17)$$

If $n_{\mathrm{S}2}$ is assumed uniform over the surface S_2, it can be taken out of the integration. However, note that the distance L from the emission spot to the element $d\mathrm{S}_1$ depends on the position of the emission spot, i.e., the location on S_2. Since the position of the emission spot is determined by the angles ϕ and ψ, L is a function of ϕ and ψ, and therefore the factor, $\exp\left(-L/\lambda_c\right)$, cannot be taken out of the integration.

3.2.3 Momentum flux onto the upper surface brought by molecules coming from the bulk region after experiencing intermolecular collisions there

Next, let us consider the momentum flux due to molecules colliding onto the upper surface after experiencing an intermolecular collision. Let us suppose that after each intermolecular collision, each molecule forgets its past velocity and is scattered with temperature and flow velocity at the position of the intermolecular collision. Thus, such molecules will carry the information such as temperature and flow velocity where they experience the latest intermolecular collision.

Recall that in the case when N_0 molecules with some specific velocity $\boldsymbol{c}$ are moving from some specific point toward other specific point at some specific moment, the fraction of molecules that have not had intermolecular collisions up to the moment when they travel a distance l is $N(l)/N_0 = \exp(-l/\lambda_c)$, as mentioned in Sec. 3.2.2. Hence, the fraction of molecules which experience their next collision from when they travel a distance l until when they travel a distance $l + dl$ is

$$\frac{N(l)}{N_0} - \frac{N(l+dl)}{N_0} = \frac{N(l)}{N_0} \cdot \frac{dl}{\lambda_c} = \frac{\exp(-l/\lambda_c)}{\lambda_c} dl, \tag{3.18}$$

where the relation, $N(l + dl) = N(l) - N(l)dl/\lambda_c$, obtained in Eq. (3.15a) is used. Thus, the probability density function of the distance which a molecule travels until when it experiences its next collision in the future after the current time is given by $f_l(l) = \exp(-l/\lambda_c)/\lambda_c$.

Next let us investigate the probability density function of the distance which a molecule has traveled since its last intermolecular collision until the current time. Note that a molecule with some specific velocity $\boldsymbol{c}$ will collide with one of molecules whose velocity is in the range $\boldsymbol{\zeta}$ to $\boldsymbol{\zeta} + d\boldsymbol{\zeta}$ within dt in future is given by $\sigma_T v_{\mathrm{rel\,to}\,\boldsymbol{c}} dt \cdot nf(\boldsymbol{\zeta})d\boldsymbol{\zeta}$, which was used to derive the collision frequency ν_c of a molecule with velocity $\boldsymbol{c}$ in Eq. (1), where $v_{\mathrm{rel\,to}\,\boldsymbol{c}}$ is the relative speed given by $v_{\mathrm{rel\,to}\,\boldsymbol{c}} = |\boldsymbol{\zeta} - \boldsymbol{c}|$. Similarly to this, the probability that a molecule, which currently has a velocity $\boldsymbol{c}$, collided with one of molecules, which currently have a velocity in the range $\boldsymbol{\zeta}$ to $\boldsymbol{\zeta} + d\boldsymbol{\zeta}$, within dt in the past is also given by $\sigma_T v_{\mathrm{rel\,to}\,\boldsymbol{c}} dt \cdot nf(\boldsymbol{\zeta})d\boldsymbol{\zeta}$. This is under the assumption that molecules in the range $\boldsymbol{\zeta}$ to $\boldsymbol{\zeta} + d\boldsymbol{\zeta}$ are distributed uniformly within a small region on the order of mean free path. Thus, how a molecule experienced intermolecular collisions in the past is similar to how a molecule will experience intermolecular collisions in the future. Due to this symmetry with respect to time, the probability density function of the

distance l which a molecule has traveled since its last intermolecular collision until the current time is also given by $f_l(l) = \exp(-l/\lambda_c)/\lambda_c$. Thus, the probability density function of the travel distance of a molecule from the moment of its last intermolecular collision to the current time is the same as the probability density function of the travel distance of a molecule from the current time to the moment of its next intermolecular collision. This fact suggests that intermolecular collisions in the past can be considered similar to intermolecular collisions in the future.

Let us consider the simple case when the gas surrounding the element dS_1 is in equilibrium of number density n_g and temperature T_g. The number of molecules of class $\boldsymbol{c}$ striking at dS_1 within unit time is given by

$$n_g \cdot cdA \cdot f_g(\boldsymbol{c})d\boldsymbol{c} = n_g \cdot cdS_1 \cos\theta \cdot \left(\frac{m}{2\pi k_B T_g}\right)^{3/2} \exp\left(-\frac{m}{2k_B T_g}c^2\right) d\boldsymbol{c}\,, \qquad (3.19)$$

where dA is the area of a cross section perpendicular to $\boldsymbol{c}$ of the cylinder which has the side surface formed by all straight lines that are parallel to the velocity $\boldsymbol{c}$ and pass through the closed curve bounding dS_1, and hence, dA is given by $dA = dS_1 \cos\theta$, and θ is the angle between the velocity $\boldsymbol{c}$ and the inward normal of dS_1, as seen in Fig. 3.3 (a). Since the probability density function of the travel distance l of a molecule from the moment of its last intermolecular collision to the current time is given by $f_l(l) = \exp(-l/\lambda_c)/\lambda_c$, the fraction of the molecules of class $\boldsymbol{c}$ which directly strikes dS_1 after experiencing an intermolecular collision in the region between l and $l + dl$ inside the above-mentioned cylinder, where l is the distance from dS_1 as shown in Fig. 3.3 (b), out of all the molecules of class $\boldsymbol{c}$ striking dS_1 coming from anywhere inside the above-mentioned cylinder is given by $f_l(l)dl = \exp(-l/\lambda_c)dl/\lambda_c$. Therefore, the number of the molecules of class $\boldsymbol{c}$ which directly strikes dS_1 after experiencing an intermolecular collision in the region between l and $l + dl$ inside the above-mentioned cylinder is given by

$$f_l(l)dl \cdot n_g \cdot cdA \cdot f_g(\boldsymbol{c})d\boldsymbol{c} = \exp(-l/\lambda_c)\frac{dl}{\lambda_c} \cdot n_g \cdot cdS_1 \cos\theta \cdot \left(\frac{m}{2\pi k_B T_g}\right)^{3/2} \exp\left(-\frac{m}{2k_B T_g}c^2\right) d\boldsymbol{c}\,. \qquad (3.20)$$

Since $d\boldsymbol{c}$ is infinitesimal, all of these molecules can be considered to bring the momentum of $m\boldsymbol{c}$ to the element dS_1. Hence, the momentum brought to dS_1 by the molecules of class $\boldsymbol{c}$

which directly strikes dS_1 after experiencing an intermolecular collision in the region between l and $l + dl$ inside the above-mentioned cylinder is given by

$$f_l(l)dl \cdot m\boldsymbol{c} \cdot n_g \cdot cdA \cdot f_g(\boldsymbol{c})d\boldsymbol{c} =$$

$$\exp(-l/\lambda_c)\frac{dl}{\lambda_c} \cdot m\boldsymbol{c} \cdot n_g \cdot cdS_1 \cos\theta \cdot \left(\frac{m}{2\pi k_B T_g}\right)^{3/2} \exp\left(-\frac{m}{2k_B T_g}c^2\right) d\boldsymbol{c} . \quad (3.21)$$

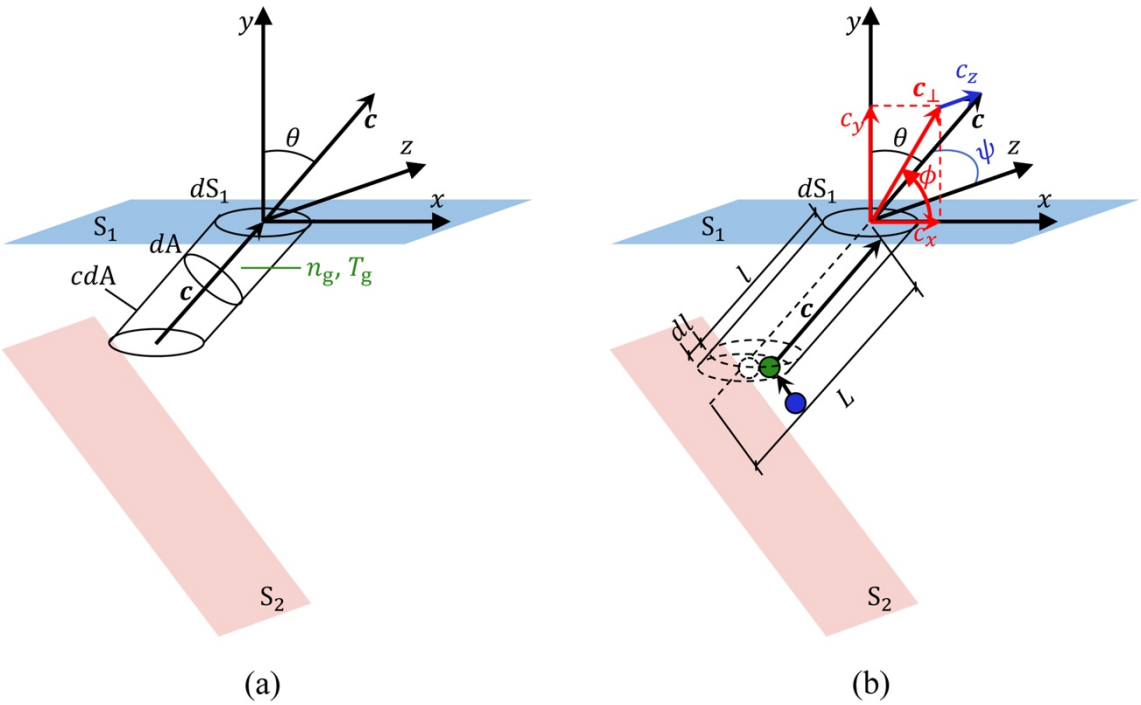

Fig. 3.3. Schematics of (a) the cylinder containing all of molecules of class $\boldsymbol{c}$, which directly strike dS_1 within unit time unless they experience intermolecular collisions, and (b) the region where molecules of class $\boldsymbol{c}$ which directly strike dS_1 experienced their latest intermolecular collision. Reprinted with permission from C. J. C. Otic and S. Yonemura, Physics of Fluids 34, 072010 (2022). Copyright 2022 Author(s).

The momentum brought to dS_1 by the molecules of class $\boldsymbol{c}$ which directly strikes dS_1 after experiencing an intermolecular collision anywhere in the above-mentioned cylinder within the bulk region of gas is given by

$$\int_0^L f_l(l) \cdot m\boldsymbol{c} \cdot n_g \cdot cdA \cdot f_g(\boldsymbol{c})d\boldsymbol{c}\, dl =$$

$$\int_0^L \frac{\exp(-l/\lambda_c)}{\lambda_c} \cdot m\boldsymbol{c} \cdot n_g \cdot cdS_1 \cos\theta \cdot \left(\frac{m}{2\pi k_B T_g}\right)^{3/2} \exp\left(-\frac{m}{2k_B T_g}c^2\right) d\boldsymbol{c}dl . \quad (3.22)$$

Here, L represents the distance from the element dS_1 to the area element on the other wall in the direction of $-\boldsymbol{c}$, as also illustrated in Fig. 3.3 (b). Next, let us consider all kinds of molecules which can strike dS_1. To consider them, it is only necessary to integrate the above expression over all possible molecular velocity. Hence, the momentum brought to dS_1 by the molecules which directly strikes dS_1 after experiencing an intermolecular collision anywhere in the bulk region of gas is given by

$$\int_{\text{possible } \boldsymbol{c}} \int_0^L f_l(l) \cdot m\boldsymbol{c} \cdot n_\mathrm{g} \cdot cdA \cdot f_\mathrm{g}(\boldsymbol{c}) dl d\boldsymbol{c} = \int_{\text{possible } \boldsymbol{c}} \int_0^L \frac{\exp(-l/\lambda_c)}{\lambda_c} \cdot m\boldsymbol{c} \cdot n_\mathrm{g} \cdot cdS_1 \cos\theta \cdot \left(\frac{m}{2\pi k_\mathrm{B} T_\mathrm{g}}\right)^{3/2} \exp\left(-\frac{m}{2k_\mathrm{B} T_\mathrm{g}} c^2\right) dl d\boldsymbol{c} \,. \tag{3.23}$$

The momentum flux $\boldsymbol{J}_\mathrm{M}^{(\mathrm{gas})}$ onto dS_1 due to the molecules which directly strikes dS_1 after experiencing an intermolecular collision anywhere in the bulk region of gas is given by

$$\begin{aligned} \boldsymbol{J}_\mathrm{M}^{(\mathrm{gas})} &= \int_{\text{possible } \boldsymbol{c}} \int_0^L f_l(l) \cdot m\boldsymbol{c} \cdot n_\mathrm{g} \cdot c\cos\theta \cdot f_\mathrm{g}(\boldsymbol{c}) dl d\boldsymbol{c} \\ &= \int_{\text{possible } \boldsymbol{c}} \int_0^L \frac{\exp(-l/\lambda_c)}{\lambda_c} \cdot m\boldsymbol{c} \cdot n_\mathrm{g} \cdot c\cos\theta \cdot \left(\frac{m}{2\pi k_\mathrm{B} T_\mathrm{g}}\right)^{3/2} \exp\left(-\frac{m}{2k_\mathrm{B} T_\mathrm{g}} c^2\right) dl d\boldsymbol{c}, \end{aligned} \tag{3.24}$$

where the superscript (gas) denotes the flux coming from the bulk region of the gas. Consequently, the x-momentum flux, $J_{\mathrm{M},x}^{(\mathrm{gas})}$, onto dS_1 due to the molecules which directly strikes dS_1 after experiencing an intermolecular collision anywhere in the bulk region of gas is given by

$$\begin{aligned} J_{\mathrm{M},x}^{(\mathrm{gas})} &= \int_{\text{possible } \boldsymbol{c}} \int_0^L f_l(l) \cdot mc_x \cdot n_\mathrm{g} \cdot c\cos\theta \cdot f_\mathrm{g}(\boldsymbol{c}) dl d\boldsymbol{c}, \\ &= \int_{\text{possible } \boldsymbol{c}} \int_0^L \frac{\exp(-l/\lambda_c)}{\lambda_c} \cdot mc_x \cdot n_\mathrm{g} \cdot c\cos\theta \cdot \left(\frac{m}{2\pi k_\mathrm{B} T_\mathrm{g}}\right)^{3/2} \exp\left(-\frac{m}{2k_\mathrm{B} T_\mathrm{g}} c^2\right) dl d\boldsymbol{c}. \end{aligned} \tag{3.25}$$

Note that if the temperature T_{S_2} of the surface S_2 and the number density n_{S_2} of imaginary gas inside the surface S_2 are used instead of T_g and n_g, and the above expression is integrated over

the range of $L < l < \infty$, the same expression as Eq. (3.16) will be obtained for the x-momentum flux $J_{\mathrm{M},x}^{(\mathrm{wall})}$.

As what was done for $J_{\mathrm{M},x}^{(\mathrm{wall})}$, let us express the velocity $\boldsymbol{c}$ by using its magnitude c, the polar angle ψ, and the azimuthal angle ϕ. Since $d\boldsymbol{c} = |J| dc d\psi d\phi = c^2 \sin\psi \, dc d\psi d\phi$, then

$$
\begin{aligned}
J_{\mathrm{M},x}^{(\mathrm{gas})} &= \int_0^{\pi}\int_0^{\pi}\int_0^{\infty}\left[\int_0^{L}\frac{\exp\left(-l/\lambda_c\right)}{\lambda_c}dl\right] m n_{\mathrm{g}} \sin^3\psi \sin\phi\cos\phi \, c^4 \left(\frac{m}{2\pi k_{\mathrm{B}} T_{\mathrm{g}}}\right)^{3/2} \\
&\quad \exp\left(-\frac{m}{2k_{\mathrm{B}}T_{\mathrm{g}}}c^2\right) dc d\psi d\phi, \\
&= \int_0^{\pi}\int_0^{\pi}\int_0^{\infty}\{1-\exp\left(-L/\lambda_c\right)\} m n_{\mathrm{g}} \sin^3\psi \sin\phi\cos\phi \, c^4 \left(\frac{m}{2\pi k_{\mathrm{B}} T_{\mathrm{g}}}\right)^{3/2} \\
&\quad \exp\left(-\frac{m}{2k_{\mathrm{B}}T_{\mathrm{g}}}c^2\right) dc d\psi d\phi. \qquad (3.26)
\end{aligned}
$$

As mentioned in Sec. 3.2.2, L is a function of ϕ and ψ, and therefore the factor, $\{1-\exp\left(-L/\lambda_c\right)\}$, cannot be taken out of the integration.

3.2.4 Total x-momentum flux onto the upper surface

So far the momentum flux brought onto the upper surface by molecules impinging on it have been considered. In addition, the contribution of not only molecules impinging on it but also molecules reflected on it has to be considered also. However, since it was assumed that the reflections of molecules are diffusive, reflected molecules will not contribute to the transfer of the tangential component of momentum. Therefore, in the case of fully diffusive wall, the sum of the x-momentum fluxes onto the upper surface brought by molecules leaving the lower surface without experiencing intermolecular collisions, $J_{\mathrm{M},x}^{(\mathrm{wall})}$, and by molecules coming from the bulk region after experiencing intermolecular collisions there, $J_{\mathrm{M},x}^{(\mathrm{gas})}$, represents the total x-momentum flux onto the surface element dS_1 at the upper surface. This is the theoretical tangential Knudsen force per unit area induced on the surface element dS_1 considered in this study.

In the construction of the $J_{\mathrm{M},x}^{(\mathrm{gas})}$ in the theory, it was assumed that incident molecules on the upper surface has a Maxwellian distribution. From the DSMC simulation of Chap. 2, at low Knudsen numbers, $\mathrm{Kn} < 1$, the velocity distribution for the molecules moving in the $+y$-

direction are close to the Maxwellian. However, the distribution deviates from the Maxwellian at high Knudsen numbers, Kn ≥ 1, but not so largely. Thus, the use of the Maxwellian distribution here is not so bad as an approximation.

3.3 Methods and parameters for theoretical analysis

In the theoretical analysis, the same situation as that considered in the DSMC simulations of Chap. 2 is considered. Specifically, the ratchet surface structure shown in Fig. 3.1 is chosen as the configuration of interest. Here, an infinitely long channel whose lower surface is defined by a ratchet structure repeated periodically in the x-direction is considered, while the upper surface is considered to be flat. The ratchet walls are heated at a temperature $T_\mathrm{h} = 500$ K, while the upper surface was set at room temperature $T_\mathrm{c} = 300$ K. Here, all solid boundaries are considered isothermal and fully diffusive. The periodic length, L_P, and the depth, d, of the ratchet are of equal lengths, i.e., $d = L_\mathrm{P}$, and the smallest gap distance, g, is set at $g = 0.2d$.

The considered gas is air consisting of imaginary hard sphere molecules with a mass of $m = 4.80967 \times 10^{-26}$ kg and a diameter of $d_\mathrm{m} = 0.356$ nm. The number density of molecules is given by that in the case when the gas is at the reference temperature of $T_\mathrm{ref} = (T_\mathrm{c} + T_\mathrm{h})/2 = 400$ K and reference gas pressure of $p_\mathrm{ref} = 1$ atm. Let us call this number density as the reference number density and it can be calculated by $n_\mathrm{ref} = p_\mathrm{ref}/k_\mathrm{B}\,T_\mathrm{ref}$, where k_B is the Boltzmann constant and is given by 1.380649×10^{-23} J/K. From the diameter of molecules and the reference number density, the mean free path for gas molecules was evaluated as $\lambda_\mathrm{ref} = 96.79697\cdots$ nm. Let us define the Knudsen number here as Kn $= \lambda_\mathrm{ref}/g$, where the gap g is chosen as the characteristic length. As was done in the DSMC simulations, the setting value of Knudsen numbers was changed as 0.05, 0.1, 0.2, 0.3, 0.5, 0.7, 1.0, 1.4, 2, 3, 5, 10, 20, 50, and 100. Similarly to the numerical simulations in Chap. 2, the Knudsen number was adjusted by adjusting the gap g as $g = \lambda_\mathrm{ref}/\mathrm{Kn}$, while keeping the gas mean free path λ_ref constant, i.e., keeping the reference gas pressure p_ref constant.

Considering the upper surface as S_1 and the ratchet surface as S_2, as mentioned in Sec. 3.2.4, the superposition of the x-momentum fluxes $J_{\mathrm{M},x}^{(\mathrm{wall})} + J_{\mathrm{M},x}^{(\mathrm{gas})}$, is the theoretical tangential Knudsen force per unit area, i.e., the tangential Knudsen stress, exerted on the upper surface. Here, the integrals of Eq. (3.17) and Eq. (3.26) are evaluated numerically. Note that although the domain of definition of c is $0 \leq c \leq \infty$, $7v_\mathrm{th}$ is enough as the maximum value of c with

$dc = 0.01v_{\mathrm{th}}$, as discussed in Sec. 3.2.1. Based on this, the table of $\langle \hat{v}_{\mathrm{rel\,to}\,\boldsymbol{c}} \rangle$ was made by using Eq. (3.6). Using this table, $\langle v_{\mathrm{rel\,to}\,\boldsymbol{c}} \rangle = \langle \hat{v}_{\mathrm{rel\,to}\,\boldsymbol{c}} \rangle \cdot v_{\mathrm{th}}$ and $c = \hat{c} \cdot v_{\mathrm{th}}$, $\langle \hat{v}_{\mathrm{rel\,to}\,\boldsymbol{c}} \rangle$ for some $\hat{c}$, i.e., $\langle v_{\mathrm{rel\,to}\,\boldsymbol{c}} \rangle$ for some c, is obtained by interpolating the two data for two grids of $\hat{c}$ near the given $\hat{c}$. The average free path λ_c for some molecule with specific velocity $\boldsymbol{c}$ is calculated from Eq. (3.7) and $\langle v_{\mathrm{rel\,to}\,\boldsymbol{c}} \rangle$ obtained in the above-mentioned procedure. Furthermore, for the integration in terms of ψ over the range 0 to π, a value of $d\psi = \pi/100$ was considered. As shown in Fig. 3.4, from the viewpoint of $d\mathrm{S}_1$, the inclined walls and the vertical walls of the ratchet structure extend from $\phi = 0$ to $\phi = \pi$. It means that the number of inclined surfaces and the number of the vertical sides to be considered in the calculation of Eq. (3.17) and Eq. (3.26) are infinity. These walls are used to calculate the distances, L's, from the considered surface element $d\mathrm{S}_1$ to surface elements on these walls in the calculation of $\exp(-L/\lambda_c)$ in Eq. (3.17) and Eq. (3.26). However, as for the walls located far from the element $d\mathrm{S}_1$, the value of $\exp(-L/\lambda_c)$ becomes extremely small for $L \gg \lambda_c$, and hence, $\exp(-L/\lambda_c)$ can be neglected in the calculation of Eq. (3.17) and Eq. (3.26). Thus, the exact value of L for such walls located far from the element $d\mathrm{S}_1$ need not to be calculated. Thanks to this, the region where the exact value of L is calculated can be limited. In the present study, the bottom edge of the vertical wall is set as $y = 0$ and the center of the inclined wall is set as $x = 0$ as shown in Figs. 3.4 (a) and (b). In the case when the element $d\mathrm{S}_1$ is located in the region of $0 \le x < 0.5L_{\mathrm{P}}$, the walls within the region of $-(k + 0.5)L_{\mathrm{P}} \le x \le (k + 0.5)L_{\mathrm{P}}$ are considered to calculate the value of L, as shown in Figs. 3.4 (a) and (b), where the factor k is defined as $k = \mathrm{int}(10\lambda_{\mathrm{ref}}/L_{\mathrm{P}}) + 1$. In the case when the element $d\mathrm{S}_1$ is located in the region of $0.5L_{\mathrm{P}} \le x < L_{\mathrm{P}}$, the walls within the region of $-(k - 0.5)L_{\mathrm{P}} \le x \le (k + 1.5)L_{\mathrm{P}}$ are considered to calculate the value of L.

Let us number the walls within the above mentioned region, which can be seen from $d\mathrm{S}_1$, in order of increasing angle ϕ, where ϕ is the angle between $-x$ direction and the projection of the straight line from $d\mathrm{S}_1$ to a point visible from $d\mathrm{S}_1$ on a considered wall on to the xy plane and is the vertically opposite angle of the azimuthal angle ϕ of the velocity vector $\boldsymbol{c}$ considered in Sec. 3.2.2. The area visible from $d\mathrm{S}_1$ on the first wall is indicated as $\phi_0 < \phi < \phi_1$ with respect to ϕ, and that on the ith wall is indicated as $\phi_{i-1} < \phi < \phi_i$, and that on the last wall out of n walls is indicated as $\phi_{n-1} < \phi < \phi_n$, as shown in Fig. 3.4 (a). The x-momentum flux onto $d\mathrm{S}_1$ brought by molecules leaving the the i th wall surface without experiencing intermolecular collisions, $J_{\mathrm{M},x,i}$, is given by replacing ϕ_1 and ϕ_2 by ϕ_{i-1} and ϕ_i in Eq. (3.17). The total momentum flux onto $d\mathrm{S}_1$ brought by molecules leaving the ratchet surface without

experiencing intermolecular collisions is given by $\sum_{i=1}^{n} J_{\mathrm{M},x,i}$. The integration for $J_{\mathrm{M},x,i}$ is done numerically by using the increment of $\Delta\phi = (\phi_i - \phi_{i-1})/100$.

As for the x-momentum flux, $J_{\mathrm{M},x}^{(\mathrm{gas})}$, onto dS_1 due to the molecules which directly strikes dS_1 after experiencing an intermolecular collision anywhere in the bulk region of gas, the integration with respect to ϕ in Eq. (3.26) over the range of $0 < \phi < \pi$ is divided into the $n + 1$ integrations over $n + 1$ small ranges of $0 < \phi < \phi_0$, $\phi_0 < \phi < \phi_1$, ... , $\phi_{n-1} < \phi < \phi_n$, and $\phi_n < \phi < \pi$, as shown in Fig. 3.4 (b). Each of the integrations over these small ranges are done numerically by using the increments of $\Delta\phi = \phi_0/100$ for the first range, and $\Delta\phi = (\pi - \phi_n)/100$ for the final range, and $\Delta\phi = (\phi_i - \phi_{i-1})/100$ for other ranges. For the integration over the ranges of $0 < \phi < \phi_0$ and $\phi_n < \phi < \pi$, the term $\exp(-L/\lambda_c)$ in Eq. (3.26) is treated as zero since the walls are far enough from dS_1. By summing up the results of the integrations, the x-momentum flux, $J_{\mathrm{M},x}^{(\mathrm{gas})}$, due to the molecules which directly strikes dS_1 after experiencing an intermolecular collision anywhere in the bulk region of gas can be obtained.

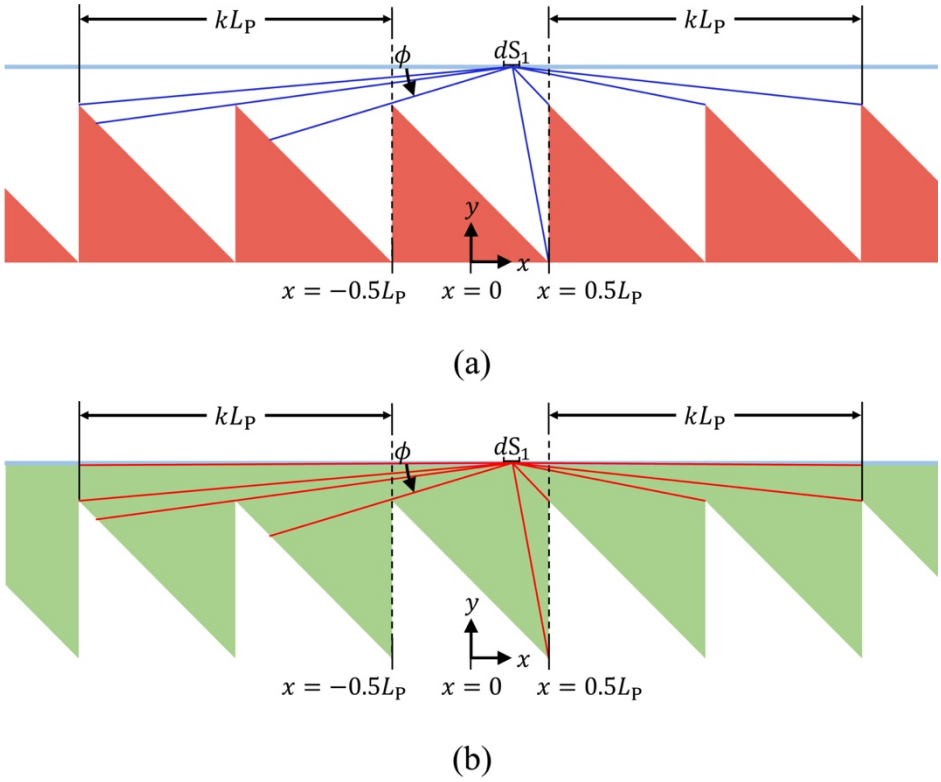

Fig. 3.4. Ranges of calculation of the theoretical expressions for the (a) wall region, and (b) gas region. Reprinted with permission from C. J. C. Otic and S. Yonemura, Physics of Fluids 34, 072010 (2022). Copyright 2022 Author(s).

3.4 Theoretical analysis

Let us denote the tangential Knudsen stress, or the tangential Knudsen force per unit area exerted on the upper surface, as τ_{Kn}. In the DSMC simulation of Chap. 2, this is the accumulated x-momentum transferred by impinging molecules on the upper surface, while in the theoretical analysis here, this is the sum of the x-momentum fluxes $J_{\mathrm{M},x}^{(\mathrm{wall})} + J_{\mathrm{M},x}^{(\mathrm{gas})}$. For reference, let us focus first our investigation for the case of $\mathrm{Kn} = 1$. Figure 3.5 shows the distribution of the local tangential Knudsen stresses obtained by theoretical analysis and that obtained in the DSMC simulations of Chap. 2. Here, the tangential Knudsen stresses are normalized by p_{ave}, which is the pressure spatially averaged in the whole region of the gas. A positive tangential Knudsen stress represents that the tangential Knudsen force is directed rightward, i.e., $+x$-direction, while a negative tangential Knudsen stress represents that the tangential Knudsen force is directed leftward, i.e., $-x$-direction. The plot shows a non-uniform distribution of the local tangential Knudsen stress. At locations on the upper surface that are directly above the ratchet tip, the tangential Knudsen stress is negative, i.e., the force is directed leftward on the object. However, away from the ratchet tip, the tangential Knudsen force drastically shifts to positive, i.e., the force is directed rightward on the object. By integrating the distribution of local tangential Knudsen stress over all sections of the upper surface, a positive average tangential Knudsen stress is obtained, i.e., the net tangential Knudsen force on the upper surface is directed rightward.

Now, let us compare our theoretical results with that of the DSMC simulation. Firstly, it has to be emphasized that a uniform gas density $n_{\mathrm{g}} = n_{\mathrm{ave}}$ and gas temperature $T_{\mathrm{g}} = T_{\mathrm{ave}}$ is assumed in calculating $J_{\mathrm{M},x}^{(\mathrm{wall})} + J_{\mathrm{M},x}^{(\mathrm{gas})}$. Here, n_{ave} and T_{ave} are the average number density and the average gas temperature obtained in the DSMC simulation, respectively, and were obtained by spatially averaging the local number density and the local gas temperature in the whole region of the gas. Furthermore, the imaginary number density n_{S2}, calculated using Eq. (3.10), is also assumed uniform throughout the ratchet wall surface with the assumption that $n_{\mathrm{S2o}} = n_{\mathrm{ave}}$ and $T_{\mathrm{S2o}} = T_{\mathrm{ave}}$. The resulting distribution of the local tangential Knudsen stress based on our theoretical expression is plotted in Fig. 3.5, where the results obtained in the DSMC simulations of Chap. 2 are also plotted. It can be seen from Fig. 3.5 that the distribution of the Knudsen stress obtained in our theoretical analysis agrees well with that of the DSMC simulation. However, there are some disparity in terms of magnitude between the theoretical results and the DSMC results, especially at the surfaces above the inclined part of the ratchet.

To understand this, note that in theoretical analysis, it was assumed that the density and temperature in the gas are uniform and that the gas is at rest. However, due to the temperature difference between the bounding surfaces, temperature distribution can be induced in the gas. Furthermore, temperature distributions in slightly rarefied gas can lead to thermally driven gas flows[36–39]. Therefore, our assumption of uniform temperature and stationary gas may not be enough to accurately describe the tangential Knudsen force. This might be why our theoretical tangential Knudsen stress deviates from that obtained by DSMC simulation, at least so far for $\mathrm{Kn} = 1$.

Let us look at the resulting temperature and velocity distribution from the DSMC simulation of Chap. 2 for $\mathrm{Kn} = 1$ in Fig. 3.6. As expected, the non-uniform temperature distribution induces thermally driven flows which result to gas flows in the bulk region. A strong clockwise vortex can be seen in the large region above the inclined part of the ratchet and a weaker counterclockwise vortex can be seen in the small region immediately to the right of the ratchet tip. From the viscous flow perspective, the presence of gas flows in the upper region of the channel can induce viscous shear stress, such that a flow in the $+x$-direction can induce a positive shear force and a flow in the $-x$-direction can induce a negative shear force. By comparing Fig. 3.5 and Fig. 3.6, it can be seen that in regions where the flow is directed in the $+x$-direction, the local tangential Knudsen stress obtained from DSMC is larger than that from our theory, and where the flow is directed in the $-x$-direction, the opposite is true. As mentioned, the resulting velocity distribution in the bulk region of the gas was not considered in our theoretical analysis. From these, it can be deduced that the disparity in the tangential Knudsen stress between the DSMC result and our theory may be caused by the viscous effect of the flow. To validate this deduction, let us calculate the contribution of the flow, i.e., the viscous shear stress, to the local tangential Knudsen stress. On the average, molecules that are impinging on the upper surface carry the x-momentum per molecule which prevails at a distance of one mean free path λ_{ref} below the upper surface. According to Vincenti and Kruger Jr.[35], the viscous shear stress can be expressed by

$$\tau_{\mathrm{flow}} = \frac{1}{4} mn\bar{C} u_{\lambda_{\mathrm{ref}}} . \tag{3.27}$$

Here, $\bar{C}$ is the mean molecular speed and $u_{\lambda_{\mathrm{ref}}}$ is the average x-velocity of molecules taken from the gas region located λ_{ref} below the upper surface. The above viscous shear stress is considered as the estimated contribution of the flow to the tangential Knudsen stress, τ_{Kn}, and is shown as “flow effect” in Fig. 3.7(a). The superposition of the flow effect and the result from

our theory was found to agree well with the DSMC simulation of Chap. 2, as seen in Fig. 3.7(b). This validates the previous deduction. Thus, the disparity in the obtained tangential Knudsen stress between our theory and the DSMC simulation can be considered to be caused by the effect of induced gas flows. Let us check whether the same is true for all Knudsen numbers.

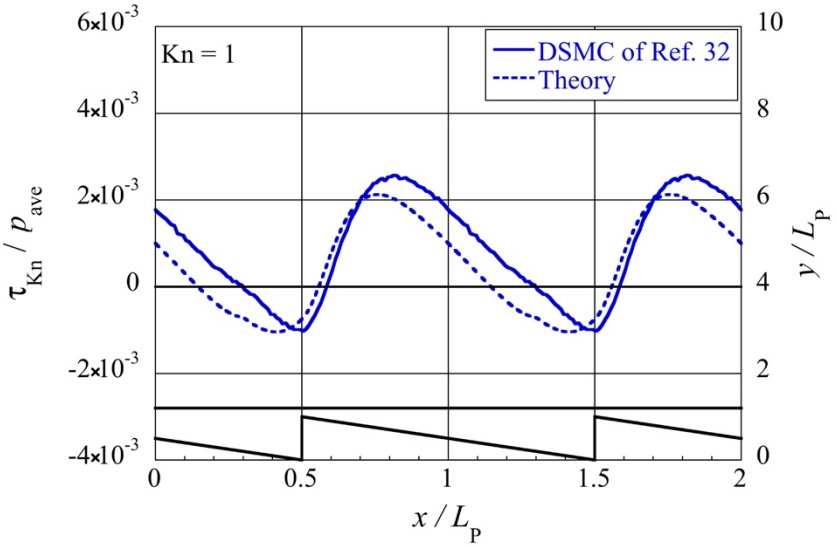

Fig. 3.5. Tangential Knudsen stresses obtained by DSMC simulation of Chap. 2 and that obtained by the theoretical analysis, at Kn = 1. Reprinted with permission from C. J. C. Otic and S. Yonemura, Physics of Fluids 34, 072010 (2022). Copyright 2022 Author(s).

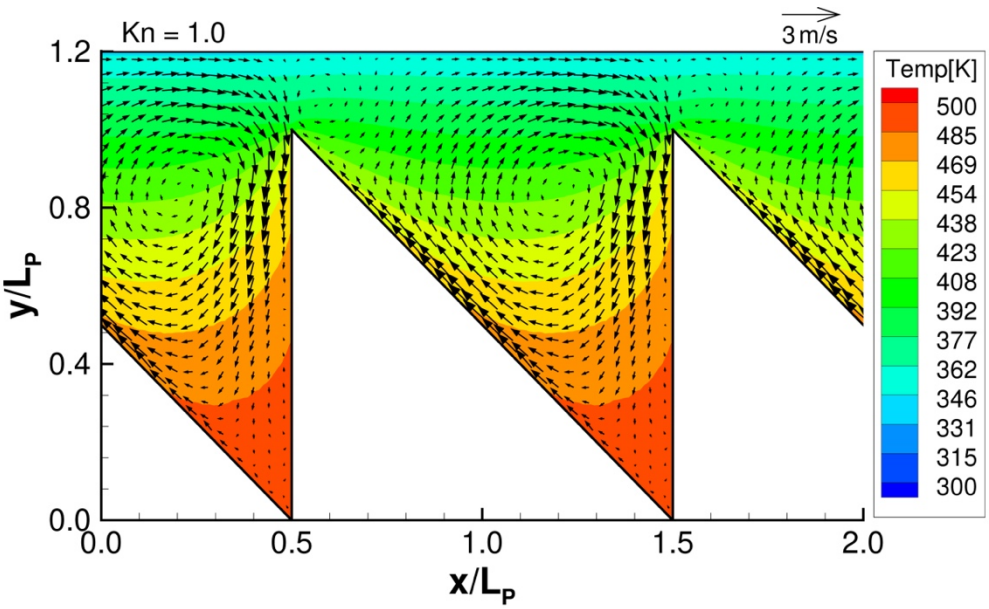

Fig. 3.6. DSMC result for the flow distribution and temperature distribution at Kn = 1. Reprinted with permission from C. J. C. Otic and S. Yonemura, Micromachines 13, 871 (2022). Copyright 2022 Author(s).

So far only the distribution of the local tangential Knudsen stress, i.e., the Knudsen force per unit area, has been shown. Next, let us consider the net tangential Knudsen force. For different Knudsen numbers, Fig. 3.8 shows the average tangential Knudsen stress obtained by the theoretical analysis, by viscous shear stress, and their sum, together with the results from the DSMC simulation of Chap. 2. Note that here, higher Knudsen number cases, i.e., $\mathrm{Kn} > 1$, are not included in the calculation of the estimated contribution of the flow. This is because the flow effect cannot be calculated based on Eq. (3.27) for $\mathrm{Kn} > 1$ since the region located λ_{ref} below the upper surface starts to be occupied by the ratchet body.

Let us consider the tangential Knudsen force starting from low Knudsen number cases. Figure 3.8 shows that in lower Knudsen numbers of $\mathrm{Kn} < 1$, there is a significant difference in the tangential Knudsen stress obtained by our theory and that obtained by DSMC simulation of Chap. 2. The results for theory and DSMC do not agree well particularly around $\mathrm{Kn} = 0.1$, where the net tangential Knudsen stress obtained in our theoretical analysis vanishes. This is because when $\mathrm{Kn} \to 0$, i.e., $\lambda \ll L$ thus $\exp(-L/\lambda) = 0$, $J_{\mathrm{M},x}^{(\mathrm{wall})}$ becomes zero from Eq. (3.17) and $J_{\mathrm{M},x}^{(\mathrm{gas})}$ also results in zero from Eq. (3.26). Here, the disappearance of $J_{\mathrm{M},x}^{(\mathrm{wall})}$ is natural because in the case of low Knudsen number, no molecule leaving the ratchet surface can arrive at the upper surface without experiencing intermolecular collisions. On the other hand, the disappearance of $J_{\mathrm{M},x}^{(\mathrm{gas})}$ is not true. The fact that the tangential stress appears in the DSMC simulation shows that this stress is caused by impinging molecules coming from the bulk region after experiencing intermolecular collisions in the case of low Knudsen number. This disparity shows the incompleteness of Eq. (3.26) for $J_{\mathrm{M},x}^{(\mathrm{gas})}$. The incompleteness might be because of the assumption that the gas is stationary. Figure 3.9 shows the resulting temperature and velocity distribution from the DSMC simulation of Chap. 2 for $\mathrm{Kn} = 0.1$. The strong thermal edge flow is generated near the tip of the ratchet. It must induce the tangential stress on the upper surface. Therefore, the contribution of flow has to be added as what was done for $\mathrm{Kn} = 1$. By taking the sum of the flow effect and our theory, the resulting value agrees very well with the tangential Knudsen stress obtained by DSMC simulation over the wide range of $\mathrm{Kn} \leq 1$, as seen in Fig. 3.8.

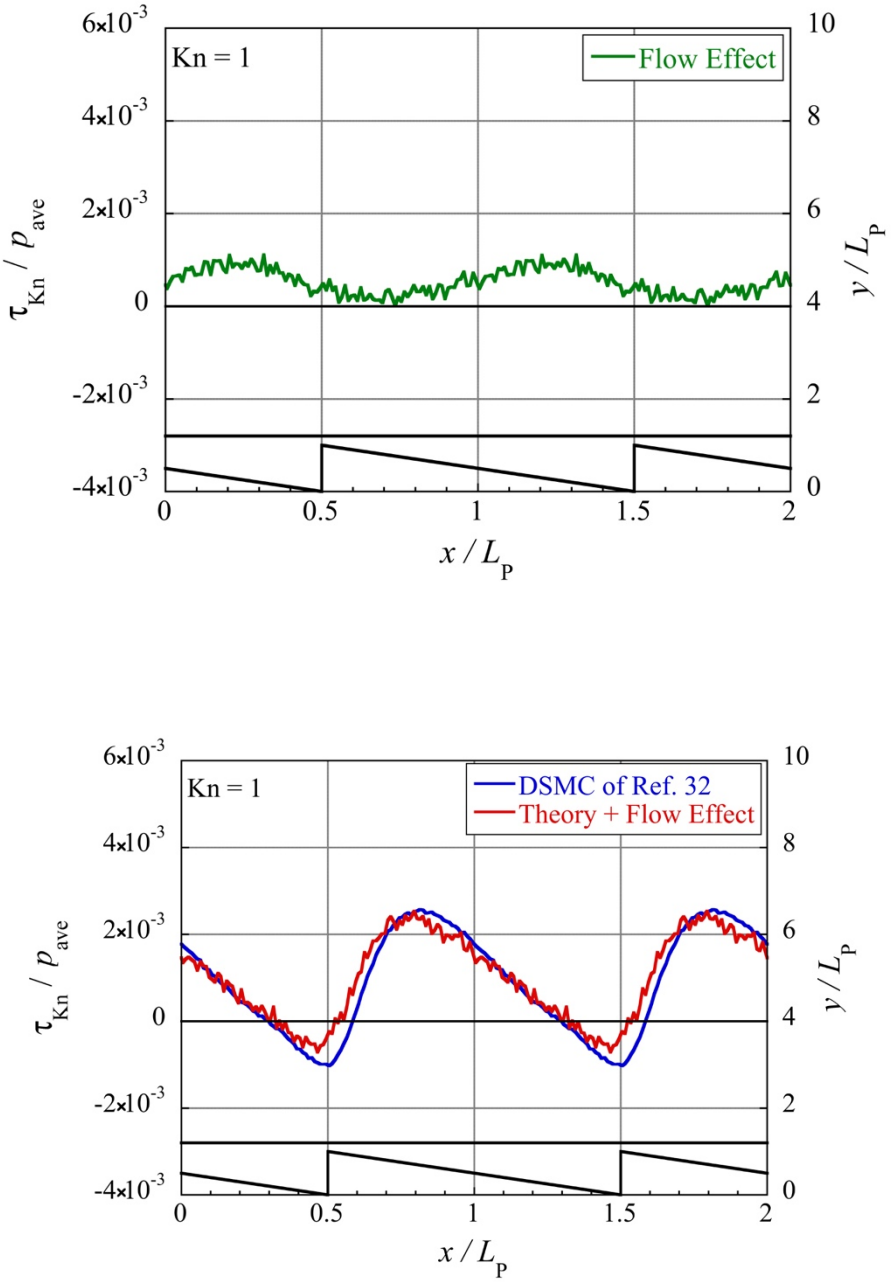

Fig. 3.7. (a) Estimated contribution of the flow to the tangential Knudsen stress, i.e., flow effect, and (b) tangential Knudsen stresses obtained by DSMC simulation of Chap. 2 and that obtained by the superposition of theoretical result and the contribution of the flow, at Kn = 1. Reprinted with permission from C. J. C. Otic and S. Yonemura, Physics of Fluids 34, 072010 (2022). Copyright 2022 Author(s).

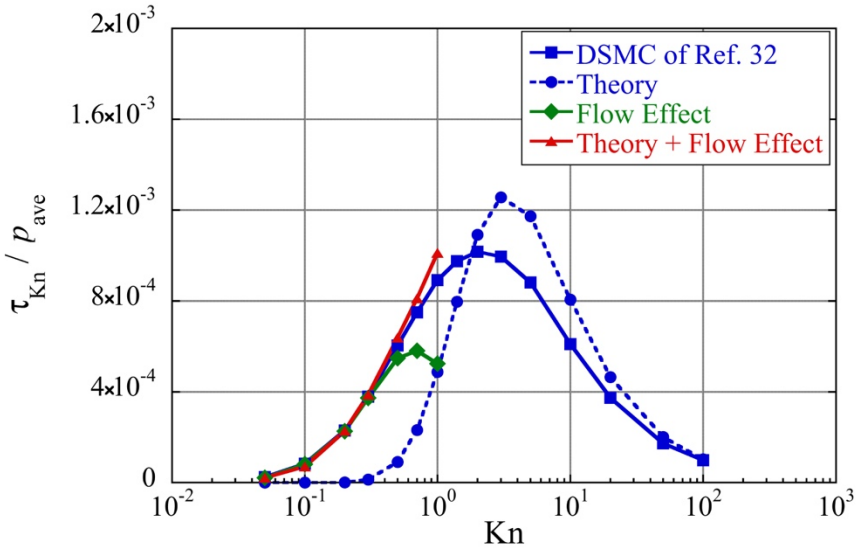

Fig. 3.8. Net tangential Knudsen stresses obtained by several methods, for the range of Knudsen numbers considered. Reprinted with permission from C. J. C. Otic and S. Yonemura, Physics of Fluids 34, 072010 (2022). Copyright 2022 Author(s).

Let us consider the cases of the Knudsen numbers higher than unity. In the case of $\mathrm{Kn} = 10$, the average tangential Knudsen stress obtained by our theory is higher than that obtained in the DSMC simulation, as shown in Fig. 3.8. Figure 3.10 shows the comparison of the distribution of the local tangential Knudsen stress obtained by our theoretical analysis and that by DSMC simulation for $\mathrm{Kn} = 10$. The theoretical evaluation is larger than the DSMC result over the region above the inclined part of the ratchet. On the other hand, Fig. 3.11 shows the resulting temperature and velocity distribution from the DSMC simulation for $\mathrm{Kn} = 10$. Although the flow field for $\mathrm{Kn} = 10$ becomes small compared with that for $\mathrm{Kn} = 1$, a rather strong flow along the inclined surface can be seen. In this case the mean free path λ_{ref} is larger than the maximum width of the channel, and hence, the flow effect could not be calculated by using Eq. (3.27). Since the flow along the inclined surface shown in Fig. 3.11 is located within the distance of λ_{ref} from the upper surface, it surely contributes to generating negative tangential stress on the upper surface. If this flow effect is considered, the disparity in the tangential Knudsen stress between the theoretical evaluation and the DSMC simulation will decrease.

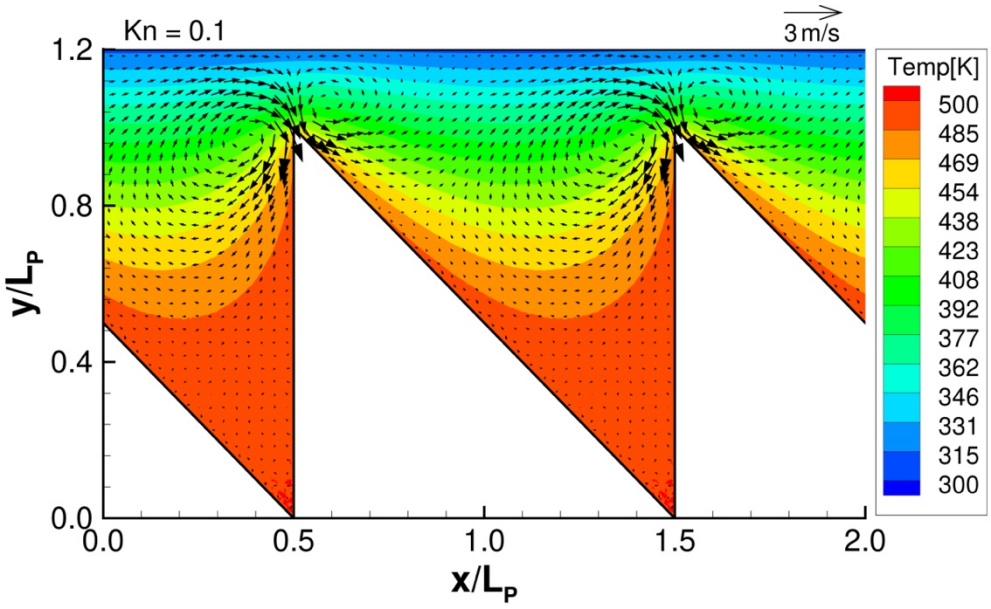

Fig. 3.9. DSMC result for the flow distribution and temperature distribution at Kn = 0.1. Reprinted with permission from C. J. C. Otic and S. Yonemura, Micromachines 13, 871 (2022). Copyright 2022 Author(s).

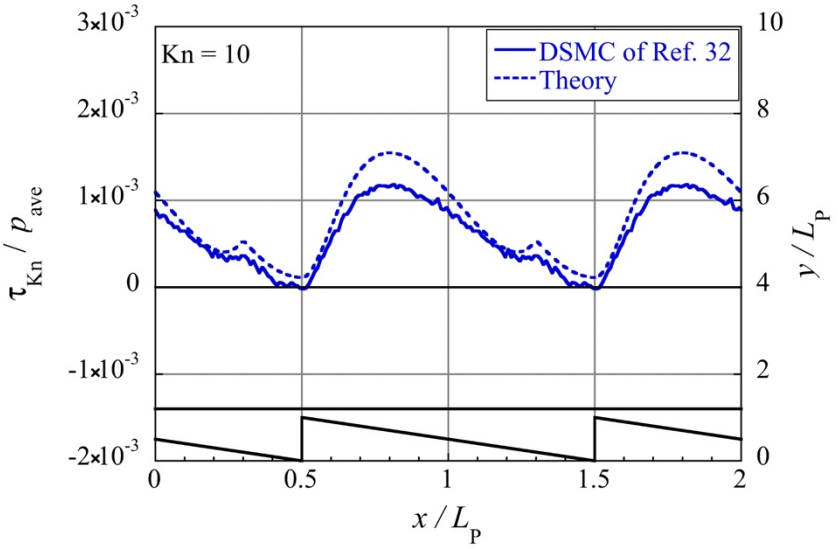

Fig. 3.10. Tangential Knudsen stresses obtained by DSMC simulation of Chap. 2 and that obtained by the theoretical analysis, at Kn = 10. Reprinted with permission from C. J. C. Otic and S. Yonemura, Physics of Fluids 34, 072010 (2022). Copyright 2022 Author(s).

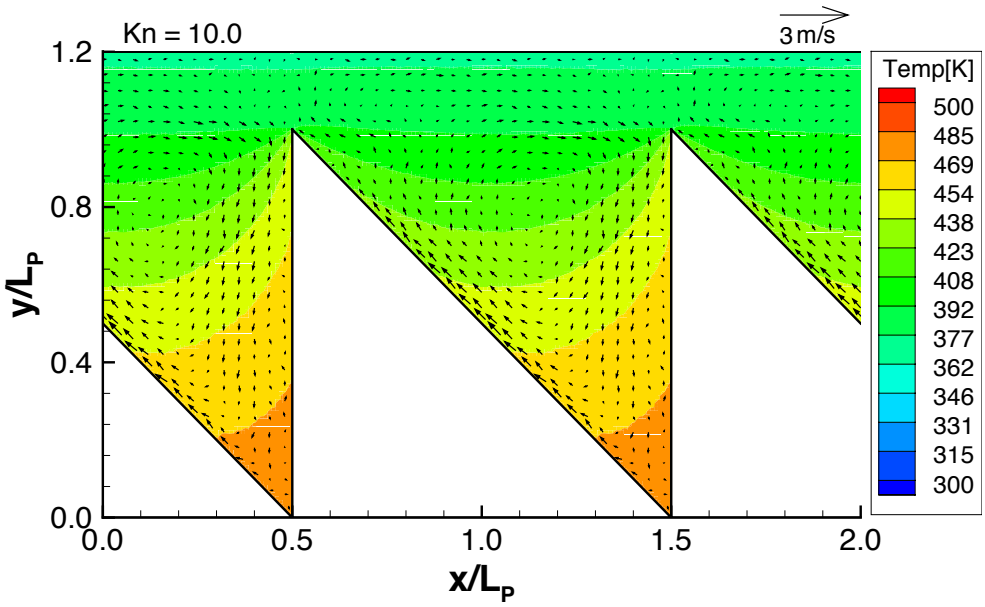

Fig. 3.11. DSMC result for the flow distribution and temperature distribution at Kn = 10. Reprinted with permission from C. J. C. Otic and S. Yonemura, Micromachines 13, 871 (2022). Copyright 2022 Author(s).

In the above discussion, the local tangential stress distribution in low Knudsen numbers of $\mathrm{Kn} < 1$ is not discussed. Before reaching a conclusion, it has to be investigated. Figure 3.12 shows the distribution of the local tangential Knudsen stress, i.e., the tangential Knudsen force per unit area, obtained by DSMC simulation, by theoretical analysis, and from the estimated contribution of the flow, at $\mathrm{Kn} = 0.1$. It can be seen that the local tangential Knudsen stress based on our theoretical analysis results in zero. The reason for this has been explained above. Note that although the average tangential Knudsen stresses obtained from DSMC simulation and due to the flow effect agree very well each other for the case of $\mathrm{Kn} = 0.1$, as shown in Fig. 3.8, the tangential Knudsen stress distributions for them do not agree each other. Therefore, there must be another force acting locally that needs to be considered.

In the case of low Knudsen numbers, i.e., $\mathrm{Kn} \leq 0.1$, it can be considered that the gas is in a slightly rarefied condition or near the equilibrium. For slightly rarefied gas conditions, in addition to the viscous shear stress, a thermal stress can also be induced[36–39]. Thermal stresses arise when the temperature gradient is non-uniform and is driven by gradients of heat flux. This condition introduces a momentum flux resulting in the thermal stress which can be expressed as follows:

$$\tau_{\mathrm{thermal}} = p_{\mathrm{ref}} \left(\frac{n_{\mathrm{ref}}}{n} \frac{{\lambda_{\mathrm{ref}}}^2}{T_{\mathrm{ref}}} \right) \left(\gamma_3 \frac{\partial^2 T}{\partial x \partial y} + \gamma_7 \frac{1}{T} \frac{\partial T}{\partial x} \frac{\partial T}{\partial y} \right), \tag{3.28}$$

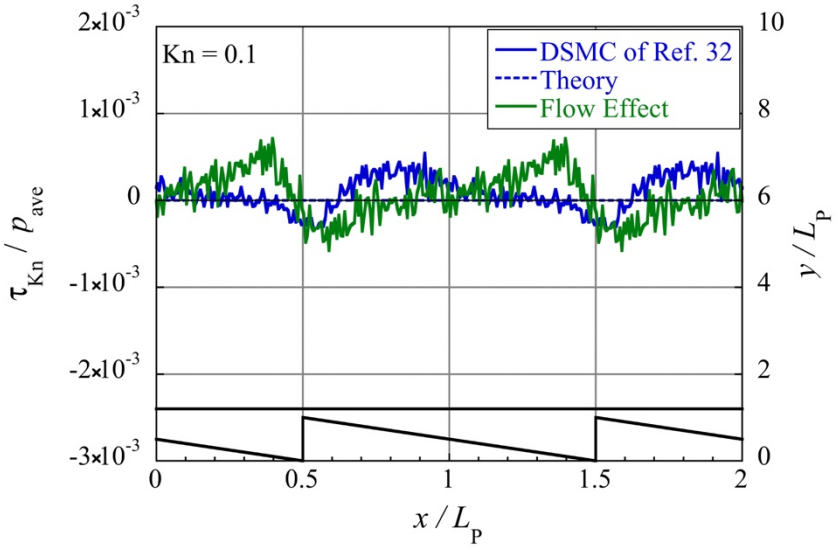

Fig. 3.12. Tangential Knudsen stresses obtained by DSMC simulation of Chap. 2, by theoretical results, and from the estimated contribution of the flow, at Kn $= 0.1$. Reprinted with permission from C. J. C. Otic and S. Yonemura, Physics of Fluids 34, 072010 (2022). Copyright 2022 Author(s).

where the variables with subscript "ref" are the reference values defined in Sec. 3, and the constants γ_3 and γ_7 are the thermal-stress transport coefficients which for hard sphere molecules have a value of $\gamma_3 = 1.947906335$ and $\gamma_7 = 0.188106$, respectively[37]. Here, the temperature at the gas region λ_{ref} below the upper surface is chosen for the calculation of the thermal stress. In Fig. 3.13, the distribution of the thermal stress is compared with the tangential stress obtained in the DSMC simulation minus the stress due to the flow effect. Here, the stress due to the flow effect is the one shown in Fig. 3.12. It shows the following interesting relation:

$$\{\text{The tangential Knudsen stress obtained in the DSMC simulation}\} - \{\text{Stress due to the flow}\} = \{\text{Thermal stress}\}. \tag{3.29}$$

Here, since the periodic boundaries are assumed in the x-direction in the present study, the gradient $\partial T/\partial y$ at $x = L_{\mathrm{P}}$ and $x = 0$ are equal, and hence, the γ_3 term in Eq. (3.28) vanishes when integrated with respect to x to obtain the net force. Furthermore, the γ_7 term in Eq. (3.28) was found to be very small, about two orders of magnitude smaller than the γ_3 term, and therefore can be neglected. For these reasons, the net value of the thermal stress is zero and does not contribute to the net tangential Knudsen stress for the considered situation. Thus, the phenomenon that although the net tangential Knudsen forces obtained from DSMC simulation

and due to the flow effect are coincident, the detailed stress distributions for them disagree is caused by the contribution of thermal stress, whose local distribution is not zero but net contribution is zero. Equation (3.29) can be rewritten as follows:

$$\{\text{The tangential Knudsen stress obtained in the DSMC simulation}\} = \{\text{Stress due to the flow}\} + \{\text{Thermal stress}\}. \quad (3.30)$$

Thus, for low Knudsen numbers, the tangential Knudsen stress can be given by the sum of contributions of the viscous effect and the thermal stress. From our simulations, it was found that the thermal stress becomes smaller as the Knudsen number increases. Therefore, considering the result obtained for Kn ≤ 1, it can be concluded that the tangential Knudsen stress can be given by our theoretical expression together with the viscous effect and the thermal stress as follows:

$$\{\text{The tangential Knudsen stress obtained in the DSMC simulation}\} = \{J_{\mathrm{M},x}^{(\mathrm{wall})}\} + \{J_{\mathrm{M},x}^{(\mathrm{gas})}\} + \{\text{Stress due to the flow}\} + \{\text{Thermal stress}\}. \quad (3.31)$$

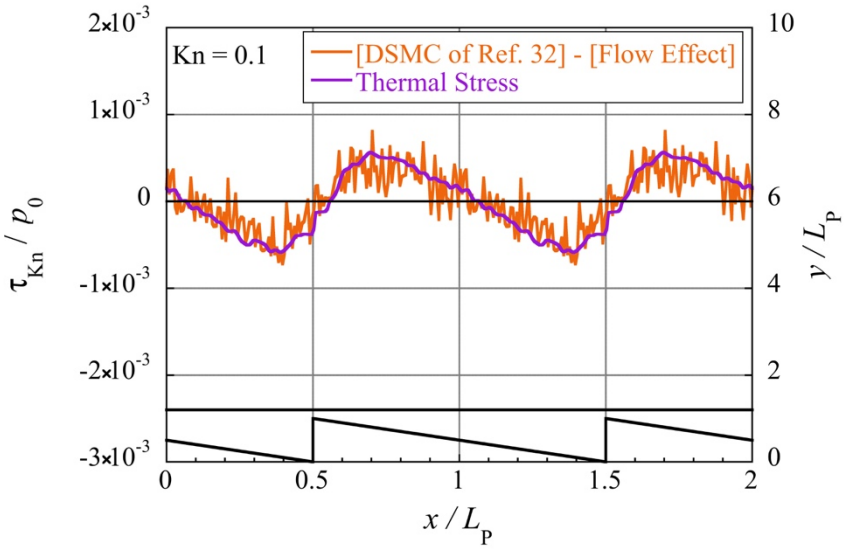

Fig. 3.13. Distribution of the thermal stress and that of the tangential Knudsen stress obtained by subtracting the flow effect from the DSMC results of Chap. 2, at Kn = 0.1. Here, p_{ref} is used as p_0 for the thermal stress, while the spatially averaged pressure p_{ave} is used as p_0 for the DSMC simulation and flow effect. Reprinted with permission from C. J. C. Otic and S. Yonemura, Physics of Fluids 34, 072010 (2022). Copyright 2022 Author(s).

3.5 Conclusion

A theoretical analysis was conducted to clarify the mechanism of the tangential Knudsen force for fully diffusive surfaces and for different Knudsen numbers. Considering two surfaces, an upper and a lower surface, a theoretical expression was derived by formulating the two kinds of x-momentum fluxes transferred on the upper surface, one is brought by molecules directly coming from the other surface without experiencing intermolecular collisions and the other is brought by molecules coming from the bulk region after experiencing intermolecular collisions there.

Using the combination of the hot ratchet structure and the cold object, the tangential Knudsen force on the object obtained by theoretical analysis in the present study was compared with that obtained in the numerical experiments by the DSMC method of Chap. 2. Although the tangential Knudsen force evaluated by our theoretical expression shows rather good agreement with that obtained in the numerical experiments, there is disparity between them. The most probable cause of this disparity is because in the derivation of the theoretical expression, the gas was assumed to be stationary although thermally driven flows can be induced. Hence, the theoretical expression together with the contribution of viscous flow gives the net tangential Knudsen force, which agrees with that obtained in the numerical experiments for $\mathrm{Kn} \leq 1$. Furthermore, from the investigation of thermal stress, it can be said, that the superposition of the evaluation by the theoretical expression, the contribution of viscous flow and the thermal stress will give not only the net tangential Knudsen force but also the detailed stress distribution, both of which agree with those obtained in the numerical experiments for $\mathrm{Kn} \leq 1$.

From the agreement of the obtained tangential Knudsen forces between the theoretical analysis and the numerical experiment, it is found that the tangential Knudsen force is caused by three mechanisms. The first is the contribution of impinging molecules coming from the other surface with different temperature. The second is the contribution of viscous effect of thermally driven flows. The third is the contribution of thermal stress, which is remarkable for small Knudsen numbers.

References

[1] W. Crookes, "Experimental contributions to the theory of the radiometer.—Preliminary notice," *Proceedings of the Royal Society A* 25, 303-314 (1877).

[2] O. Reynolds, "On the forces caused by the communication of heat between a surface and a gas; and on a new photometer," *Philosophical Transactions of the Royal Society A* 166, 725 (1876).

[3] A. Einstein, "Zur Theorie der Radiometerkräfte", *Zeitschrift für Physik* 27, 1–6 (1924).

[4] N. Selden, C. Ngalande, S. Gimelshein, E. P. Muntz, A. Alexeenko, and A. Ketsdever, "Area and edge effects in radiometric forces," *Physical Review E* 79, 041201 (2009).

[5] A. Ketsdever, N. Gimelshein, S.Gimelshein, and N. Selden, "Radiometric phenomena: From the 19th to the 21st century," *Vacuum* 86, 1644–1662 (2012).

[6] P. Epstein, "On the Resistance Experienced by Spheres in their Motion through Gases," *Physical Review* 23, 710 (1924).

[7] W. Phillips, "Thermal Force on Spherical Particles in a Rarefied Gas," *Physics of Fluids* 15, 999 (1972).

[8] A. Passian, A. Wig, F. Meriaudeau, T. L. Ferrel, and T. Thundat, "Knudsen forces on microcantilevers," *Journal of Applied Physics* 92, 6326 (2002).

[9] A. Passian, R. J. Warmack, T. L. Ferrell, and T. Thundat, "Thermal Transpiration at the Microscale: A Crookes Cantilever," *Physical Review Letters* 90, 124503 (2003).

[10] B. Gotsmann and U. Dürig, "Experimental observation of attractive and repulsive thermal forces on microcantilevers," *Applied Physics Letters* 87, 194102 (2005).

[11] M. Scandurra, F. Izacopetti, and P. Colona, "Gas kinetic forces on thin plates in the presence of thermal gradients," *Physical Review E* 75, 026308 (2007).

[12] T. Zhu and W. Ye, "Origins of Knudsen forces on heated microbeams," *Physical Review E* 82, 036308 (2010).

[13] J. Nabeth, S.Chigullapalli, and A. Alexeenko, “Quantifying the Knudsen force on heated microbeams: A compact model and direct comparison with measurements,” *Physical Review E* 83, 066306 (2011).

[14] A. Strongrich, W. O’Neill, A. Cofer, and A. Alexeenko,, “Experimental measurements and numerical simulations of the Knudsen force on a non-uniformly heated beam,” *Vaccuum* 109, 405–416 (2014).

[15] A. Strongrich, and A. Alexeenko, "Microstructure actuation and gas sensing by the Knudsen thermal force," *Applied Physics Letters* 107, 193508 (2015).

[16] Y. Sone and K. Aoki, “A similarity solution of the linearized Boltzmann equation with application to thermophoresis of a spherical particle,” *Journal of Theoretical and Applied Mechanics* 2, 3 (1983).

[17] A. Donkov, S. Tiwari, T. Liang, S. Hardt, A. Klar, and W. Ye, “Momentum and mass fluxes in a gas confined between periodically structured surfaces at different temperatures,” *Physical Review E* 84, 016304 (2011).

[18] A. Lotfian and E. Roohi, “Radiometric flow in periodically patterned channels: Fluid physics and improved configurations,” *Journal of Fluid Mechanics* 860, 544-576 (2019).

[19] M. Mousivand, and E. Roohi, "On the nonlinear thermal stress, thermal creep, and thermal edge flows in triangular cavities," *Physics of Fluids* 34, 052002 (2022).

[20] H. Brenner, “Nonisothermal Brownian motion: Thermophoresis as the macroscopic manifestation of thermally biased molecular motion,” *Physical Review E* 72, 061201 (2005).

[21] D. Zeng, R. Cai, Y.Yang, “DSMC study of the radiometric force acting on a thin plate with surface temperatures much higher than the environment temperature,” *International Journal of Mechanical Sciences* 187, 105922 (2020).

[22] D. Kalempa, and F. Sharipov, "Radiometric force on a sphere in a rarefied gas based on the Cercignani–Lampis model of gas–surface interaction," *Physics of Fluids* 33, 073602 (2021).

[23] K. Zhang, L. Xu, Y. Li, F. Marchesoni, J. Wang, and G. Xia, "Self-propulsion of Janus particles in the free molecular regime," *Physics of Fluids* 34, 033311 (2022).

[24] P. K. Roy, I. Legchenkova, L. Dombrovsky, V. Y. Levashov, B. Binks, N. Shvalb, S. Shoval, V. Valtsifer, E. Bormashenko, “Thermophoretic levitation of solid particles at atmospheric pressure,” *Advanced Powder Technology* 33, 103497 (2022).

[25] X. Wang, Z. Zhang, F. Han, W. Zhang, S. Zhang, “Ab initio simulation of rarefied flows of gaseous mixtures in the system of microbeams with different temperatures,” *International Communications in Heat and Mass Transfer* 131, 105872 (2022).

[26] A. Würger, "Leidenfrost Gas Ratchets Driven by Thermal Creep," *Physical Review Letters* 107, 164502 (2011).

[27] S. Hardt, S.Tiwari, and T. Baier, "Thermally driven flows between a Leidenfrost solid and a ratchet surface," *Physical Review E* 87, 063015 (2013).

[28] T. Baier, J. Dölger, and S.Hardt, “Energy harvesting through gas dynamics in the free molecular flow regime between structured surfaces at different temperatures,” *Physical Review E* 89, 053003 (2014).

[29] V. Shahabi, T. Baier, E. Roohi, and S. Hardt, “Thermally induced gas flows in ratchet channels with diffuse and specular boundaries,” *Science Reports* 7, 41412 (2017).

[30] T. Baier, S. Hardt, V. Shahabi, and E. Roohi, “Knudsen pump inspired by Crookes radiometer with a specular wall,” *Physical Review Fluids* 2, 033401 (2017).

[31] L. Zhu and Z. Guo, "Numerical study of nonequilibrium gas flow in a microchannel with a ratchet surface," *Physical Review E* 95, 023113 (2017).

[32] C. J. Otic, and S. Yonemura, “Effect of Different Surface Microstructures in the Thermally Induced Self-Propulsion Phenomenon,” *Micromachines* 13, 871 (2022).

[33] D. Wadsworth and E. Muntz, “A computational study of radiometric phenomena for powering microactuators with unlimited displacements and large available forces,” *Journal of Microelectromechanical Systems* 5(1), 59-65 (1996).

[34] G. A. Bird, *Molecular Gas Dynamics and the Direct Simulation of Gas Flows* (Oxford University Press, Oxford, 1994).

[35] W.G. Vincenti and C. H. Kruger, *Introduction to Physical Gas Dynamics* (Krieger Publishing Company, Malabar, 1975).

[36] M. Kogan, V. Galkin, and O. Fridlender, “Stresses produced in gases by temperature and concentration inhomogeneities. New types of free convection,” *Soviet Physics Uspekhi* 19, 420–428 (1976).

[37] Y. Sone, “Flows induced by temperature fields in a rarefied gas and their ghost effect on the behavior of a gas in the continuum limit,” *Annual Review of Fluid Mechanics* 32, 779–811 (2000).

[38] Y. Sone, *Molecular Gas Dynamics: Theory, Techniques, and Applications* (Birkhauser Boston, 2007).

[39] A. Mohammadzadeh, A. S. Rana, and H. Struchtrup, “Thermal stress vs. thermal transpiration: A competition in thermally driven cavity flows,” *Physics of Fluids* 27, 112001 (2015).

Chapter 4 Numerical Investigation on Thermally Induced Forces Used for a Non-Contact Manipulation of a Micro-Object

4.1 Introduction

In rarefied gas conditions, such as that in micro/nano-scale flows, an object placed close to a structure of a different temperature and receives a force[1]. This phenomenon is caused by temperature inhomogeneities in the gas at conditions where the Knudsen number, defined as the ratio of the mean free path for gas molecules to the characteristic length of the flow, is non-zero[2]. The class of forces induced in this phenomenon is called as Knudsen force. Recent advances in micro-electromechanical systems (MEMS) made it possible to fabricate micro/nano-devices that can exploit the Knudsen forces for specific applications[1–10]. Such technologies include microstructure actuation[5–6], gas sensing[7–9], atomic force microscopy[1,4], and high-precision force measurements[3], among others. In addition to experimental[2,10] and theoretical approaches[1,11–13], numerical approaches have also been used to study the Knudsen forces[7,10,14–17]. Computational studies are particularly significant to reproduce the thermally induced flow field in complex systems that is difficult to observe experimentally. The studies of [1,2,10,15–18] started from a relatively simple configuration; specifically, a microbeam was placed close to a flat plate. For this configuration, Nabeth et al. [15] and Zhu and Ye[16] provided their explanations for the mechanism of the Knudsen force. Specifically, the latter pointed out that the Knudsen force is caused mainly by the thermally induced flows in the bulk region of the gas, and that the configuration of the physical domain has a significant influence on the magnitude and direction of the Knudsen force. Therefore, the configuration can be manipulated with a desired application in mind, such

---

Discussions are based mainly on C.J.C. Otic and S. Yonemura, "Thermally induced Knudsen forces for contactless manipulation of a micro-object," *Micromachines* 13, 1092 (2022).

as two beams of different temperatures placed close to each other to be used for gas sensor mechanism[5–7,9] and a heated object placed eccentrically inside a closed system to be used for rotational mechanism[12–13]. Furthermore, simple geometrical modifications in the actuator mechanism have shown better performance than conventional ones[19].

The above studies[1–19] proved that thermally induced Knudsen forces can displace an object without physical contact and any moving parts. This displacement is usually repulsive, such as a heated cantilever being deflected away from a colder flat substrate[1,2,8]. However, by reversing the temperature gradient, i.e., when a cold cantilever is placed close to a heated flat substrate, the direction of the generated force is reversed (attractive force)[4]. In this case, the thermally induced Knudsen force can displace the object closer to the substrate. Furthermore, if the substrate has a microstructure, the tangential Knudsen force will be induced on the object and can induce the self-propulsion of the object[11,14]. Combining these two ideas, it may be possible to use the thermally induced Knudsen forces to capture or manipulate an object without contact. Specifically, the usual configuration where a beam is placed close to a flat substrate can be modified to achieve a mechanism that can trap and manipulate a micro-object in a gas.

Contactless trapping and manipulating a micro-object suspended in a liquid has been extensively studied in microfluidics[20–33]. For example, optical trapping uses a laser beam as a tweezer-like mechanism, which can trap and directly manipulate micro-objects[20–22]. On the other hand, for objects that are sensitive to heat, such as biological cells, hydrodynamic trapping is another method where flow field is induced to trap and manipulate suspended micro-objects[23–26]. Alternatively, both mechanisms can also be employed together. For example, an optically trapped micro-rotor can induce highly localized flow fields that can be used to indirectly manipulate micro-objects[27]. Another example is the use of optical gradient and thermophoretic forces to trap targets to a focal spot[28–29]. However, these mechanisms have been limited to liquid conditions. Optical trapping of a micro-object is typically more complicated in gas than in water[30–31], while aerodynamic-based traps [32–33] have shown that artificially induced air flows can trap and manipulate objects similar to hydrodynamic traps. However, such systems use jets of air, and in those systems, high-precision manipulation of a micro-object is difficult to achieve.

In this study, we take advantage of the thermally induced Knudsen force appearing uniquely in micro/nano-scale flows to propose a simple configuration of a tweezer-like mechanism, which can be used to trap and manipulate a micro-object in a gas. Specifically, we demonstrate that when a thin plate is perpendicularly mounted on a heated substrate and placed close to a

colder beam (micro-object of interest), a force is generated on the beam and attracts the beam to the thin plate horizontally and vertically. Therefore, in this configuration, the thin plate acts like tweezers that can trap and manipulate the beam. Using the direct simulation Monte Carlo (DSMC) method, we reproduce the flow and study the Knudsen force induced on the beam. The effect of different parameters on the Knudsen force is also investigated in this paper

4.2 Methodology

Let us consider the space between two horizontal infinitely wide flat substrates, which are filled with air. In this study, the function of tweezers is represented by a thin plate mounted perpendicularly on the upper substrate facing downward, and below the thin plate is the object to be grasped which is represented by a beam suspended in air, as shown in Fig. 4.1.The two substrates and the thin plate are heated at a temperature $T_{\mathrm{sub}} = 500$ K, while the object, i.e., the beam, is set at a room temperature $T_{\mathrm{obj}} = 300$ K. Here, the width and the height of the beam are w and h, respectively, and its top surface is separated downward from the bottom surface of the flat upper substrate by a gap distance, g_{tot}, as shown in Fig. 4.1. Moreover, the thin plate is a protrusion of length l_{pro} from the substrate and is deviated rightward from the center of the beam by a distance of l_{dev}. Therefore, the gap distance between the tip of the thin plate and the top surface of the beam, g_{tip}, is given by $g_{\mathrm{tip}} = g_{\mathrm{tot}} - l_{\mathrm{pro}}$. Although the local flow field near the thin plate will be largely influenced by the size of the minimum gap g_{tip}, the global flow field around the object will be determined by the size of the gap distance between the beam and the flat upper substrate, g_{tot}. Therefore, in this study, the total gap distance, g_{tot}, is considered as the characteristic length of the flow, which is used to calculate the Knudsen number, as mentioned later.

Here, the x axis is set rightward and the y axis is set upward such that $x = 0$ is colinear with the center of the beam, and such that $y = 0$ is on the bottom surface of the upper substrate, i.e., the uppermost boundary. Furthermore, the computational domain is considered to be periodic in the $-x$ and $+x$ directions, and the bottommost boundary is considered to be a surface of the lower substrate. As shown in Figure 4.1, the distances between the left side of the computational domain and the left side of the beam and between the right side of the computational domain and the right side of the beam are both L_{side}. The distance between the bottom surface of the beam and the bottommost boundary is L_{bot}.

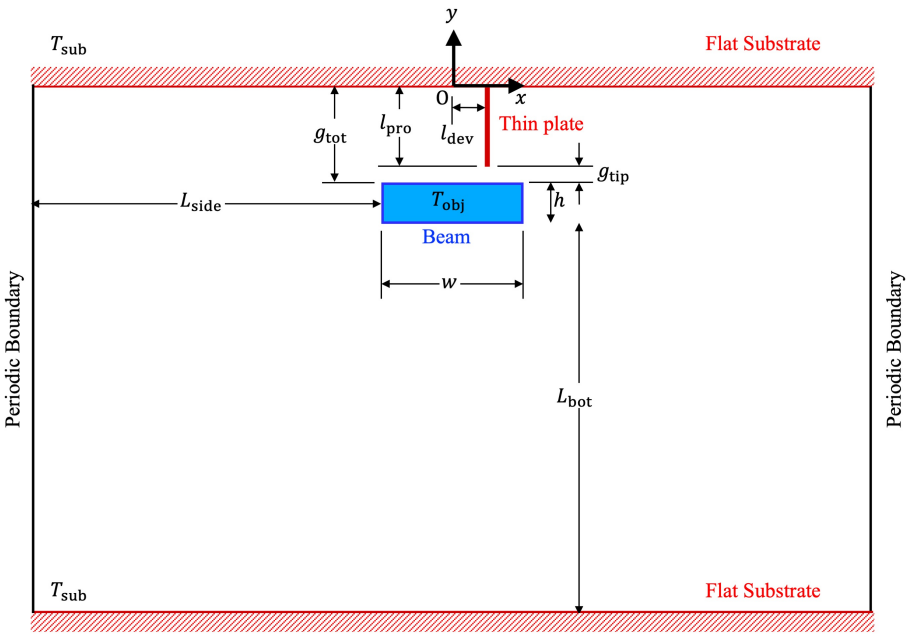

Fig. 4.1. Schematic of the computational domain. Reprinted with permission from C. J. C. Otic and S. Yonemura, Micromachines 13, 1092 (2022). Copyright 2022 Author(s).

In this study, air is used as the working gas. Although air is composed of molecules of different species, it is assumed here that air molecules are represented by imaginary hard sphere molecules[34] with a mass $m = 4.80967 \times 10^{-26}$ kg. Note that, as discussed in Chap. 2, by using hard sphere molecules of constant diameter instead of realistic air molecules, the discussion in this study can also be applied to other gases without being limited to air, provided that the Knudsen number is the same. From the reference temperature at $T_{\mathrm{ref}} = (T_{\mathrm{sub}} + T_{\mathrm{obj}})/2 = 400$ K, the equivalent viscosity is $\mu_{\mathrm{ref}} = 2.301328\cdots \times 10^{-5}$ Pa · s[35–36]. From the relation $\mu_{\mathrm{ref}} = 0.499 m n_{\mathrm{ref}} \bar{C}_{\mathrm{ref}} \lambda_{\mathrm{ref}}$ and the mean free path for gas molecules given by $\lambda_{\mathrm{ref}} = 1/\sqrt{2} n_{\mathrm{ref}} \pi d_{\mathrm{m}}^2$, the diameter of the imaginary hard sphere molecules is obtained and set at $d_{\mathrm{m}} = 0.356$ nm, where $\bar{C}_{\mathrm{ref}}$ is the average thermal speed of molecules and given by $\bar{C}_{\mathrm{ref}} = \sqrt{8 k_{\mathrm{B}} T_{\mathrm{ref}}/\pi m}$, k_{B} is the Boltzmann constant given by $k_{\mathrm{B}} = 1.380649 \times 10^{-23}$ J/K, and n_{ref} is the number density of molecules at the reference temperature T_{ref} and the reference pressure p_{ref} and given by $n_{\mathrm{ref}} = p_{\mathrm{ref}}/k_{\mathrm{B}} T_{\mathrm{ref}}$, and the reference pressure p_{ref} is set at the standard pressure $p_{\mathrm{ref}} = 1$ atm. Using the above relation, for $d_{\mathrm{m}} = 0.356$ nm, the corresponding mean free path is $\lambda_{\mathrm{ref}} = 96.79697\cdots$ nm, and the mean free time, $\tau_{\mathrm{ref}} = \lambda_{\mathrm{ref}}/\bar{C}_{\mathrm{ref}}$, is $\tau_{\mathrm{ref}} = 1.790101\cdots \times 10^{-10}$ s. As mentioned above, in this study, the length g_{tot} is considered as the characteristic length, such that the Knudsen number, $\mathrm{Kn} = \lambda_{\mathrm{ref}}/g_{\mathrm{tot}}$. Furthermore, the reference lengths for the computational domain shown in Fig. 4.1 are set

relative to the reference mean free path λ_{ref}, as tabulated in Table 4.1. Note that here, the Knudsen number is set at $\mathrm{Kn} = 0.2$, i.e., the length g_{tot} is set at $5\lambda_{\mathrm{ref}}$.

Table 4.1. Reference lengths for the physical domain.

Parameter	**Symbol**	**Value**
Beam width	w	$8\lambda_{\mathrm{ref}}$
Beam height	h	$2\lambda_{\mathrm{ref}}$
Length of protrusion	l_{pro}	$4\lambda_{\mathrm{ref}}$
Tip to beam distance	g_{tip}	λ_{ref}
Total gap	g_{tot}	$5\lambda_{\mathrm{ref}}$
Deviation of plate from center	l_{dev}	$2\lambda_{\mathrm{ref}}$
Distance of side boundaries	L_{side}	$20\lambda_{\mathrm{ref}}$
Distance of bottommost boundary	L_{bot}	$20\lambda_{\mathrm{ref}}$

In this study, the focus is on non-continuum flow conditions, i.e., micro/nano-scale flows and, hence, the Navier–Stokes equation is not applicable. Here, the direct simulation Monte Carlo (DSMC) method[37–38] was used to simulate the flow. The DSMC method has already been used in several studies for the Knudsen forces on microbeams[7,16–17]. In the DSMC method, the motion of sample molecules, which are considered as a statistical representation of the real molecules, is simulated and tracked. Since the Knudsen force in a steady state is of interest in this study, macroscopic properties are then taken as the time average of the sampled molecular velocities. Free motions and intermolecular collisions are decoupled over a very small time step. In this study, the maximum collision number method[39–40] is used to treat intermolecular collisions. The details on the maximum collision number method used here were presented in Chap. 2. For simplicity, a surface accommodation coefficient of unity is assumed here, and the diffuse reflection model[34] is used for molecule–wall collisions. The DSMC method used in this study is described in the flow chart shown in Fig. 4.2.

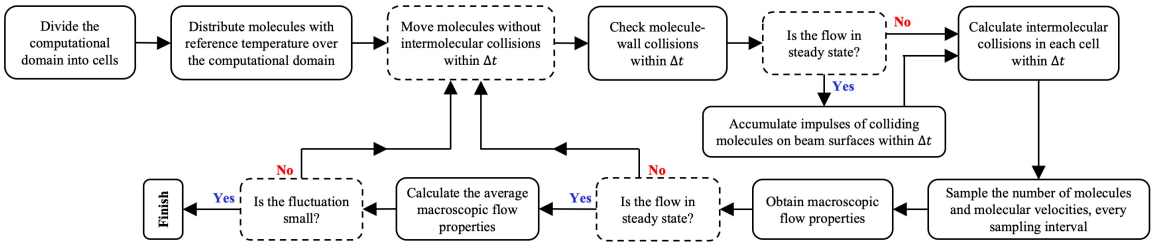

Fig. 4.2. Flow chart of the DSMC method used in this study. Reprinted with permission from C. J. C. Otic and S. Yonemura, Micromachines 13, 1092 (2022). Copyright 2022 Author(s).

The physical domain in Fig. 4.1 was divided into DSMC cells with uniform cell sizes Δx and Δy set smaller than the mean free path λ_{ref}. For all the cases considered in this study, a cell size of $\Delta x = \Delta y = \lambda_{\mathrm{ref}}/4$ is used. Furthermore, the time step for the DSMC simulation was also set smaller than the mean free time τ_{ref}. For all the cases considered in this study, a time step of $\Delta t = 0.08\tau_{\mathrm{ref}}$ is used. This chosen time step ensures that not only is it smaller than the mean free time, but also, no molecule can cross two cells within one time step. Moreover, sample molecules were initialized in each DSMC cell at a number of 30 for the standard cell size of $\Delta x \times \Delta y$. The macroscopic flow properties are obtained by sampling the molecular velocities. The details on the calculation of the macroscopic properties, such as the number density n, the flow velocity v, and temperature T, in each DSMC cell, were presented in Chap. 2. Of particular interest in this study is the force acting over the surfaces of the beam. The local surface force, $F_{i,l}$, per unit area is given by:

$$\frac{F_{i,l}}{\Delta S_l} = \frac{W_{\mathrm{f}}}{\Delta S_l (t_{\mathrm{end}} - t_{\mathrm{start}})} \sum_{q=1}^{N_{\mathrm{wall-coll},l}} m \left[(\boldsymbol{c}_q)_i - (\boldsymbol{c}_q)_i' \right]. \tag{4.1}$$

Here, W_{f} is the number of real molecules represented by one sample molecule and $F_{i,l}$ is the ith component of the surface force exerted on the lth surface element with a width ΔS_l of the surface of the beam. In the present study, two dimensional flow field is considered. Nevertheless, it means not that the thickness of the flow field is zero but that the flow field does not change in the z direction, which is normal to the xy plane. Thus, the thickness of the flow field in the z direction is regarded as unity. The same is true for the DSMC cell size. Using the volume of a DSMC cell with unit thickness, the factor W_{f} was obtained by dividing the expected number of real molecules within the DSMC cell in the initial state by the number of initial sample molecules. Thus, the width ΔS_l represents the area of the lth surface element. While $N_{\mathrm{wall-coll},l}$ is the number of sample molecules colliding onto the lth surface element during the

sampling term from $t = t_{\mathrm{start}}$ to $t = t_{\mathrm{end}}$, $\boldsymbol{c}_q$ and $\boldsymbol{c}'_q$ are the pre-collision and post-collision velocities of the qth sample molecule in terms of the order of wall–molecule collision occurring in the sampling term. The net force, F_i, is then obtained by integrating the local surface force per unit area $F_{i,l}/\Delta S_l$ in Eq. (4.1) over the surface of the object.

4.3 Results and discussion

4.3.1 Evaluation of the proposed device compared to the case of no thin plate

Let us first consider the case when there is no thin plate mounted on the substrate at the uppermost boundary. Figure 4.3 (a) and Fig. 4.3 (b) show the temperature and pressure distributions with the flow distribution obtained in the DSMC simulation for such a case, and Fig. 4.4 (a) shows the flow and pressure distributions near the beam for the same case. Note that the pressure is normalized by p_{ave}, which is the pressure spatially averaged in the whole region of the gas. In the present DSMC simulation, the gas pressure in the cell j is obtained by $p_j = n_j k_{\mathrm{B}} T_j$, where T_j is the temperature of gas in the cell j, n_j is the number density of gas molecules in the cell j and given by $n_j = N_j/V_j$, N_j is the number of real molecules in the cell j, and V_j is the volume of the cell j. Here, the spatially averaged pressure p_{ave} is defined as $p_{\mathrm{ave}} = \left(\sum_j V_j p_j\right)/\left(\sum_j V_j\right)$, where $\sum_j$ represents the summation over all the DSMC cells. Since the spatially averaged number density and the spatially averaged temperature are defined as $n_{\mathrm{ave}} = \left(\sum_j N_j\right)/\left(\sum_j V_j\right)$ and $T_{\mathrm{ave}} = \left(\sum_j N_j T_j\right)/\left(\sum_j N_j\right)$, respectively, the relation $p_{\mathrm{ave}} = n_{\mathrm{ave}} k_{\mathrm{B}} T_{\mathrm{ave}}$ is satisfied. In the present simulations, the spatially averaged number density will not differ from the initial value, i.e., the setting value, because the number of real molecules will not vary during the simulations and, hence, n_{ave} is constant and common for all the considered cases. Therefore, the spatially averaged pressure p_{ave} is proportional to the spatially averaged temperature T_{ave}. On the other hand, the spatially averaged temperature T_{ave} is determined as a result of DSMC simulation and depends on the ratio of the area of hot surface to the area of the cold surface. Since this ratio depends on the cases, the resultant spatially averaged temperature varies depending on the cases. Due to the variation in T_{ave}, the spatially averaged pressure p_{ave} also varies depending on the cases. Under the condition where the surrounding pressures are different among the cases, the pressure and the stress cannot be properly compared among the cases by using their absolute values. In order to avoid this prob-

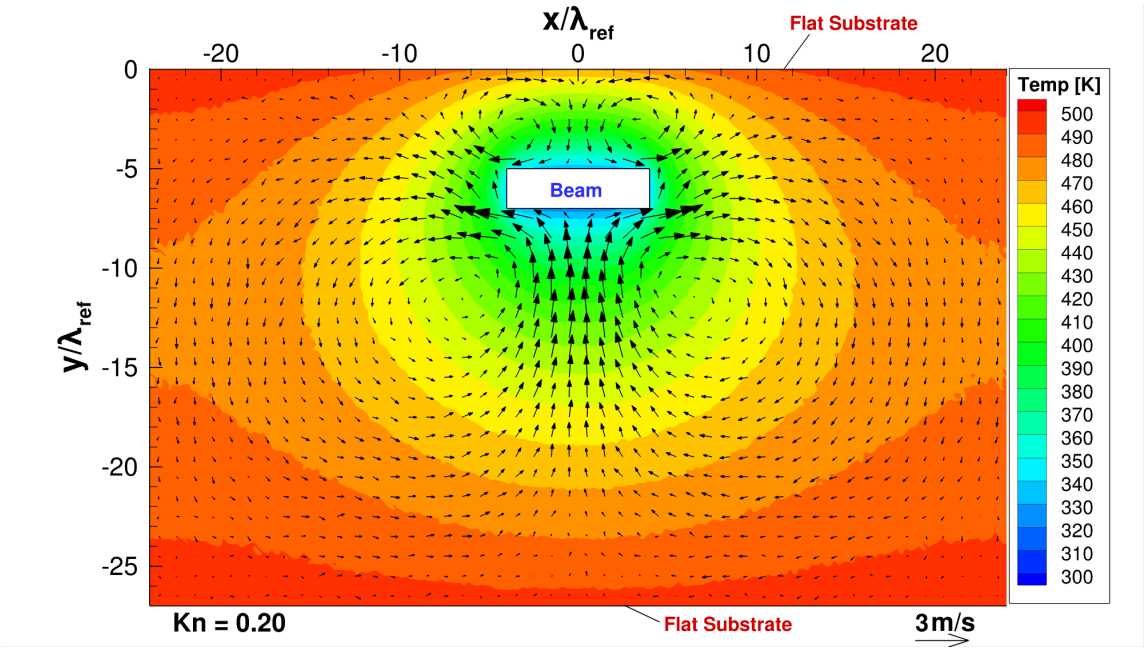

(a)

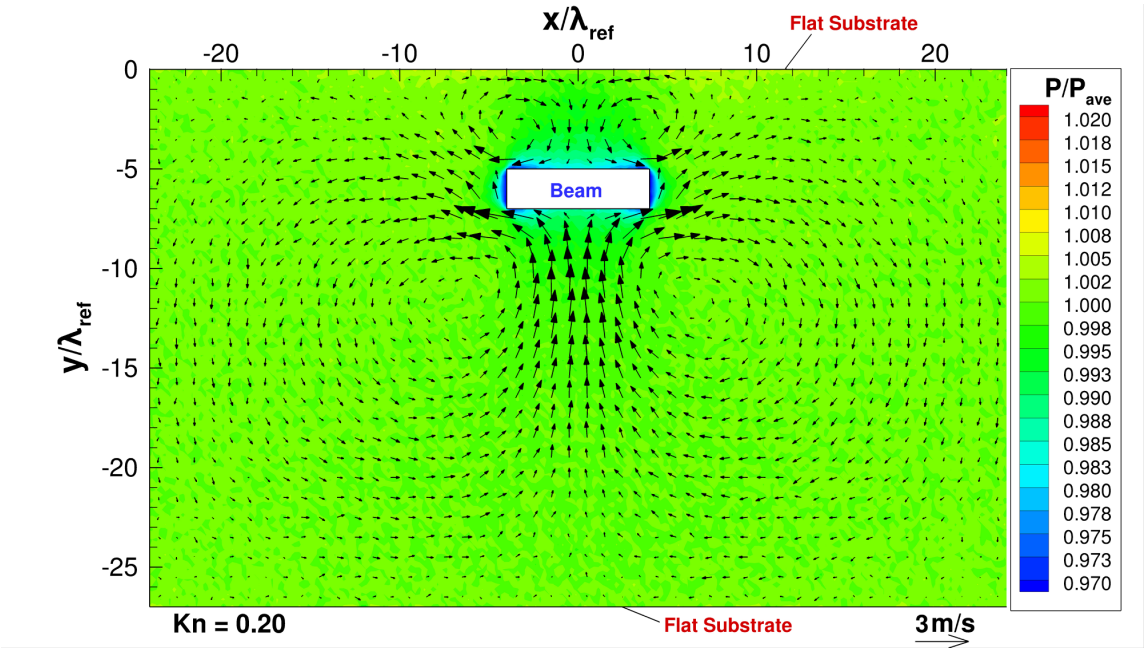

(b)

Fig. 4.3. (a) Flow and temperature distribution and (b) pressure distribution, when the beam is placed close to a heated flat substrate, at Kn = 0.2. Reprinted with permission from C. J. C. Otic and S. Yonemura, Micromachines 13, 1092 (2022). Copyright 2022 Author(s).

lem, in the present study, the pressure and the stress normalized by the spatially averaged pressure p_{ave} are compared instead of their absolute values.

According to Sone, Y[41], in the case when an object of uniform temperature with sharp edges is immersed in a gas with a different temperature, the temperature field induced around the edges of the object drives a flow from a colder region to a hotter region near the edges. This flow is called thermal edge flow. The thermal edge flow should be considered as a pumping mechanism rather than a usual flow. For example, the driving mechanism of a pump using a thermal edge flow was proposed[42]. In the present study, the thermal edge flows are induced near the beam corners in the directions from the central region of each surface of the beam to the corners. Since the thermal edge flows play a role as pump, these flows move gas molecules away from the corners. As a result, low pressure is induced around the beam, as shown in Fig. 4.3 (b). The low-pressure area on the bottom surface of the beam, which is induced by the thermal edge flow, sucks in gas from the wide bulk region of the gas below the beam due to the induced pressure difference; thus, the strong upward flow from the bulk to the beam is induced. This upward-pressure-driven flow supplies molecules to the low-pressure area on the bottom surface of the beam. In other words, this pressure-driven flow compensates the decrease in molecules in the central region of the bottom surface of the beam in such a manner that the supply of molecules is balanced with the removal of molecules due to the thermal edge flows in the steady state. Due to this compensation of the decrease in molecules by the upward-pressure-driven flow, the low pressure induced by the thermal edge flow is partly cancelled out, but remains in the central region of the bottom surface of the beam in the steady state, as shown in Fig. 4.3 (b) and Fig. 4.4 (a). This is because if the low pressure is fully canceled out, the pressure-driven flow will disappear, and the thermal edge flow will pump out molecules from the considered region again and, hence, the flow cannot become steady.

The same is true for the low-pressure area on the top surface of the beam. The low-pressure region on the top surface of the beam sucks in gas from the narrow region of the gas above the beam. Thus, the downward-pressure-driven flow from the narrow region to the beam is induced. However, this downward flow to the top surface of the beam is much weaker than the upward flow to the bottom surface of the beam. The reason for the weaker downward flow is because the low-pressure area on the top surface can gather only a fewer number of molecules because of a smaller space between the beam and the upper substrate compared with the low-pressure area on the bottom surface. The decrease in the number of molecules near the bottom surface is more efficiently compensated by the strong upward molecular flow than that near the top surface. This causes relatively high pressure on the bottom surface compared with that on the

top surface, as shown in Fig. 4.3 (b) and Fig. 4.4 (a). This pressure difference can be seen in the stress distribution exerted on the beam surface shown in Fig. 4.4 (b).

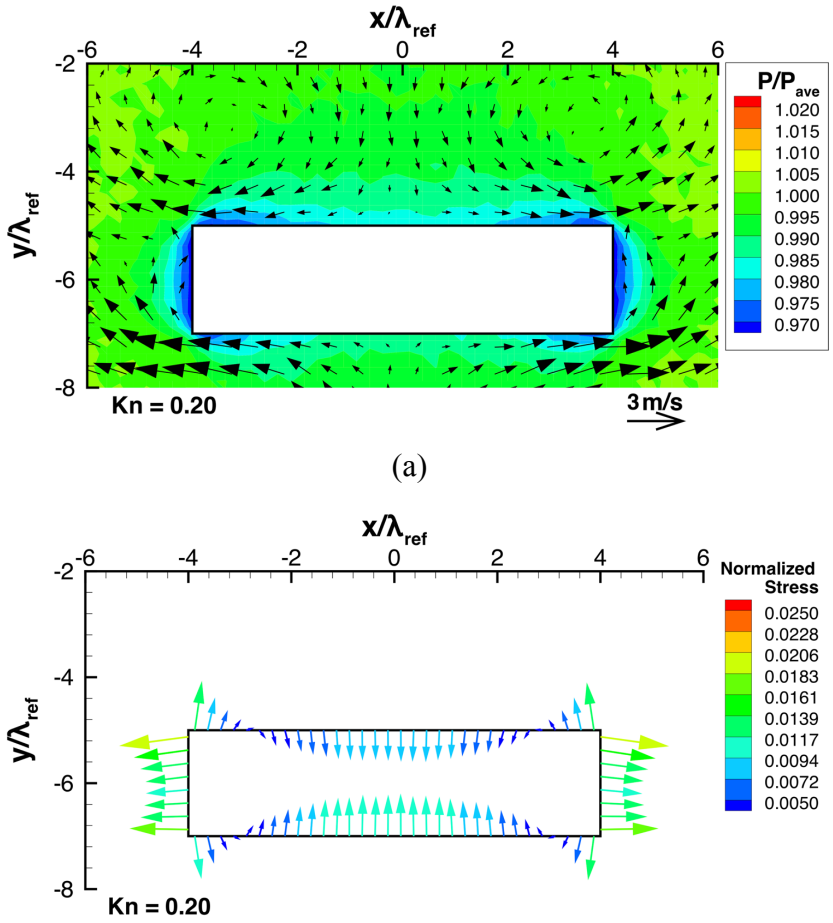

Fig. 4.4. (a) Pressure and flow distributions around the beam, and (b) stress distributions on the beam surfaces, when the beam is placed close to a heated flat substrate, at Kn = 0.2. Reprinted with permission from C. J. C. Otic and S. Yonemura, Micromachines 13, 1092 (2022). Copyright 2022 Author(s).

After the upward-pressure-driven flow impinges on the bottom surface of the beam, it is directed sideways. As a result, it forms two vortices of opposite rotation, such that it satisfies the equation of continuity. However, the formation of two vortices seen here can be considered to be caused by the limited region of the computational domain in the present study. If the domain is large enough, i.e., if the lower substrate and the periodic boundaries on the right and left sides are far enough from the beam, it can result in just a jet of gas impinging on a plate,

which is converted into two opposing flows along the plate. In the same manner, two opposing vortices are induced also near the top surface of the beam, although they are much weaker than those appearing near the bottom surface. This is because the downward-pressure-driven flow to the top surface of the beam is much weaker than the upward-pressure-driven flow to the bottom surface of the beam, as mentioned above.

Let us now consider the case when a thin plate is mounted on a flat substrate. Figure 4.5 (a) and Fig. 4.5 (b) show the temperature and pressure distributions with the flow distribution obtained from DSMC for such a case, and Fig. 4.6 (a) shows the flow and pressure distributions near the beam for the same case. In this case, except the region near the right side of the top surface of the beam, the obtained flow field is similar to the case of no thin plate, while the right vortex near the top surface of the beam naturally disappears because it is obstructed by the thin plate. Since the thin plate is hotter than the surrounding gas, a thermal edge flow is induced along the plate from the gap region between its tip and the top surface of the beam towards its root. Thus, similar to the thermal edge flow appearing around the corners of the beam, the thermal edge flow appearing around the edge of the thin plate acts like a pump that sucks in gas from the region near the top surface of the beam. This results in a reduction in pressure on the top surface of the beam located near the thin plate, as seen in Fig. 4.6 (a). As a result, this increases the pressure difference between the bottom and top surfaces of the beam. Furthermore, since this hot thin plate is located near the right top corner of the cold beam, the temperature gradient near the right top corner is increased, as seen in Fig. 4.5 (a). Due to this, the upward thermal edge flow along the right side of the beam is enhanced, as seen in Fig. 4.5 (a) and Fig. 4.6 (a). This enhanced thermal edge flow along the right side of the beam carries molecules out of the region on the right side and, hence, induces the reduction in pressure on the right side of the beam, as seen in Fig. 4.6 (a), whereas the normalized pressure on the left side is the same as that for the case of no plate shown in Fig. 4.4 (a). In the case of no thin plate, the pressures on the right and left sides are the same because of symmetry in the field and, hence, no horizontal force appears. On the other hand, in the case when the thin plate is mounted and deviated rightward from the center of the beam, a rightward force is induced by the above-mentioned pressure difference appearing on the right and left sides of the beam.

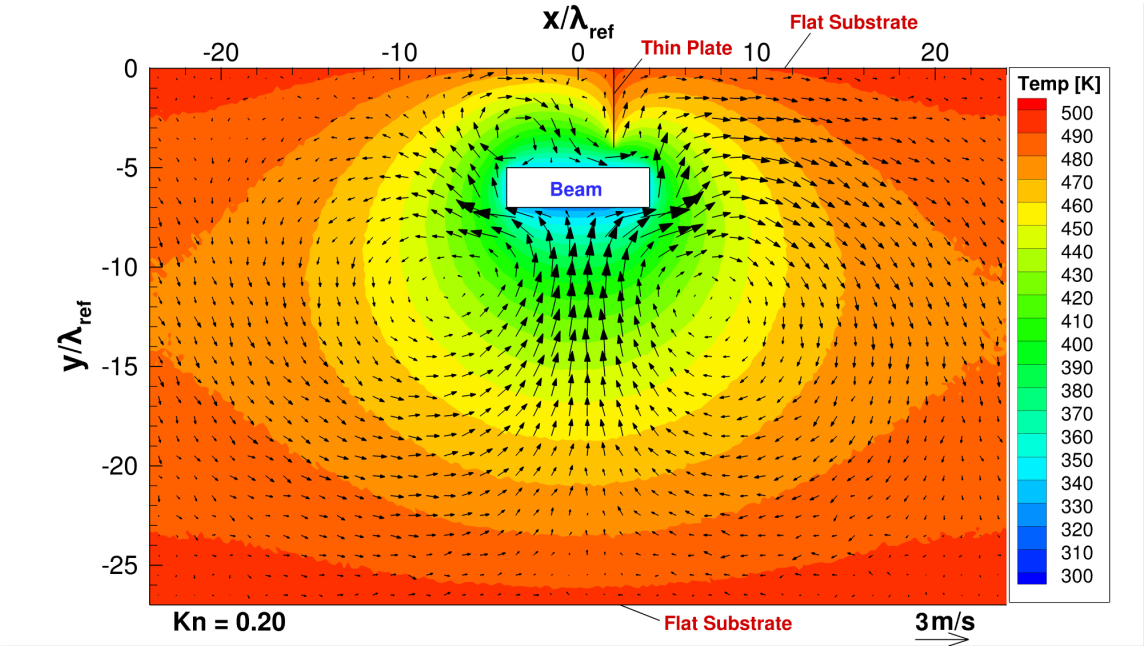

(a)

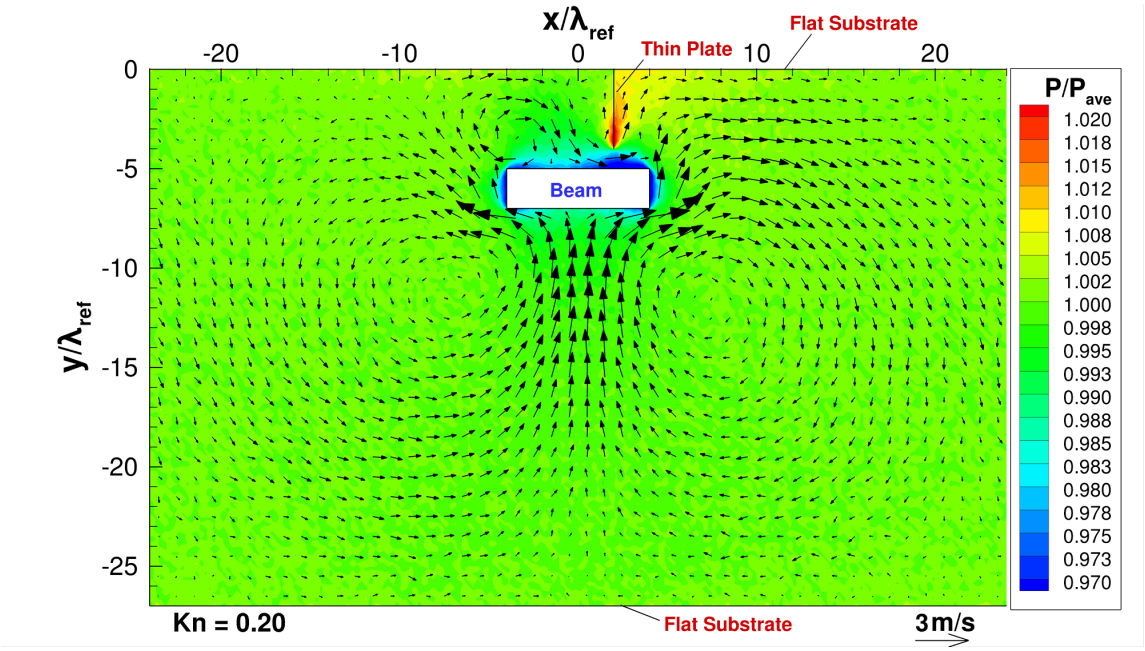

(b)

Fig. 4.5. (a) Flow and temperature distribution and (b) pressure distribution, when the beam is placed close to a heated thin plate mounted on a substrate, at Kn = 0.2. Reprinted with permission from C. J. C. Otic and S. Yonemura, Micromachines 13, 1092 (2022). Copyright 2022 Author(s).

Usually, in a gas, absolute values for the normal components of stress are much larger than those of its tangential components. This is because the normal component of stress includes the contribution of ambient pressure. If a figure of stress exerted on the beam surface is drawn, such as Fig. 4.4 (b), using the absolute stresses exerted on it, the tangential components of stresses are not visible since their absolute values are much smaller than those of normal components. Nevertheless, in general, if a surface force due to ambient pressure or some other constant pressure is integrated over a surface of an object, the net force exerted on the object due to such pressure is zero. Therefore, the contribution of ambient pressure or some other constant pressure can be excluded when the net force exerted on the object is discussed. Considering this fact, it is convenient to subtract some constant pressure comparable to ambient pressure from the normal components of the local stress when the net force exerted on the beam is discussed. Due to this subtraction, the magnitudes of the normal components of stress can be expressed in the same order as those of the tangential components of stress. Here, firstly, the average pressure exerted on the beam surface, $\bar{p}_{\mathrm{surface}}$, which is obtained by averaging a pressure obtained by Eq. (4.1) over the beam surface is calculated, and then this superficially averaged pressure $\bar{p}_{\mathrm{surface}}$ is divided by the spatially averaged pressure p_{ave}. Then, the obtained value is subtracted from the normal component of the stress obtained by Eq. (4.1), which is also normalized by p_{ave}. Thus, local stresses relative to the superficially averaged pressure $\bar{p}_{\mathrm{surface}}$ exerted on the beam surface is obtained as follows:

$$\text{Normalized modified normal stress} = \frac{\text{normal stress}}{p_{\mathrm{ave}}} - \frac{\bar{p}_{\mathrm{surface}}}{p_{\mathrm{ave}}}, \tag{4.2a}$$

$$\text{Normalized modified tangential stress} = \frac{\text{tangential stress}}{p_{\mathrm{ave}}}. \tag{4.2b}$$

Here, in order to differentiate the thus-obtained stress from absolute pressure or absolute stress, it is called “modified stress”, of which the concept is similar to “gauge pressure”. Furthermore, note that in the present study, “normal stress” is reckoned as positive when it corresponds to a state of compression.

Figure 4.4 (b) shows the distribution of the modified stress exerted on the beam surface in the case of no thin plate. In this case, the ratio $\bar{p}_{\mathrm{surface}}/p_{\mathrm{ave}}$ was 0.9813. Here, the normal component of normalized modified stress has a value in the range -2×10^{-2} to 2×10^{-2} as shown in Fig. 4.4 (b). In the case of negative value, the modified stress is drawn as if it pulls the beam outward like a tension in Fig. 4.4 (b). However, the magnitudes of normalized

modified stresses are much smaller than the subtracted normalized pressure of 0.9813. Therefore, the tensile stresses in Fig.4. 4 (b) should not be considered real tension. Actually, they represent a positive but low pressure less than $0.9813\ p_{\mathrm{ave}}$. In Fig. 4.6 (b), we show the stress distribution, such as Figure 4.4 (b), for different case, where the same subtracted value as that for the case of no thin plate in Fig. 4.4 (b), i.e., 0.9813, was used. The same process is done for the stress distributions like Fig. 4.4 (b) presented in Sec. 4.3.2–4.3.3. In Fig. 4.4 (b), the superficially averaged pressure, $\bar{p}_{\mathrm{surface}}$, is chosen as the subtracted pressure to visualize the effective force due to stress on the beam. However, for the purpose of examining the net force on the beam, the subtracted pressure can be flexibly chosen, in a way that is convenient. Therefore, here, the same subtracted normalized pressure of 0.9813 is chosen for all the cases. Thanks to this choice, the normalized modified stress can be directly compared over all the cases.

In the case when there is no thin plate mounted on the substrate, as shown in Fig. 4.4 (b), the stresses are symmetric in the x-direction; hence, zero net force in the x-direction can be obtained. However, the magnitude of the pressure exerted on the bottom surface of the beam is slightly larger than that exerted on the top surface of the beam; hence, a non-zero net force is directed upward in the y-direction. This pressure difference can be seen also in the pressure distribution in Fig. 4.3 (b) and Fig. 4.4 (a), as mentioned above.

On the other hand, in the case when a thin plate is mounted on the substrate, as shown in Fig. 4.6 (b), the stresses are non-uniform and asymmetric horizontally and vertically. Specifically, as mentioned in the discussion for Fig. 4.6 (a), the stresses on the left and right sides of the beam are unequal, which result in a non-zero net force directed rightward. Furthermore, the presence of the thin plate causes an increase in the difference between the normal stresses exerted on the bottom and top surfaces of the beam, as mentioned above; hence, a stronger net force directed upward is obtained. Particularly, the upward force is stronger in the vicinity of the thin plate compared to the case of no thin plate shown in Fig. 4.4 (b). Here, note that the upward pulling force drawn in the vicinity of the thin plate represents not a real tension but a positive pressure, significantly smaller than the other parts of the beam surface, as mentioned above. These non-zero net forces are caused by the pressure differences on the surfaces of the beam, whose mechanism is described in the fifth paragraph of this section. The results show here that by mounting a thin plate on a flat substrate, a force that attracts the beam to the plate horizontally and vertically is induced.

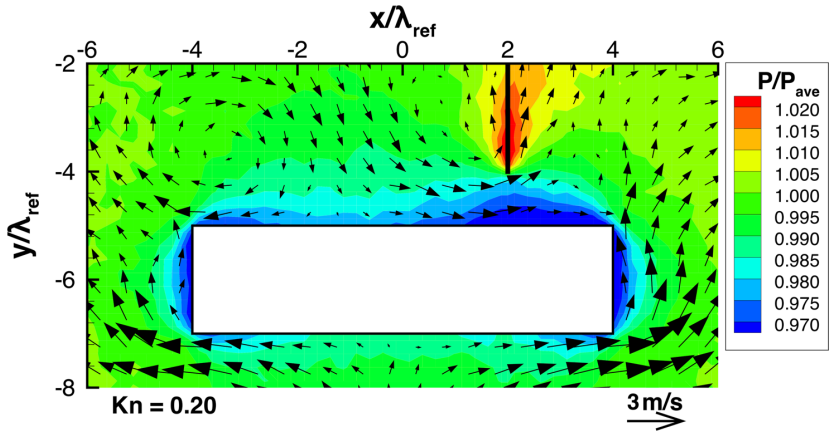

(a)

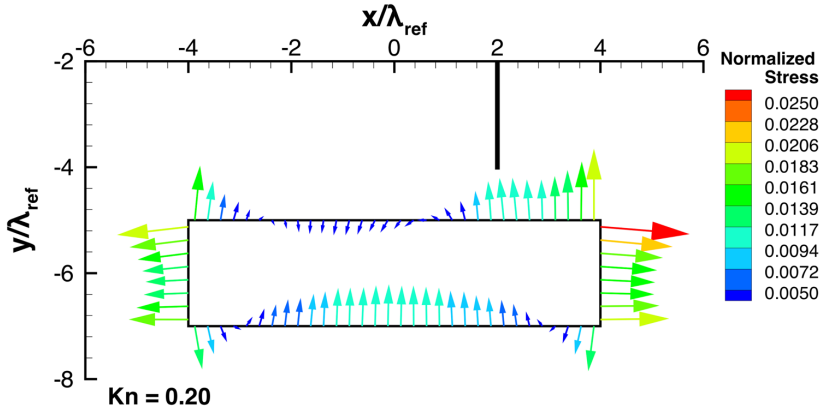

(b)

Fig. 4.6. (a) Pressure and flow distributions around the beam, and (b) stress distributions on the beam surfaces, when the beam is placed close to a heated thin plate mounted on a substrate, at Kn = 0.2. Reprinted with permission from C. J. C. Otic and S. Yonemura, Micromachines 13, 1092 (2022). Copyright 2022 Author(s).

4.3.2 Effect of the position of the thin plate

Next, let us consider how the position of the thin plate relative to the beam affects the stress and the resultant net force exerted on the beam, by adjusting the deviation distance, l_{dev}, while keeping all other parameters constant. Figure 4.7 (a) to Fig. 4.7 (d) show the stress distributions on the beam surface for such cases. Figure 4.8 shows the dependencies of the resultant net rightward and upward forces, F_x and F_y, exerted on the beam on the deviation distance, l_{dev}. Here, the rightward and upward forces, F_x and F_y, are normalized by the forces exerted on the left side and the bottom surface due to the spatially averaged pressure p_{ave}, i.e., $p_{\mathrm{ave}} \times h$ and $p_{\mathrm{ave}} \times w$, respectively.

Consider the case of no thin plate shown in Fig. 4.4 (b) as a reference case. By mounting a thin plate on the substrate just above the center of the beam, as shown in Fig. 4.7 (a), the high pressure on the central region of the top surface of the beam shown in Fig. 4.4 (b) is weakened, while the stresses exerted on the other surfaces are almost the same as those of the case of no thin plate. This results in the strong upward net force, as shown in Fig. 4.8 (a). This net upward force is 0.009-times as strong as the force due to the spatially average pressure p_{ave}. In the case when the system is in the atmospheric air condition, a lift force of about 900 Pa can be obtained. Assuming that the beam is of silicon material (2329 $\mathrm{kg/m^3}$ [36]), this lift force is equivalent to the force that levitates the beam with a height of 40 mm.

As the position of the thin plate is moved rightward away from the center of the beam, the region on the top surface of the beam where the pressure is reduced by the upward thermal edge flow towards the thin plate moves rightwards together with the position of the thin plate, as shown in Fig. 4.6 (b) and Fig. 4.7 (a)–(d). Since the region of pressure reduction is gradually deviated from the center of the beam as the thin plate moves rightward from the center of the beam, the net upward force decreases with increasing l_{dev}, as shown in Fig. 4.8 (a). Note that even in the case of no thin plate, the net upward force is non-zero. It is indicated by a horizontal solid line in Fig. 4.8 (a). In Fig. 4.8 (a), the position of the edge of the beam, $x = 0.5w$, i.e., $x = 4\lambda_{\mathrm{ref}}$, is also indicated by the vertical solid line. By mounting a thin plate on the flat substrate, the net upward force is enhanced, as shown in Fig. 4.8 (a). However, this is only true up to the point when the position of the thin plate is at $l_{\mathrm{dev}} = 0.75w$ from the center of the beam, where the net upward force approaches that of the case of no thin plate. Note that in the case of $l_{\mathrm{dev}} = 0.75w$, the thin plate is located outside the region above the beam, i.e., $-0.5w \leq x \leq 0.5w$.

Simultaneously, as the thin plate is moved towards the edge of the beam from its center, the pressure on the right side of the beam is gradually reduced, as shown in Fig. 4.6 (b) and Fig. 4.7 (a)–(c). As a result, the net rightward force appears and increases with increasing l_{dev}, up to the edge of the beam, i.e., $0 < l_{\mathrm{dev}} \leq 0.5w$, as shown in Fig. 4.8 (b). Similarly to Fig. 4.8 (a), the position of the edge of the beam, $x = 0.5w$, is indicated in Fig. 4.8 (b). The net rightward force obtained when the thin plate is located at the right edge of the beam is 0.0045-times as strong as the force due to the spatially average pressure p_{ave}. In the case when the system is in the atmospheric air condition, a rightward force of about 450 Pa can be obtained. Assuming that the beam is of silicon material, this force is equivalent to the force that accelerates the beam with a width of 20 mm rightward with the earth's gravitational acceleration. However, when the position of the thin plate is moved further away from the edge

of the beam, the reduction in pressure on the right side of the beam is decreased, as shown in Fig. 4.7 (d). As a result, the net rightward force decreases as the thin plate is moved further away from the edge of the beam, i.e., $l_{\mathrm{dev}} > 0.5w$, as shown in Fig. 4.8 (b).

Nevertheless, the results here show that in a range of $0 < l_{\mathrm{dev}} \leq 0.75w$, the net force is always directed upward and rightward, i.e., it always attracts the beam to the plate horizontally and vertically. Therefore, by using these thermally induced forces, the mechanism where the thin plate acts like tweezers that can trap the beam is obtained.

4.3.3 Effect of height of the beam

Next, let us investigate the effect of the height of the beam, h, on the stress and the resultant net force exerted on the beam, by adjusting the beam height, h, while keeping all other parameters constant. For such cases, Fig. 4.9 (a) and Fig. 4.10 (a) show the flow and pressure distributions near the beam, and Fig. 4.9 (b) and Fig. 4.10 (b) show the stress distributions on the beam surface. Figure 4.11 shows the dependencies of the resultant net rightward and upward forces, F_x and F_y, exerted on the beam on the height. Here, similar to what was done in Sec. 4.3.1–4.3.2, the rightward and upward forces, F_x and F_y, are normalized by the forces exerted on the left side and the bottom surface due to the spatially averaged pressure p_{ave}, i.e., $p_{\mathrm{ave}} \times h$ and $p_{\mathrm{ave}} \times w$, respectively.

Consider the case shown in Fig. 4.6, where $h = 0.25w$ and $l_{\mathrm{dev}} = 0.25w$, as the reference case. Firstly, let us compare the case when the beam height is decreased to $h = 0.125\,w$ as shown in Fig. 4.9, with the reference case. By decreasing the beam height, the thermal edge flows around the corners of the beam become stronger and the pressure on the top surface of the beam is decreased, as shown in Fig. 4.9 (a), compared to Fig. 4.6 (a). However, the high pressure on the central region of the bottom surface of the beam is almost the same as that of the reference case. As a result, the pressure difference between the bottom and top surfaces of the beam is increased, as seen in Fig. 4.9 and Fig. 4.6. Therefore, a stronger upward net force is generated, as shown in Fig. 4.11 (a). Simultaneously, as the beam height is decreased, the pressures on both the right side and the left side of the beam are reduced, as shown in Fig. 4.9 (a) and Fig. 4.6 (a). Although the pressure is decreased on both sides, the pressure reduction on the right side is slightly greater than that on the left side, as shown in Fig. 4.9 and Fig. 4.6. Therefore, a stronger rightward net force is generated, as shown in Fig. 4.11 (b).

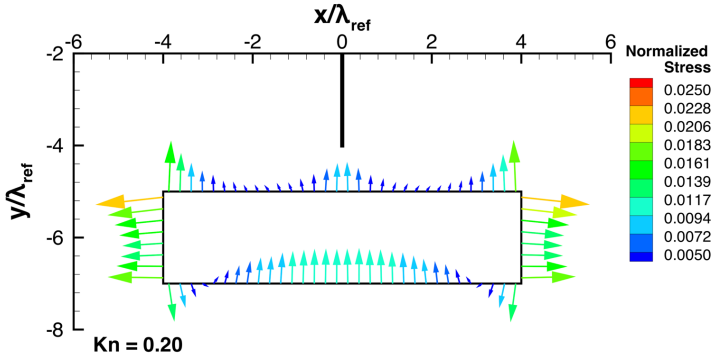

(a)

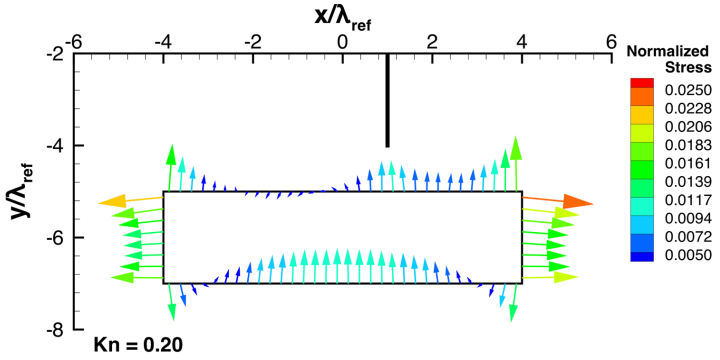

(b)

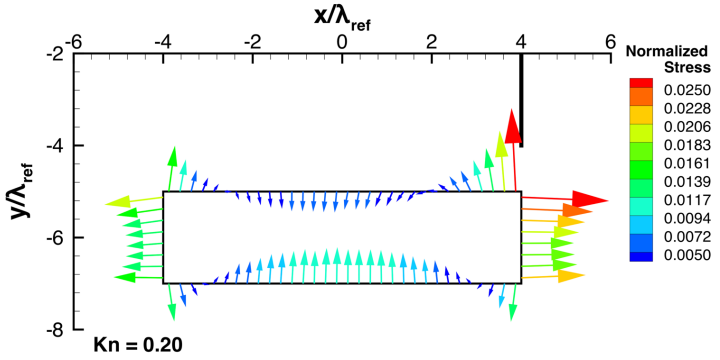

(c)

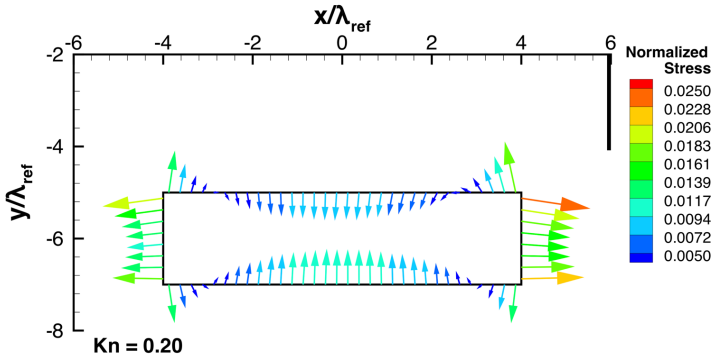

(d)

Fig. 4.7. Stress distributions for different deviation distances, l_{dev}, at Kn = 0.2. (a) $l_{\mathrm{dev}} = 0$. (b) $l_{\mathrm{dev}} = 0.125w$. (c) $l_{\mathrm{dev}} = 0.5w$. (d) $l_{\mathrm{dev}} = 0.75w$. Reprinted with permission from C. J. C. Otic and S. Yonemura, Micromachines 13, 1092 (2022). Copyright 2022 Author(s).

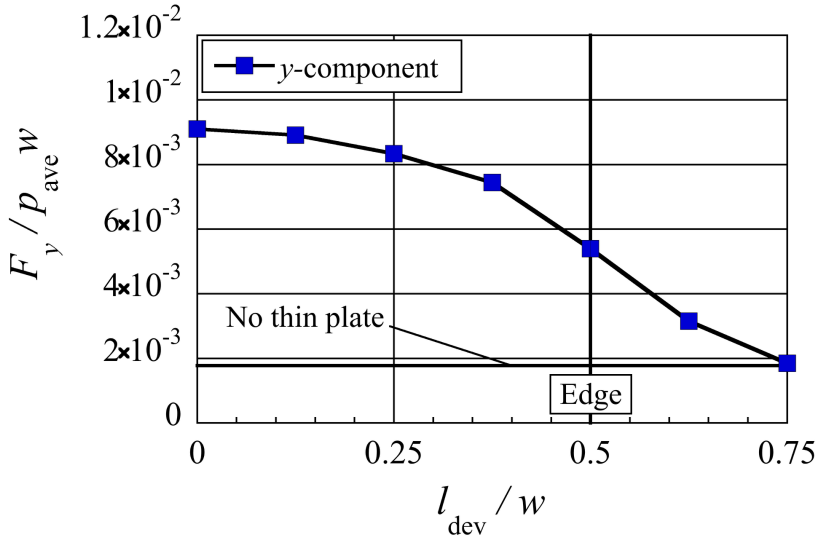

(a)

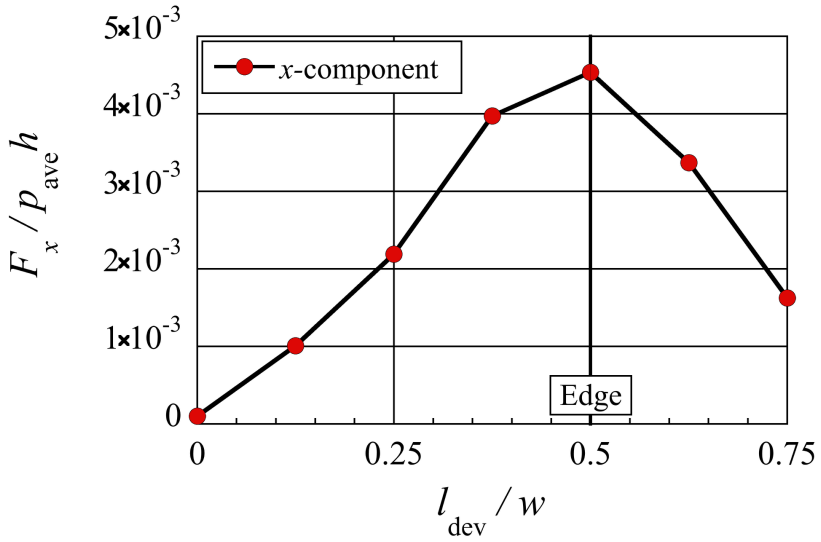

(b)

Fig. 4.8. Net (a) upward and (b) rightward forces exerted on the beam for different deviation distances, l_{dev}, at Kn = 0.2. Reprinted with permission from C. J. C. Otic and S. Yonemura, Micromachines 13, 1092 (2022). Copyright 2022 Author(s).

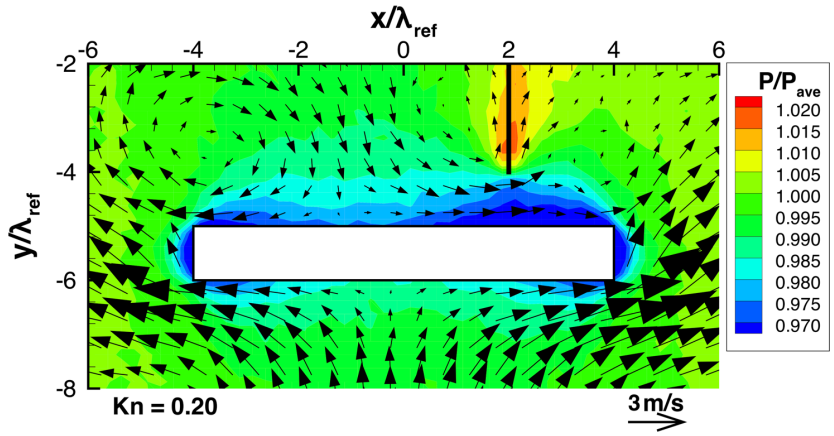

(a)

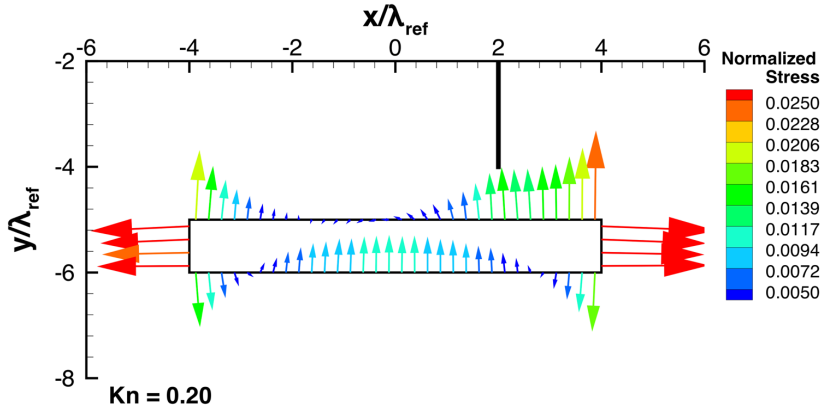

(b)

Fig. 4.9. (a) Pressure and flow distributions around the beam, and (b) stress distributions on the beam surfaces for a beam height of $h = 0.125w$, at Kn $= 0.2$. Reprinted with permission from C. J. C. Otic and S. Yonemura, Micromachines 13, 1092 (2022). Copyright 2022 Author(s).

Secondly, let us compare the case when the beam height is changed to $h = 0.375w$, with the reference case. By increasing the beam height, as shown in Fig. 4.10 (a), the thermal edge flows around the corners of the beam become weaker and the reduction in the pressure on the top surface of the beam is decreased compared to Fig. 4.6 (a). However, the high pressure on the central region of the bottom surface of the beam remains almost the same as that of the reference case. As a result, the pressure difference between the bottom and top surfaces of the beam is decreased, as seen in Fig. 4.10 and Fig. 4.6. Therefore, upward net force is weakened, as shown in Fig. 4.11 (a). Simultaneously, as the beam height is increased, the reductions in the pressures on both the right side and the left side of the beam are decreased, as shown in Fig. 4.10 (a) and Fig. 4.6 (a). The decrease in the reductions in the pressures on both sides indicates

that the pressures on both sides become closer to the average pressure and, hence, the pressure difference between both sides becomes smaller. Therefore, a rightward net force is still generated, but weaker, as shown in Fig. 4.11 (b). The results presented here and in the previous paragraph show that for a shorter beam height, the net upward and rightward forces are stronger.

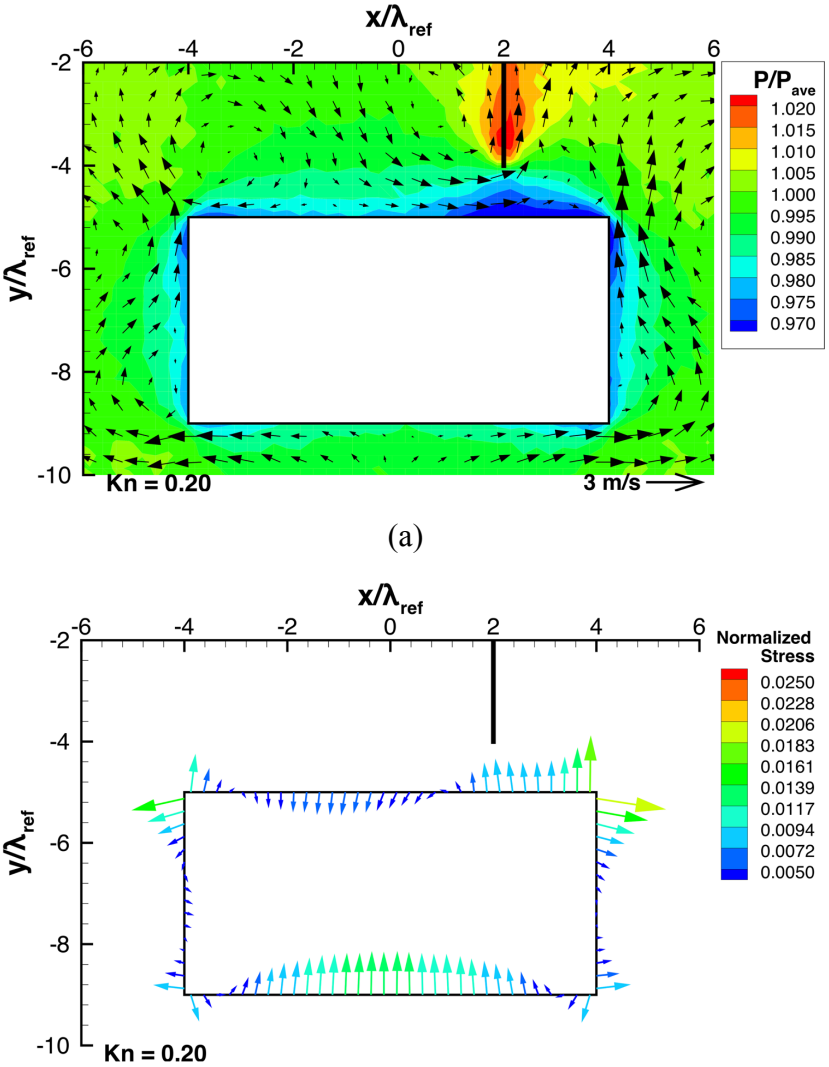

Fig. 4.10. (a) Pressure and flow distributions around the beam, and (b) stress distributions on the beam surfaces for a beam height of $h = 0.375w$, at Kn $= 0.2$. Reprinted with permission from C. J. C. Otic and S. Yonemura, Micromachines 13, 1092 (2022). Copyright 2022 Author(s).

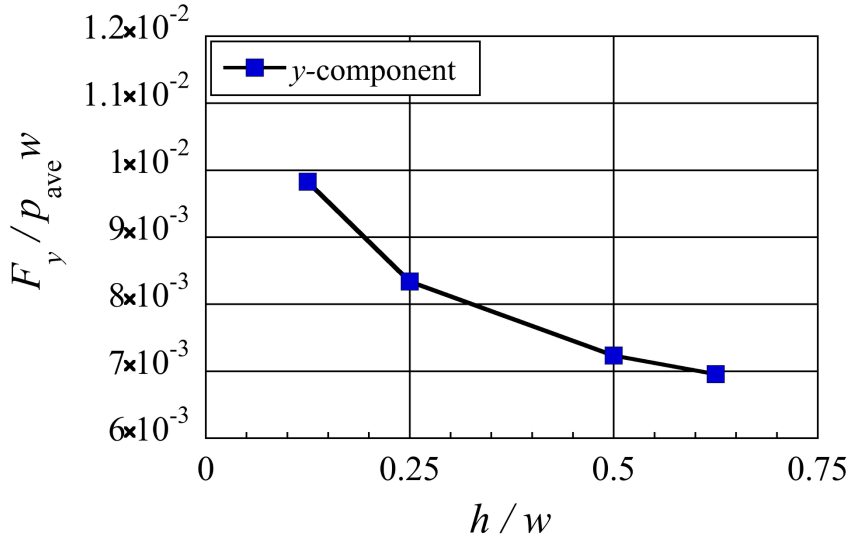

(a)

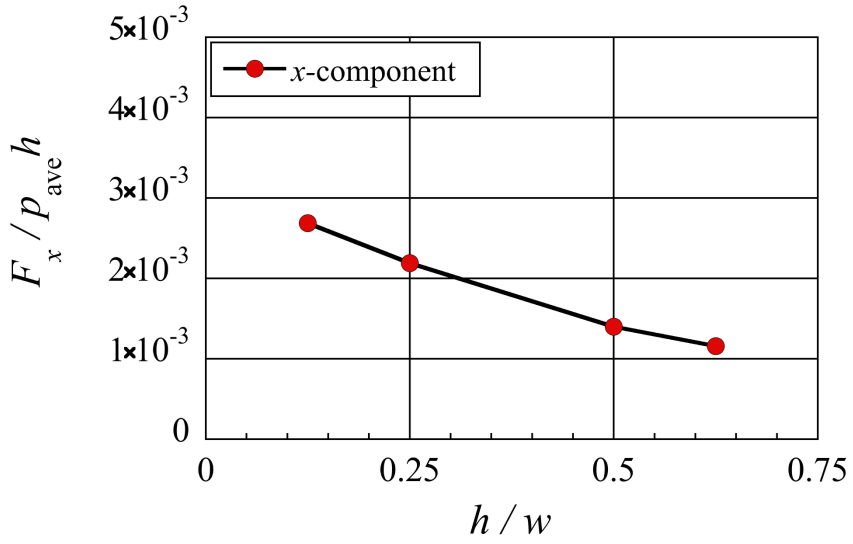

(b)

Fig. 4.11. Net (a) upward and (b) rightward forces exerted on the beam for different beam heights, h, at Kn = 0.2. Reprinted with permission from C. J. C. Otic and S. Yonemura, Micromachines 13, 1092 (2022). Copyright 2022 Author(s).

4.3.4 Effect of lower temperature differences

So far, only a temperature difference of 200 K has been considered. Now, let us consider the effect of using temperature differences lower than 200 K between the heated substrate (thin plate) and the colder object (beam), i.e., $T_{\mathrm{sub}} - T_{\mathrm{obj}}$, on the net forces. Figure 4.12 shows the distribution of the resultant net rightward and upward forces, F_x and F_y, exerted on the beam, for various temperature differences less than and equal to 200 K at $\mathrm{Kn} = 0.2$. Here, the temperature difference $T_{\mathrm{sub}} - T_{\mathrm{obj}}$ is changed while the middle value $(T_{\mathrm{sub}} + T_{\mathrm{obj}})/2$ is kept at 400 K. Similar to what was done in Sec. 4.3.2–4.3.3, the rightward and upward forces, F_x and F_y, are normalized by the forces exerted on the left side and the bottom surface due to the spatially averaged pressure p_{ave}, i.e., $p_{\mathrm{ave}} \times h$ and $p_{\mathrm{ave}} \times w$, respectively. It can be seen from Fig. 4.12 that as the temperature difference is decreased from 200 K, both the net upward and rightward forces decrease. Specifically, both the net upward and rightward forces are proportional to the temperature difference, and both vanish in the case of no temperature difference, i.e., $T_{\mathrm{sub}} = T_{\mathrm{obj}}$. As discussed in previous sections, the reduction in pressure around the surface of the beam is due to the thermal edge pump effect. A low-temperature difference means that the strength of the thermal edge flows is weak. This results in smaller reductions in pressure around the beam and, hence, weaker net upward and rightward forces. In the case of the minimum temperature difference considered here at 25K, under the atmospheric air condition, a lift force of about 100 Pa and a rightward force of about 20 Pa can be obtained. Assuming that the beam of silicon material of the density of $2329\ \mathrm{kg/m^3}$, this lift force is equivalent to the force that levitates the beam with a height of 4 mm, and the rightward force is equivalent to the force that accelerates the beam with a width of 0.8 mm rightward with the Earth's gravitational acceleration. Thus, the obtained force for low-temperature differences is still large enough to move a small object less than 1 mm. Therefore, even at the low temperature difference of 25 K, the mechanism proposed in this study can still be achieved.

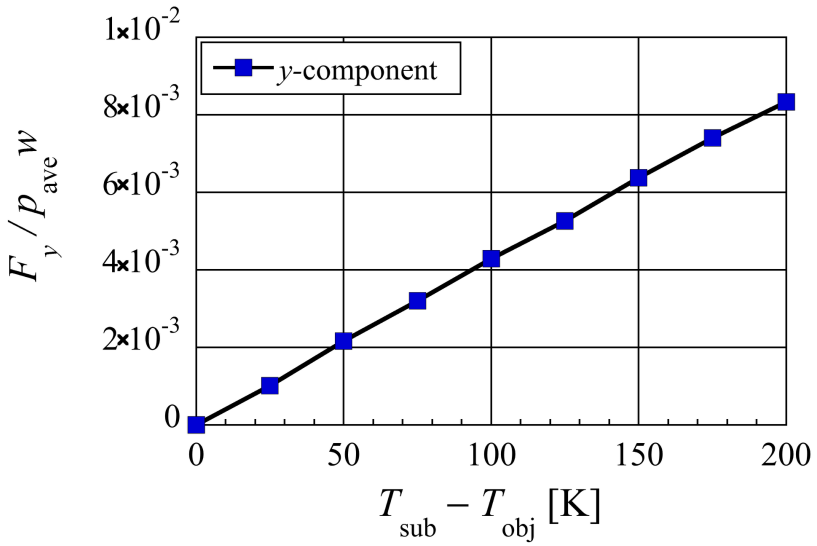

(a)

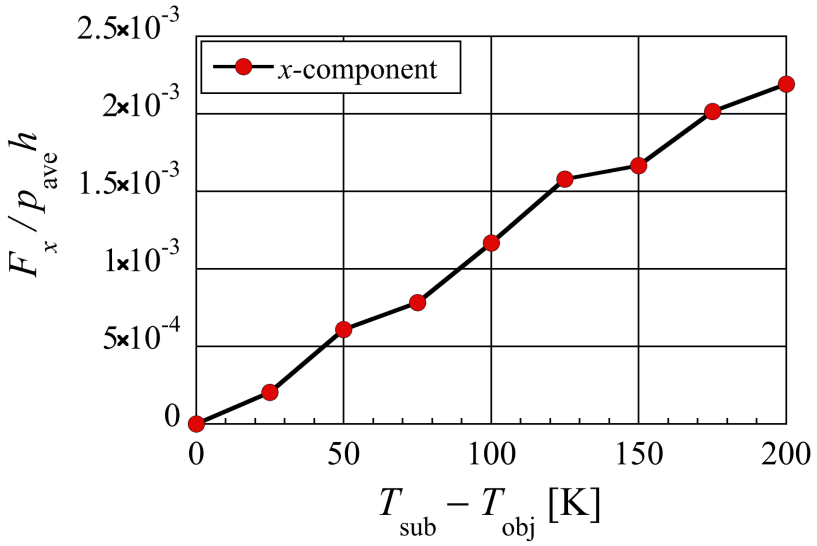

(b)

Fig. 4.12. Net (a) upward and (b) rightward forces exerted on the beam at different temperature differences, in the case of Kn = 0.2 and $(T_{\mathrm{sub}} + T_{\mathrm{obj}})/2 = 400$ K. Reprinted with permission from C. J. C. Otic and S. Yonemura, Micromachines 13, 1092 (2022). Copyright 2022 Author(s).

4.3.5 Effect of Knudsen number

Up to this point, only a Knudsen number of $\mathrm{Kn} = 0.2$ was considered. Now, let us consider the effect of different Knudsen number cases on the net forces. Figure 4.13 shows the resultant net rightward and upward forces, F_x and F_y, exerted on the beam, for various Knudsen numbers. Here, the Knudsen number is adjusted by adjusting all the lengths of the setup considered here while keeping the gas mean free path λ_{ref} constant, i.e., keeping the reference gas pressure p_{ref} constant. For example, the total gap distance g_{tot} is adjusted as $g_{\mathrm{tot}} = \lambda_{\mathrm{ref}}/\mathrm{Kn}$. Similar to what was done in Sec. 4.3.2–4.3.4, the rightward and upward forces, F_x and F_y, are normalized by the forces exerted on the left side and the bottom surface due to the spatially averaged pressure p_{ave}, i.e., $p_{\mathrm{ave}} \times h$ and $p_{\mathrm{ave}} \times w$, respectively. It can be seen from Fig. 4.13 that the net upward force and the net rightward force are both maximum around $\mathrm{Kn} \approx 0.2$, which is used as the reference Kn throughout this study, and both become small at low Knudsen numbers $\mathrm{Kn} < 0.05$ and high Knudsen numbers $\mathrm{Kn} > 1$. Note that the Knudsen number here is evaluated based on the total gap distance, g_{tot}, such that $\mathrm{Kn} = \lambda_{\mathrm{ref}}/g_{\mathrm{tot}}$.

As discussed in previous sections, the reduction in pressure around the surface of the beam is due to the thermal edge pump effect. Specifically, the low-pressure region on the top surface of the beam is increased by the thermal edge flow induced on the tip of the thin plate. Therefore, considering the local Knudsen number between the tip of the thin plate and the top surface of the beam, i.e., $\mathrm{Kn}_{\mathrm{tip}} = \lambda_{\mathrm{ref}}/g_{\mathrm{tip}}$, is significant when discussing the effect of the Knudsen number on the net forces. Note that $\mathrm{Kn}_{\mathrm{tip}} = 5\mathrm{Kn}$ since $g_{\mathrm{tip}} = g_{\mathrm{tot}}/5$. Using $\mathrm{Kn}_{\mathrm{tip}}$, the above-mentioned knowledge can be restated as follows: the net upward force and the net rightward force are both maximum around $\mathrm{Kn}_{\mathrm{tip}} \approx 1$ and both become small at low Knudsen numbers $\mathrm{Kn}_{\mathrm{tip}} < 0.25$ and high Knudsen numbers $\mathrm{Kn}_{\mathrm{tip}} > 5$. This means that the thermally induced forces, which attract the beam to the thin plate horizontally and vertically, are optimum when the distance between the beam and the thin plate is in the order of one mean free path, as what is used throughout this study.

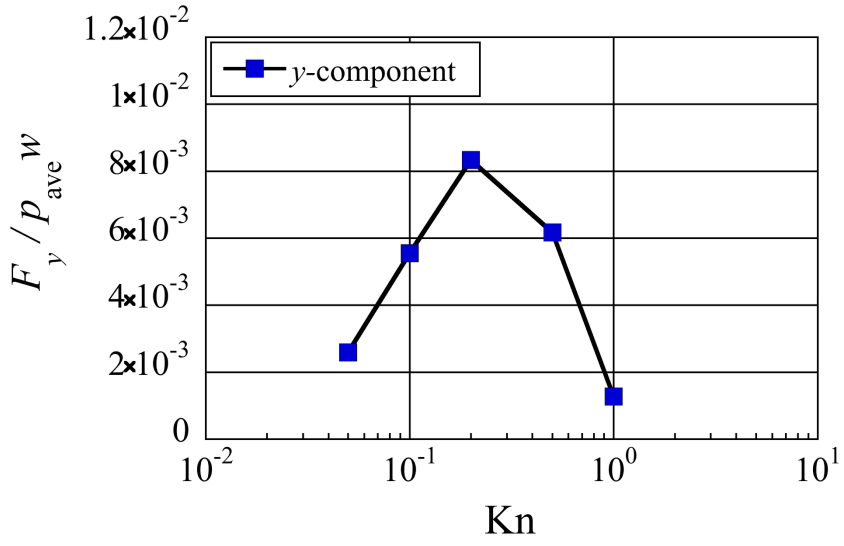

(a)

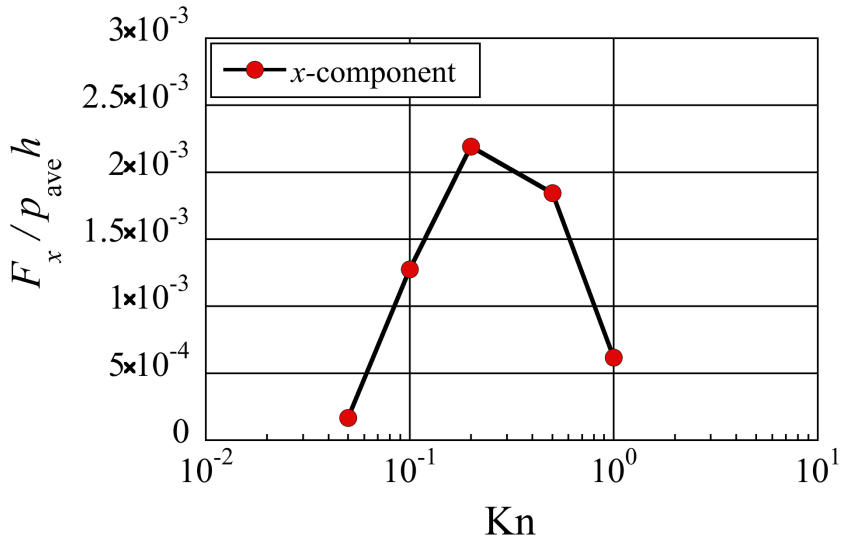

(b)

Fig. 4.13. Net (a) upward and (b) rightward forces exerted on the beam at different Knudsen numbers. Reprinted with permission from C. J. C. Otic and S. Yonemura, Micromachines 13, 1092 (2022). Copyright 2022 Author(s).

4.3.6 Summary of the mechanism

Finally, the mechanism of the generation of Knudsen forces for the configuration proposed here and how it can be exploited to trap and manipulate a micro-object (beam), can be summarized. In the vicinity of the corners of the isothermal beam, the isothermal surfaces in the gas are largely curved to surround the sharp corners. Such a temperature distribution gives rise to thermal edge flows that result in the thermal edge pump phenomenon. This pumping effect moves molecules away from the region around the beam surfaces and then generates low-pressure regions around the beam surfaces. As a result, pressure-driven flows appear to compensate the decrease in molecules in the low-pressure regions, as illustrated in Fig. 4.14 (a). The low-pressure region on the top surface of the beam is more weakly compensated than the low-pressure region on the bottom surface of the beam, since only a smaller number of molecules can be gathered in the narrow space between the top surface of the beam and the upper substrate than the wider space between the bottom surface of the beam and the lower substrate. This results in lower pressure on the top surface of the beam than that on the bottom surface of the beam. This pressure difference results in a net upward force, as illustrated in Fig. 4.14 (a).

When a thin plate is mounted perpendicularly on the flat substrate, the thermal edge pump phenomenon is enhanced by the additional thermal edge flow at the tip of the thin plate. This additional pumping effect enhances the pressure reduction on the top surface of the beam, as illustrated in Fig. 4.14 (b). Furthermore, if the thin plate deviates from the center of the beam, i.e., it is closer to the right edge of the beam, the pressure reduction on the right side of the beam is enhanced, as illustrated in Fig. 4.14 (b). Meanwhile, the pressures at the bottom surface and left side of the beam are unaffected, whether there is a thin plate or not. In this case, a pressure difference between the left and right sides of the beam is generated, and the pressure difference between the top and bottom surfaces of the beam is increased, as illustrated in Fig. 4.14 (b). This results in a net rightward force and a stronger net upward force. Therefore, using the induced Knudsen forces here, the thin plate acts as a tweezer-like mechanism that can trap and manipulate the beam (micro-object) without contact. Note that as the Knudsen force depends on factors, such as the temperature difference, the Knudsen number, and the shape of the configuration, e.g., the geometry of micro-object; the strength and behavior of the phenomenon discussed here also depends on such factors.

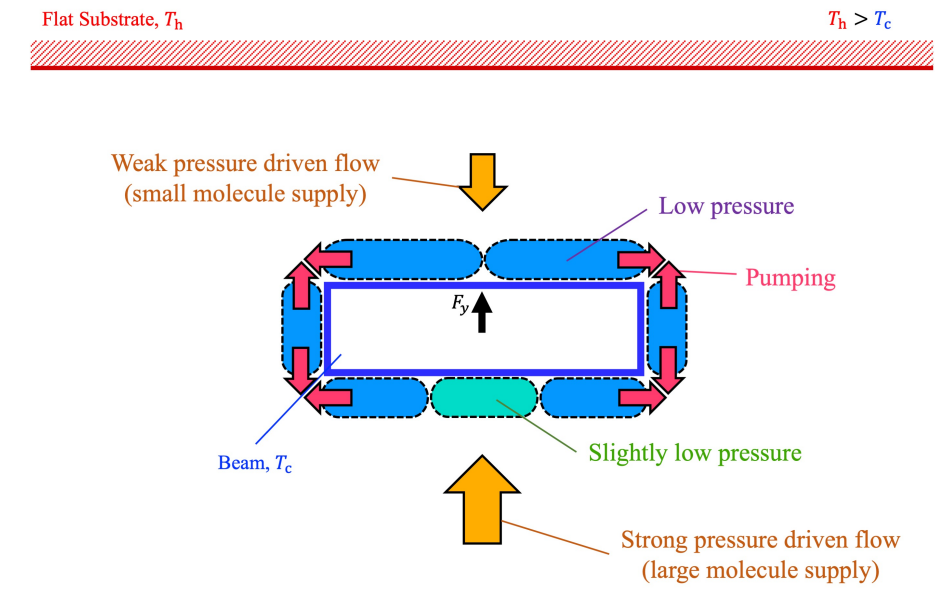

(a)

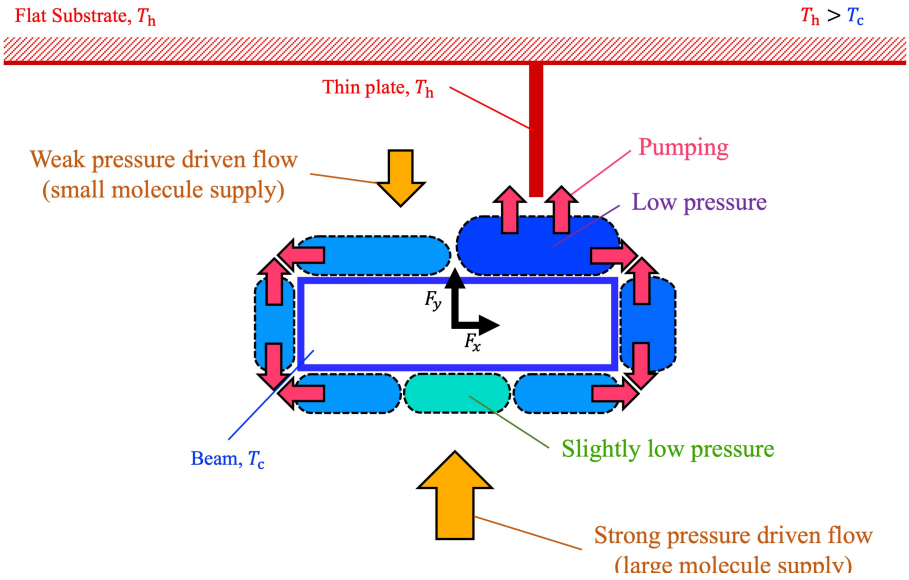

(b)

Fig. 4.14. Schematic of the mechanism of the thermally induced forces on the beam (a) when the beam is placed close to a flat substrate, and (b) when the beam is placed close to a heated thin plate mounted on a substrate. Reprinted with permission from C. J. C. Otic and S. Yonemura, Micromachines 13, 1092 (2022). Copyright 2022 Author(s).

4.4 Conclusion

In this study, it is proposed that the phenomenon of thermally induced Knudsen forces can be exploited to manipulate a micro-object. Specifically, a concept of a tweezer-like mechanism that can trap and grasp a micro-object without contact was presented. Using the DSMC method, it was demonstrated that the proposed mechanism is achieved when a heated thin plate mounted perpendicularly on a flat substrate is placed close to a micro-object, which, in this case, is a beam. The driving mechanism is mainly due to the pressure differences induced by the thermal edge flows at the corners of the beam and the thermal edge flow at the tip of the thin plate. These flows act like pumps that move gas molecules from the colder regions to the hotter regions around the edges. When the thin plate is above the beam, the pressure on the top surface of the beam is lower than that on its bottom surface. Furthermore, when the thin plate is located away from the center of the beam and is near the right side of the beam, the pressure on the right side of the beam is lower than that on its left side. Due to these pressure differences between the top and bottom surfaces and between the left and right sides of the beam, a force that attracts the beam to the plate horizontally and vertically is induced. On the other hand, in the case when the height of the beam is shorter, this phenomenon is enhanced, such that a stronger net upward and rightward force is induced. Furthermore, both the net upward and rightward forces were found to be proportional to the temperature difference, and both vanish in the case of no temperature difference. However, even at the low-temperature difference of 25 K, the obtained force is still large enough to move a small object less than 1 mm and, hence, the mechanism proposed in this study can still be achieved. Moreover, it was also found that these thermally induced Knudsen forces are optimum when the distance between the beam and the thin plate is in the order of one mean free path. In this study, the micro-object of interest is represented by a beam. Whether the mechanism proposed here also applies to other shapes, such as a sphere, remains in question and will be a subject of future research.

References

[1] A. Passian, A. Wig, F. Meriaudeau, T.L. Ferrel, and T. Thundat, "Knudsen forces on microcantilevers," *Journal of Applied Physics* 92, 6326(2002).

[2] A. L. Lereu, A. Passian, R. J. Warmack, T. L. Ferrell, and T. Thundat, "Effect of thermal variations on the Knudsen forces in the transitional regime," *Applied Physics Letters* 84, 1013–1015 (2004).

[3] B. W. Harris, F. Chen, and U. Mohideen, "Precision measurement of the Casimir force using gold surfaces," *Physical Review A* 62, 052109 (2000).

[4] B. Gotsmann, and U. Dürig, "Experimental observation of attractive and repulsive thermal forces on microcantilevers," *Applied Physics Letters* 87, 194102 (2005).

[5] A. Strongrich, and A. Alexeenko, "Microstructure actuation and gas sensing by the Knudsen thermal force," *Applied Physics Letters* 107, 193508 (2015).

[6] A. Alexeenko, A. Strongrich, A. G. Cofer, A. Pikus, I. B. Sebastiao, S. S. Tholeti, and G. Shivkumar, "Microdevices enabled by rarefied flow phenomena," *AIP Conference Proceedings* 1786, 080001 (2016).

[7] A. Hassanvand, M. B. Gerdroodbary, R. Moradi, and Y. Amini, "Application of Knudsen thermal force for detection of inert gases," *Results in Physics* 9, 351–358 (2018

[8] D. D. Vo, R. Moradi, M. B. Gerdroodbary, D. D. Ganji, " Measurement of low-pressure Knudsen force with deflection approximation for gas detection," *Results in Physics* 13, 102257 (2019).

[9] A. Pikus, I. B. Sebastião, A. Strongrich, amd A. Alexeenko, "Characterization of a Knudsen force based vacuum sensor for N2H2O gas mixtures," *Vacuum* 161, 130–137 (2019).

[10] A. Strongrich, W. O'Neill, A. Cofer, and A. Alexeenko,, "Experimental measurements and numerical simulations of the Knudsen force on a non-uniformly heated beam," *Vaccuum* 109, 405–416 (2014).

[11] C.J.C. Otic and S. Yonemura, “Mechanism of tangential Knudsen force at different Knudsen numbers,” *Physics of Fluids* [in press] (2022).

[12] Q. Li, T. Liang, and W. Ye, “Shape-dependent orientation of thermophoretic forces in microsystems,” *Physical Review E* 88, 033020 (2013).

[13] Q. Li, T. Liang, and W. Ye, “Knudsen torque: A rotational mechanism driven by thermal force,” *Physical Review E* 90, 033009 (2014).

[14] C.J.C. Otic and S. Yonemura, “Effect of different surface microstructures in the thermally induced self-propulsion phenomenon,” *Micromachines* 13, 871 (2022).

[15] J. Nabeth, S.Chigullapalli, and A. Alexeenko, “Quantifying the Knudsen force on heated microbeams: A compact model and direct comparison with measurements,” *Physical Review E* 83, 066306 (2011).

[16] T. Zhu and W. Ye, “Origin of Knudsen forces on heated microbeams,” *Physical Review E* 82, 036308 (2010).

[17] T. Zhu, W. Ye, and J. Zhang, “Negative Knudsen force on heated microbeams,” *Physical Review E* 84, 056316 (2011).

[18] A. Passian, R. J. Warmack, T. L. Ferrell, and T. Thundat, “Thermal transpiration at the microscale: a Crookes cantilever,” *Physical Review Letters* 90, 124503 (2003).

[19] X. Wang, Z. Zhang, W. Zhang, T. Su, and S. Zhang, “Impact of improved design on Knudsen force for micro gas sensor,” *Micromachines* 11, 634 (2020).

[20] A. Ashkin, J. M. Dziedzic, J. E Bjorkholm, and S. Chu, “Observation of a single-beam gradient force optical trap for dielectric particles,” *Optics Letters* 11, 288 (1986).

[21] J. E. Curtis, B. A. Koss, B.A., and D. G. Grier, “Dynamic holographic optical tweezers,” *Optics Communication* 207, 169–175 (2002).

[22] D. G. Grier, “A revolution in optical manipulation,” *Nature* 424, 810–816 (2003).

[23] J. O. Kessler, “Hydrodynamic focusing of motile algal cells,” *Nature* 313, 218–220 (1985).

[24] G.B. Lee, B. H. Hwei, and G. R. Huang, G.R. “Micromachined pre-focused M x N flow switches for continuous multi-sample injection,” *Journal of Micromechanics and Microengineering* 11, 654–661 (2001).

[25] N. Sundararajan, M. S. Pio, L. P. Lee, and A. A. Berlin, "Three-dimensional hydrodynamic focusing in polydimethylsiloxane (PDMS) microchannels," *Journal of Microelectromechanical Systems* 13, 559–567 (2004).

[26] A. Shenoy, C. V. Rao, and C. M. Schroeder, "Stokes trap for multiplexed particle manipulation and assembly using fluidics," *Proceedings of the National Academy of Sciences* 113, 3976-3981 (2016).

[27] U. G. Būtaitė, G. M. Gibson, YL. D. Ho, M. Taverne, J. M. Taylor, and D. B. Phillips, "Indirect optical trapping using light driven micro-rotors for reconfigurable hydrodynamic manipulation," *Nature Communications* 10, 1215 (2019).

[28] K. Setoura, T. Tsuji, S. Ito, S. Kawano, and H. Miyasaka, "Opto-thermophoretic separation and trapping of plasmonic nanoparticles," *Nanoscale* 11, 21093-21102 (2019).

[29] T. Tsuji, Y. Matsumoto, R. Kugimiya, K. Doi, and S. Kawano, "Separation of nano- and microparticle flows using thermophoresis in branched microfluidic channels. *Micromachines* 10, 321 (2019).

[30] A. Ashkin and J. M. Dziedzic, "Optical levitation by radiation pressure," *Applied Physics Letters* 19, 283 (1971).

[31] K. C. Neuman and S. M. Block, S.M.; "Optical trapping," *Review of Scientific Instruments* 75, 2787 (2004).

[32] P. C. Nordine and R. M. Atkins, "Aerodynamic levitation of laser-heated solids in gas jets," *Review of Scientific Instruments* 53, 1456 (1982).

[33] Y. L. Pan, C. Wang, S. C. Hill, M. Coleman, L. A. Beresnev, and J. L. Santarpia, "Trapping of individual airborne absorbing particles using a counterflow nozzle and photophoretic trap for continuous sampling and analysis," *Applied Physics Letters* 104, 113507 (2014).

[34] W.G. Vincenti and C. H. Kruger, *Introduction to Physical Gas Dynamics* (Krieger Publishing Company, Malabar, 1975).

[35] National Astronomical Observatory of Japan, *Rika Nenpyo: Chronological Scientific Tables 2007* (Maruzen, Tokyo, Japan, 2006). (In Japanese)

[36] G. Kaye and T. Laby, *Tables of Physical and Chemical Constant* (Longman, New York, USA, 1986).

[37] G. A. Bird, *Molecular Gas Dynamics and the Direct Simulation of Gas Flows* (Oxford, USA, 1994).

[38] K. Nanbu, "Direct simulation scheme derived from the Boltzmann equation I. Monocomponent gases," *Journal of the Physical Society of Japan* 49, 2042–2049(1980).

[39] K. Nanbu, "Stochastic solution method of the Boltzmann equation I," *The Memoirs the Institute of Fluid Science* 3, 47–93(1992).

[40] K. Nanbu, "Probability theory of electron–molecule, ion–molecule, molecule–molecule, and Coulomb collisions for particle modeling of materials processing plasmas and cases," *IEEE Transactions on Plasma Science* 28, 971–990(2000).

[41] Y. Sone, *Molecular Gas Dynamics: Theory, Techniques, and Applications* (Birkhauser, Boston, USA, 2007).

[42] H. Sugimoto and Y. Sone, "Vacuum pump without a moving part driven by thermal edge flow," AIP Conference Proceedings 762, 168-173 (2005).

Chapter 5 General Conclusion

This thesis studied thermally induced Knudsen forces on an object placed close to a heated structure using numerical and theoretical approaches.

In chapter 2, the object was considered to be infinitely wide at a cold temperature T_c, and placed close to an infinitely wide substrate of hot temperature T_h. The substrate has a surface structure repeated periodically in the x-direction. Four configurations were considered as the surface structures. One of them is the conventionally used ratchet configuration, and the others are its modifications. The flow was reproduced for each structure using numerical experiments by direct simulation Monte Carlo (DSMC) method, and the tangential Knudsen force induced on the bottom surface of the upper object, i.e., upper surface, was evaluated numerically. It was demonstrated that by modifying the commonly used ratchet structure, stronger tangential Knudsen forces can be obtained. New structures were proposed as alternatives to the ratchet structure that can optimize the tangential Knudsen force. Furthermore, it was found that the difference in the tangential Knudsen forces among these configurations is attributed to the difference in the tip angles. Namely, when the tip angle is decreased, the positive contribution to the rightward propulsive force due to molecules impinging on the bottom surface of the upper object directly from the oblique side without experiencing intermolecular collision remains unchanged, whereas the negative contribution to the rightward propulsive force due to molecules impinging on the bottom surface of the upper object directly from the modified side without experiencing intermolecular collision is reduced, and as a result, the rightward propulsive force increases with decreasing tip angle. From this, an intuitive explanation on the possible origin of the tangential Knudsen force was provided. In addition, it was also found that the tangential Knudsen force is affected not only by geometrical parameters but also by the Knudsen number and the temperature difference. The tangential Knudsen force peaks around $\mathrm{Kn} = 3$, i.e., in the transition flow regime, and vanishes in the continuum flow regime and in the free molecular flow regime. It can be seen that in the case of no temperature difference, i.e., $T_h = T_c$, the tangential Knudsen force vanishes in all the microstructures. As the temperature

difference is increased, the tangential Knudsen force increases linearly, whose slope varies depending on the microstructure.

In chapter 3, to clarify the mechanism of the tangential Knudsen force, a rigorous theoretical analysis was carried out. Using the ratchet configuration considered in chapter 2 as reference, a theoretical expression for x-momentum flux transferred by impinging molecules onto the upper surface was derived by considering the contributions of two kinds of impinging molecules separately. One is a group of molecules directly coming from the ratchet surfaces without experiencing intermolecular collisions, and the other is a group of molecules coming from the bulk region after experiencing intermolecular collisions there. The distributions of the tangential Knudsen stress evaluated in theoretical analysis were compared with those obtained in the numerical experiments by the DSMC method. In the transition flow regime, i.e., around $\mathrm{Kn} = 1$, both the distributions showed good agreement, but with some level of disparity. By adding the contribution of flow to the tangential stress, i.e., viscous shear stress, which is not considered in the theory, onto the theoretical results, the resulting distribution of the tangential Knudsen stress showed better agreement with that obtained in DSMC for $\mathrm{Kn} = 1$. As for the net tangential Knudsen force, which was obtained by integrating the tangential Knudsen stress over the bottom surface of the object, its value evaluated in the theoretical analysis shows a similar tendency to that obtained in DSMC in its dependency on the Knudsen number. Both show a peak in the transition flow regime, and vanishes in the continuum flow regime and in the free molecular flow regime. But, the values of both show a disparity. However, as what was done for $\mathrm{Kn} = 1$, by adding the contribution of flow to the tangential stress onto the theoretical results, the resulting net tangential Knudsen force show good agreement with that obtained in DSMC for $\mathrm{Kn} \leq 1$. This addition was not made for $\mathrm{Kn} > 1$ because the flow velocity at a region one mean free path below the upper surface, which is necessary to calculate the viscous effect, cannot be obtained since that region is occupied by the ratchet body. Furthermore, although by adding the contribution of flow onto the theoretical results, the resulting net tangential Knudsen force agrees with that obtained in DSMC for $\mathrm{Kn} \leq 1$, the resulting tangential Knudsen stress distribution still shows a quite different distribution from that of the DSMC simulation for low Knudsen numbers such as at $\mathrm{Kn} = 0.1$. As for this, by also adding the effect of thermal stress at $\mathrm{Kn} = 0.1$, the resulting distribution of the tangential Knudsen stress also shows good agreement with that in DSMC. From the agreement of the obtained tangential Knudsen forces between the theoretical analysis and the numerical experiment, it was found that the tangential Knudsen force is caused by three mechanisms. The first is the contribution of impinging molecules directly coming from the other surface with different

temperature without experiencing intermolecular collisions. The second is the contribution of viscous effect of thermally driven flows. The third is the contribution of thermal stress.

In chapter 4, an application of the phenomenon where thermally induced Knudsen forces can drive an object was proposed. Specifically, a concept of a tweezer-like mechanism which can be used to grasp and manipulate a micro-object without contact was presented. The DSMC simulations were performed to evaluate the Knudsen force exerted on a cold beam placed close to a heated thin plate mounted perpendicularly on a heated flat substrate. Here, the heated thin plate was considered as a tweezer and the cold beam was considered as the micro-object to be manipulated. The results showed that the net Knudsen forces on the beam are directed in the direction of the thin plate, and hence, the mechanism proposed above was achieved. The driving mechanism of this phenomenon is mainly due to the pressure differences induced by the thermal edge flows at the corners of the beam and the thermal edge flow at the tip of the thin plate. Due to the pressure differences between the top and bottom surfaces of the beam, and between the left and right sides of the beam, a force which attracts the beam to the plate horizontally and vertically was induced. Moreover, in the case when the height of the beam is shorter, this phenomenon is enhanced such that stronger net upward and rightward forces are induced. These thermally induced Knudsen forces are also found to be proportional to the temperature difference, and even at a low temperature difference of 25K, the mechanism proposed here can still be achieved. The results also showed that the thermally induced Knudsen forces are optimum when the distance between the beam and the thin plate is in the order of one mean free path.

To summarize, this thesis have provided answers to the following questions: what the effects of different parameters on the thermally induced tangential Knudsen force are, why the tangential Knudsen force can be generated, and how this Knudsen force can be used for certain applications.

List of Figures

List of Tables

Acknowledgement

This study would not be possible without the many people who encouraged and helped the author during the present work. Although only a few of them are mentioned here, the author extends his heartfelt gratitude to all of them.

Firstly, the author would like to express his profound respect and appreciation to his research supervisor, Professor Taku Ohara of the Institute of Fluid Science in Tohoku University for his kind consideration and unwavering support to help the author in completing this thesis. Also, the author would like to express his sincere gratitude to his former supervisor, Professor Shigeru Yonemura of the Department of Mechanical Engineering, College of Engineering, Chubu University, for his valuable insights on the present study.

Secondly, the author would like to convey his sincere thanks to the other members of his review committee, Professor Hiroki Nagai and Professor Naofumi Ohnishi of the Graduate School of Engineering in Tohoku University, for their expert assessment and constructive criticism.

Thirdly, the author would like to thank his previous colleagues in the Non-Equilibrium Molecular Gas Flow Laboratory, especially Dr. Yoshiaki Kawagoe, who helped the author hurdle many problems in the research, and the previous laboratory secretary, Ms. Megumi Akama for her untiring assistance to the author.

Fourthly, the author would like to recognize the financial support from the Japanese Government under Monbukagakusho (MEXT) Scholarship. The scholarship was a crucial aspect in inspiring and motivating the author in his studies in Japan.

Finally, the author would like to say thank you to his friends and families, both in the Philippines and in Japan, for always being there for him. But above all, the author gives his thanks to God Almighty, for the opportunities and the capabilities to proceed successfully.